UC Riverside

UC Riverside Electronic Theses and Dissertations

Title

Effect of Strut Design on Intra-Aneurysmal Hemodynamics: Implications for Flow Diversion

Permalink

https://escholarship.org/uc/item/0zg1m019

Author

Sommerkorn, Benjamin

Publication Date

2020

Peer reviewed|Thesis/dissertation

eScholarship.org Powered by the California Digital Library
University of California

UNIVERSITY OF CALIFORNIA
RIVERSIDE

Effect of Strut Design on Intra-Aneurysmal Hemodynamics: Implications for Flow Diversion

A Dissertation submitted in partial satisfaction
of the requirements for the degree of

Doctor of Philosophy

in

Mechanical Engineering

by

Benjamin S. Sommerkorn

September 2020

Dissertation Committee:
Dr. Masaru P. Rao, Chairperson
Dr. Marko Princevac
Dr. Victor Rodgers

Copyright by
Benjamin S. Sommerkorn
2020

The Dissertation of Benjamin S. Sommerkorn is approved:

_____

_____

_____

Committee Chairperson

University of California, Riverside

ACKNOWLEDGEMENTS

I'd like to thank first my chair and committee whose support both academically and otherwise have led me here. To Dr. Princevac who first took me into his laboratory and selflessly allowed me to leave in search of research that was a better fit while still giving me his time and expertise. He gave me my first teaching job and the financial help so desperately needed when I first arrived. I will miss talking about fluid mechanics and arguing about politics with you. To Dr. Rodgers whose scholarship is without equal and whose high standards and fierce rigor made me better even when it stung and whose incredibly kind words kept me going in equally dark times. You are the salt of the earth and I will miss getting advice from you and hogging your office hours. To Dr. Rao whose high hopes and spirits always kept me looking forward. Who believed in me and trusted me enough to not only pursue research outside his own wheelhouse but work in science communication and policy. My path is forever changed and pointed towards one that gives me much joy and I cannot thank you enough for giving me the freedom few other would have. You are a rare breed in the academy, and it is made better for having you there. I can't wait to see where we take this work next.

Secondly, I must thank all my friends and family. As many will tell you graduate school is a marathon not a sprint and there is no way I would have made it through without the endless love of so many. To my mother, Nanette, who instilled in me great pride and perseverance. Who taught me hard work and that giving up was never an option. To my big sisters Jennifer, Meagan, and Kelley who always had an ear for me when I needed it

and believe in me fiercely. You have all set an example for me as mentors, role models, friends, mothers, sisters and I am a better man for you all. To my twin Rachel, my other half who's always looked out for me and for who I fight for so dearly. You have one of the biggest hearts of anyone I know, and I am lucky to have you. To Drew and Holly, my science policy partners in crime who I owe the greatest debt of loyalty and love, you two saved my life. To Derek, John, Dustin, Root, Lynch, and Darren my brothers in spirit if not blood, I love you all and am lucky to be so rich. To Ryan, who without none of this research would be possible. You are my science muse, one of my best friends, and a great father and comrade, I cannot imagine crossing this finish line had we never met.

Lastly to my jaan Ryann and our fur children Rustin and Louise. The joy you bring to my life cannot be measured or written down. You are the light of my life, my stars, my moon, my partner and my rock though the final chapter of this crazy ride. The laughter of the last year alone is more than anyone could hope to have, and I can't wait to spend our lives together.

No one is an island, me least of all. Few who come from where I come from get this far and it is only because of countless acts of kindness, love, caring, mentorship, and time of which I can never pay back, or count, that I have. I am lucky beyond measure and so thankful.

DEDICATION

For Sadie, Savannah, Scarlet, Parker, Sabastian, Katie and Audrey

May you follow your dreams wherever they take you

There are no peaks out of reach

Even when they’re out of view

ABSTRACT OF THE DISSERTATION

Effect of Strut Design on Intra-Aneurysmal Hemodynamics:
Implications for Flow Diversion

by

Benjamin S. Sommerkorn

Doctor of Philosophy, Graduate Program in Mechanical Engineering
University of California, Riverside, September 2020
Dr. Masaru P. Rao, Chairperson

Flow diverting stents have transformed the treatment for intracranial aneurysms. These tightly braided metallic wire cylinders when deployed endovascularly at the neck of an aneurysm have been shown to drastically reduce intra-aneurysmal (IA) hemodynamic velocity and aneurysm lumen wall shear stress. These devices reduce the chance of rupture and thereby hemorrhagic stroke while simultaneously inducing thrombogenic cues for eventual aneurysm absorption. Current clinically available devices achieve this change in IA by manipulating device porosity and pore density to reduce shear into the aneurysm. Herein, it is demonstrated that device porosity, pore density and shear are not the only design parameters and physical mechanism to consider for flow diversion. 2D and 3D numerical simulations are compared to experimental devices deployed across the neurovasculature with varying diverter strut aspect ratios. Device designs whose struts

have an aspect ratio greater than one are shown to be effective at inducing hemodynamic transition into aneurysmal flow regimes associated with good clinical outcomes. High aspect ratio devices allow for higher porosities and reduce the IA hemodynamic response to potential changes in porosity. While addressing numerous clinical complications such as in-stent stenosis and edema this design simultaneously widens the range of devices indicated for use in high risk areas such as the posterior communicating artery and basilar trunk by altering the balance of energy transfer through the device from parent anatomy to aneurysm. These results show the potential of more robust devices of higher porosity and a reimagining of the physical forces being manipulated when flow diversion is considered in the clinic.

TABLE OF CONTENTS

TABLE OF FIGURES

1. INTRODUCTION

1.1. Stroke Pathology and Epidemiology

Stroke is a vascular disease that affects the brains ability to get oxygen from blood, impairing brain function and killing brain cells. In the United States alone, stroke is a leading cause of serious long-term disability, reducing mobility in more than half of stroke survivors age 65 and over, killed more than 140,000 people in 2016 and had a total expenditure of over 45 billion dollars from 2014 to 2015 (Benjamin et al., 2019). Predominantly separated into two types, stroke can be brought on by ischemia or hemorrhage. Ischemic strokes occur when the vasculature is obstructed, most commonly by fatty deposits on the lumen, preventing nutrients from reaching the brain, and account for 87% of all cases. Hemorrhagic stroke makes up the remaining 13% and is associated with intracranial (IC) bleeding caused by the rupture of some arterial segment, usually diseased dilated tissue called an aneurysm, denying the brain nutrients and bleeding into surrounding brain tissue. While ischemia makes up the majority of cases, hemorrhagic stroke is far deadlier, with over a third of cases associated with mortality and another third associated with significant morbidity. Treatments for ischemia have seen success with minimally targeted approaches such as tissue Plasminogen Activator (tPA) injections, by contrast hemorrhagic stroke requires highly targeted approaches at the site of hemorrhage, necessitating an extremely invasive craniotomy in a procedure known as surgical clipping.

Aneurysms are one of the primary causes for rupture and are common, with estimates of incidence ranging from 4% to 6 % of the population (Keedy, 2006). To prevent hemorrhage and eliminate the need for such invasive procedures much progress has been made with the use of new techniques for preventative treatment, focused primarily on IC aneurysms, using minimally invasive vascular catherization to address the lesion within

the anatomy. Treating the aneurysm endovascularly can be difficult given lesion morphology, anatomical location, health factors of patients and the myriad of biological and mechanical responses within the body (Pierot & Wakhloo, 2013). Current state of the art devices and techniques still lack the fidelity to be indicated for use in many parts of the vasculature were aneurysms occur, and current understanding of the mechanisms which drive some therapies remain unclear. The following work seeks to address these issues through a focus on the biomedical microdevices used for treatment, the introduction of new parameters for device design, and to further advance understanding of device effect on intra-aneurysmal (IA) hemodynamics.

1.2. Neurovascular Anatomy

1.2.1. Circle of Willis

The Circle of Willis refers to the vascular structure at the inferior side of the brain where the major blood supplying neuro-arteries meet and is responsible for supplying oxygenated blood to over 80% of the cerebrum. Eighty-five percent of saccular aneurysms will arise from the arteries of the Circle of Willis (Keedy, 2006). Exactly why aneurysms arise at all is still a question being asked by researchers, though a number of predictors and theories have arisen. The cellular structure of the cerebrum arterial lumen leave this anatomy particularly susceptible to aneurysm formation due to the absence of an external elastic lamina (Rowe et al., 2003). It has been theorized that due to the morphology of the structure such as vessel tortuosity, asymmetry, and arterial junctions that hemodynamic imbalances cause aneurysm formation (Kayembe et al., 1984). Still others use indicators such as high blood pressure, head trauma, smoking, gender, hypertension and genetics as predictors for aneurysms (Nahed et al., 2007; Ohkuma et al., 2002; Schievink, 1997; Seppo et al., 2005;

Weir et al., 2002). All these factors, along with where the lesion is in the anatomy, are included when deciding when to treat and the kinds of treatment options available to patients when a unruptured aneurysm is found.

The most frequent location for aneurysm growth is the anterior communicating artery (30%), followed by the posterior communicating (25%), middle cerebral (20%), internal carotid artery bifurcation (7.5%), basilar tip (7%), pericallosal artery (4%), and finally the posterior inferior cerebellar artery (3%) (Brisman JL, Song JK, Newell DW., 2006). The anterior circulation is composed of the anterior cerebral arteries, internal carotid arteries, and anterior communicating artery. They together make up the bulk of IC aneurysms, are where most research is conducted, and are where nearly all devices are currently indicated for use. The anterior circulation is generally characterized by larger vessel diameter and higher volumetric flow rates, leading credence to hemodynamical arguments for aneurysm growth. The posterior circulation though representing the minority of cases for aneurysms is associated with worse outcomes and smaller rates of treatment (Forget et al., 2001; Phillips et al., 2012; Pierot et al., 2008; Seibert et al., 2011).

1.2.2. Morphological Characteristics of Aneurysms

Aneurysms can be characterized in two broad categories: saccular and fusiform. Saccular are the most common, making up ninety percent of all diagnoses and get their name from the ballooning of a small segment of the vascular wall (Keedy, 2006). Fusiform represent a dilation encompassing the entire circumference of the vascular wall.

IC aneurysms are classified by geometry relative to clinical outcomes. Size, or maximum aneurysm diameter, is categorized as small (less than 6mm), medium (6 to 15 mm), large (16 to 25 mm) and giant (greater than 25 mm), in order of decreasing outcomes

(Orz et al., 1997). Secondly the aneurysm bleb itself is commonly categorized using neck size, dome height, and their ratio. Neck size, opening of aneurysm along vascular lumen, dome height, maximum distance from aneurysm lumen to vascular wall, and the ratio of these or the dome to neck ratio, are of particular importance in the use of endovascular techniques (Pierot et al., 2008). Some IA treatments such as coiling rely on large values of this ratio, requiring an aneurysm "shoulder" for the coils to rest upon. Ratio values less than 2 are deemed wide neck aneurysms, where stents were originally used to act as the shoulder, deemed stent-assisted coiling (Yi Sen Zhang et al., 2010). For aneurysms that fall outside of the shouldered large dome aneurysms (e.g. large and giant, fusiform, wide-neck, multiple aneurysms within a segmental diseased artery, and recurrent) newer flow diversion devices are now being used, which have shown significantly good clinical results (Pierot & Wakhloo, 2013). Even aneurysms which were previously untreatable such very small and blister-like aneurysms have been shown to benefit from this treatment (Kulcsár et al., 2010).

1.2.3. Biology of the Artery

Cerebral arteries are muscular arteries with a composite structure of smooth muscle cells and extracellular matrix fibers of collagen and elastin. The structure of the arterial wall consists of three layers, the outermost layer, the tunica adventia, a middle layer, the tunica media, and the innermost layer, the tunica intima. The adventia is connective tissue that attaches the artery to the surrounding tissue and is made up of bundles of wavy collagen fibers that provide the majority of longitudinal strength to the vessel (Rowe et al., 2003). Cerebral arteries are unique in that they do not have the elastic lamina found in systemic arteries that separate the adventia and media, with this boundary generally taken as the

edge of the smooth muscle layer that makes up the media (Ross & Pawlina, 2016). The tunica media is usually the thickest layer and is made up almost entirely of smooth muscle that not only provides strength to the vessel but controls vessel diameter to help regulate blood flow and pressure. The intima is a simple squamous epithelium cell subendothelium connected to the media by an internal elastic lamina and surrounded by a connective tissue basement membrane comprised of endothelial cells (ECs) in direct contact with blood, often called the lumen (Ross & Pawlina, 2016; Stehbens, 1990). ECs are in direct contact with blood flow and are heavily involved in signaling complexes and sensing of the various mechanical (e.g. fluid shear) and chemical (e.g. NO) cues present in the bloodstream.

1.2.4. Aneurysm Pathophysiology

The focus of the research herein is reducing the risk of aneurysm rupture and subsequent morbidity, but these are not the only pathophysiology of IC aneurysms. The presence of an aneurysm within the neurovasculature has long been known to cause minor to severe headaches and the pitching of nerves, specifically those involved in oculomotion or movement of the eye, both responses to aneurysm growth and pressure on nerves, brain tissue etc. within the anatomy (Bartleson et al., 1986; Dandy, 1938; Soni, 1974; Trobe et al., 1978). Exactly why/how aneurysms arise, and grow is still not known. Growth rates depend on physiological and hydrodynamical factors such as parent vessel diameter, aneurysm entrance size, entrance blood pressure, as well vasculature health and integrity factors such as vasomotor reactivity and connective tissue metabolism (Portegies et al., 2014; Stehbens, 1990; Voldby et al., 1985). Though growth and rupture are certainly connected, both representing structural failures of the vasculature wall, their pathologies are not identical as not all aneurysms grow to eventually rupture. As mentioned above

many factors are used to test for rupture risk, though these are statistical in nature, providing insight not definitive answers. So too can it be said about the hemodynamic, structural, and mechanical arguments which involve factors too complex in geometries too myriad to have yet deduced any definitive measures or parameter thresholds for rupture. Though a threshold has not yet been found, much work has gone into understanding this interplay between the hemodynamic and wall integrity that affect an aneurysm propensity to rupture.

1.2.4.1. Factors Impacting Vessel Wall Integrity

Aneurysm lumen structure is a function of remodeling that takes place over the course of the tissue's disease state and several studies of aneurysms at varying stages of development have begun to shed light on this pathology. Post-mortem histological comparisons of ruptured and unruptured aneurysms found the ruptured aneurysms were characterized by smooth continuous endothelium while unruptured aneurysms displayed few ECs, luminal thrombus and disorganized mural cells nessicary for structural integrity. Other studies found an overexpression of collagenases such as matrix metallinoproteinase-9 which is involved in the dissolution of the basement membrane. Immunostaining of these tissues has revealed high levels of inflammation though it is generally considered to be effect of rupture rather than the cause (Frosen et al., 2012). When taken together this indicates a weakened lumen structure as a result of adverse cellular response.

1.2.4.2. Factors Influencing Physiological and Hemodynamic Forces

Many studies have examined the relationship between arterial and aneurysmal geometries, anatomically driven flow parameters, and outcomes. Many of these studies have the aim of advancing toward a threshold value of conditions under which rupture can be predicted.

While several of these factors such as dome-to-neck ratio and various abnormalities are discussed elsewhere in this text in terms of their applicability to clinical practice and device selection, no single geometry-based metric has been able to predict rupture with enough sensitivity and specificity to merit clinical use on a diagnostic basis. Although no geometric parameter has emerged given the range of anatomic variation, a host of individual studies have confirmed that bifurcation angles, tortuosity and aneurysm morphology significantly impact the intra-aneurysmal velocity and distribution of stresses across the aneurysm tissue.

One commonality to both physiological force (e.g. pressure, velocity) and vessel wall integrity (via EC phenotype) is that both are affected by the magnitude and qualitative characteristics of blood flow. This coupling in applied force and reaction force arises due to the contact between circulating blood and the endothelium, which is responsible for translating sensed shear into biochemical signals as a means to reorder the vasculature and minimize strain on the cell's cytoskeleton (Galbraith et al., 1998). Therefore, whether the primary mechanisms of rupture risk are via transport of biochemical factors, a result of EC mechanotransduction, or simply an increase in applied mechanical stress, modification of flow characteristics is central to restoring homeostasis. As a first-order approximation of this behavior, the work described in this text presumes minimization of intra-aneurysmal flow and shear stress to be a predictor of successful occlusion and resorption. However, it should be noted that the role of shear-stress in EC biology as it pertains to hemorrhagic stroke is not entirely understood and is somewhat context-dependent. As the present study is focused on the development of a flow diversion device that can affect changes equivalent

to those of a conventional flow diverter at increased porosities, minimization of intra-aneurysmal wall shear stress is a natural goal. If future studies in different contexts were to determine a required minimum wall shear stress, it follows that the present design could easily be modified via the design parameters explored herein (e.g. porosity, strut aspect-ratio) to modulate wall shear stress to a desired level.

1.3. Current State of the Art in Hemorrhagic Stroke Prevention

1.3.1. History of Treatment Options

Treatment of aneurysms began in the late 1930's when an aneurysm at the junction of the carotid artery and posterior communicating artery was "clipped" shut by Dr. Walter Dandy (Dandy, 1938). This treatment, deemed surgical clipping, aims to isolate an aneurysm from the normal circulation without blocking off any small perforating arteries nearby. Under general anesthesia, an opening is made in the skull, called a craniotomy. The brain is then gently retracted to locate the aneurysm. A small clip is placed across the neck of the aneurysm to block the normal blood flow from entering. Since its inception in 1936 techniques have improved drastically with the introduction of microsurgical techniques, the operating microscope, and a variety of self-closing aneurysm clips (Schievink, 1997). For much of the time since, this method has been considered the gold standard of treatment for IC aneurysms. With the relatively recent introduction of endovascular non-invasive treatment options this has been called into question. For treatment of ruptured aneurysms surgery still provides good outcomes, with its challenger, endovascular coiling, being associated with better outcomes but with greater risks of rebleeding (Li et al., 2013). In the treatment of unruptured aneurysms, data has remained inconclusive as to best practice, leaving the decision up to clinicians (Kotowski et al., 2013).

1.3.2. Current State of the Art in Minimally Invasive Devices

The first endovascular treatment for IC aneurysms was performed in 1939, where silver wire was placed into a giant carotid aneurysm (Werner et al., 1941). In 1964 catheterization of IC arteries was introduced followed by the development of balloon mounted flow guided catheters and detachable balloons designed to occlude IC aneurysms (Luessenhop & Velasquez, 1964; Serbinenko, 1974). Nearly twenty years after the inception of these treatments and technologies the first detachable coiling system was developed, becoming the basis of modern endovascular therapies (Guglielmi, Vinuela, Dion, et al., 1991; Guglielmi, Vinuela, Sepetka, et al., 1991). Coiling comes in a variety of treatments. Coiling can be effective by itself if the geometric conditions are met by the aneurysm or as an adjunct therapy with balloon and stent-assisted coiling. These techniques seek to broaden the range of geometries where this treatment can be effective by artificially creating the "neck" of an aneurysm to keep the coils from entering the parent artery (Pierot & Wakhloo, 2013). The two most frequent complications of aneurysm coiling are thromboembolic complications and intraoperative rupture (Luessenhop & Velasquez, 1964; Serbinenko, 1974).

1.3.3. Current State of the Art in Flow Diversion Stents

Flow diversion (FD) as a treatment for IC aneurysms has only been available to clinicians for the last ten to fifteen years. A Flow Diverting Stent (FDS) is a cylindrical metal mesh placed at the opening of an aneurysm intravascularly and has two main functions in treatment of IC aneurysms. Redirection of fluid and energy, and occlusion of the lesion at the neck.

By bridging the aneurysm neck high energy flow no longer impinges on the distal necks sensitive weakened tissue, reducing the risk of rupture. The porous nature of the device limits the shear rate into the aneurysm, slowing the flow inside and thereby reduces velocity and wall shear stress (WSS). This reduction of blood circulation within the aneurysm leads to flow stasis and promotes formation of a stable aneurysmal thrombus. The FDS provides a scaffold for neo-endothelialization tissue growth across the aneurysm neck, recreating the artery occluding the lesion, and allowing the thrombosed occluded aneurysm to be absorbed into the body.

These devices are usually defined by porosity and pore density, largely due to limitations in manufacturing and for its well-researched effects into IA properties, reducing velocity and WSS by as much as 90% (Durso et al., 2011). Clinical trials have shown high rates of aneurysm occlusion, with reasonable rates of procedure related morbidity and mortality (Brinjikji et al., 2013). Issues associated with this therapy include: side branch and perforator occlusion, in-device/ in-stent thrombosis, perianeurysmal edema, delayed hemorrhage and mandatory anti-platelet therapy for a period that can potentially last the lifetime of the patient (Pierot et al., 2008; Pierot & Wakhloo, 2013).

1.4. Scope of this Work

The work exhibited herein represents the first fluidic characterizations of real-world devices using an anisotropic strut design, establishing the groundwork for understanding the IA hemodynamic effect this radial anisotropy has when deployed endovascularly. These results exhibit the potential for inducing intra-aneurysmal flow reduction on a scale comparable to that of commercial devices at higher porosities and reducing uncertainty in IA hemodynamic response.

The effect of strut height on IA hemodynamics and the implications for FD were determined using computational and experimental methods, namely: A 2D study on IA response to strut size , shape and porosity in a posterior circulation model; 2D study on IA response to curvature, strut size, and porosity in the anterior circulation; and 3D computational hemodynamic characterization and benchmarking of a novel high strut height design against a representative current-generation flow diverter in an anatomical model for which current flow diverters are not indicated. Collectively these results indicate the potential benefit of this new design concept and provide a platform for future optimization efforts.

This work demonstrates a break from the traditional way of viewing the mechanics behind FD and the potential for a future generation of devices. Aneurysmal hemodynamics are not solely dominated by the reduction of shear rate due to device porosity. We show that the small pressure gradients induced radially across a device when implanted play an important role in determine IA flow regime and velocities. We show that the velocity reduction observed under treatment can be measurably and predictably manipulated using high aspect ratio stent struts that allow for devices of larger porosity and less uncertainly in reduction observed in vitro. This work helped formulate the hemodynamic characterization and theoretical framework behind a first-generation novel device developed in tandem using these parameters to achieve the first high porosity, high aspect ratio fluid diverting device.

2. METHODS

2.1. Introduction

All nessicary materials and characterization tools are outlined within this section with an introduction outlining their importance to this work. More information relating to the specific implementation of these tools/materials within this work can be found in the respective sections.

2.2. Device Characterization

Flow diverters are different from conventional stents used in the context of cardiovascular disease in that successful treatment is indicated primarily by reduction of high velocity impingement of blood onto aneurysmal lumen and significant alteration to IA hemodynamics in addition to arterial lumen patency. Changes to IA hemodynamics are characterized both by their magnitude and flow field as these are associated with not only reduction of rupture risk but aneurysm absorption and restructuring of the arterial lumen to that of a new non-diseased state. These flows are complex and dynamic, involving both chemical and mechanical stimuli to create the total desired therapy. As this work deals with the development of a first-generation device with novel design parameters, characterization has centered on the large-scale fluid mechanical alterations induced by device implantation.

2.3. Computational Fluid Dynamics

Due to the limited ability of experimental models to fully realize and easily test large scale IA hemodynamic changes Computational Fluid Dynamics (CFD) models were developed and experimentally validated to elucidate the effect of various device parameters on IA properties. CFD models utilize discretized geometry called a mesh and solve conservation

equation of interest and need across each discretized element iteratively until a user defined level of precision is reached across the entire geometry being considered.

ANSYS FLUENT (Canonsburg, PA) was used to generate all CFD data presented herein, while the mesh was constructed using ANSYS Meshing 17.1 (Ansys, Canonsburg, PA, USA). Meshing 17.1 cuts the geometry into a finite amount of control volumes which are utilized by Fluent to solve the conservation equations of mass, energy and momentum. The equations solved in ANSYS for the following models respectively are:

$$\frac{\partial \rho}{\partial t} + \nabla \cdot (\rho \vec{v}) = 0 \qquad \text{Eq. 2-1}$$

$$\frac{\partial}{\partial t}(\rho \vec{v}) + \nabla \cdot (\rho \vec{v} \vec{v}) = -\nabla p + \rho \vec{g} + \vec{F} \qquad \text{Eq. 2-2}$$

$$\frac{\partial}{\partial t}(\rho E) + \nabla \cdot \left(\vec{v}(\rho E + p)\right) = -\nabla \cdot \left(\sum_j h_j J_j\right) + S_h \qquad \text{Eq. 2-3}$$

where ρ is density, t is time, $\vec{v}$ is the velocity vector, p is pressure, $\vec{g}$ is gravitational vector, $\vec{F}$ are forces vectors from body and external forces, E is internal energy, h is enthalpy, J is mass flux, and S is generation.

A finite volume refers to the small volume surrounding each node point on a mesh. The finite volume method is a method for representing and evaluating partial differential equations in the form of algebraic equations by converting volume integrals in a partial differential equation that contain a divergence term to surface integrals, using the divergence theorem. These terms are then evaluated as fluxes at the surfaces of each finite

volume. Finite volume methods can be compared and contrasted with the finite difference methods, which approximate derivatives using nodal values, or finite element methods, which create local approximations of a solution using local data and construct a global approximation by stitching them together. In contrast a finite volume method evaluates exact expressions for the average value of the solution over some volume and uses this data to construct approximations of the solution within cells (Eymard et al., 2019).

Once our equations have been converted to a state which we can solve iteratively a method of solving them must be chosen. Solvers chosen inside of Fluent are determined by the user as many different methods are available to best converge given various assumptions for simplicity and nature of the problem to be solved. The steady-state Navier-Stokes equations were solved using the SIMPLE algorithm (Semi-Implicit Method for Pressure-Linked Equations). The SIMPLE algorithm uses a relationship between velocity and pressure corrections to enforce mass conservation and to obtain the pressure field. This iterative algorithm follows the following steps.

1. Set the boundary conditions.
2. Compute the gradients of velocity and pressure.
3. Solve the discretized momentum equation to compute the intermediate velocity field.
4. Compute the uncorrected mass fluxes at faces.
5. Solve the pressure correction equation to produce cell values of the pressure correction.

6. Update the pressure field $p = p^* + \alpha_p \cdot p'$: where α is the under-relaxation factor for pressure.
7. Update the boundary pressure corrections p'_b
8. Correct the face mass fluxes: $J_f = J_f^* + d_f(p'_{c0} - p'_{c1})$: where d_f is a function of the average of the momentum equation coefficients for the cells on either side of face
9. Correct the cell velocities: where is the gradient of the pressure corrections, is the vector of central coefficients for the discretized linear system representing the velocity equation and Vol is the cell volume.
10. Update density due to pressure changes.
11. Repeat until convergence

Where $*$ indicates a guessed value, $'$ represents a corrected value, f represents a value calculated on a face of a cell, and $c0, c1$ represent the values within the two cells on either side of the face.

Convergence for experiments detailed here were based on the continuity residuals. The scaled continuity residual equation used is $\bar{R} = (R^c_{iteration\ N}/R^c_{iteration\ 5})$ where $R^c_{iteration\ N}$ is the uncalled residual and $R^c_{iteration\ 5}$ is the largest absolute value of the continuity residual in the first five iterations. R^c is the sum across the cells of the mass creation for each cell.

For a general variable Φ at a cell P this can be generalized as follows.

$$\bar{R}^{\phi} = \frac{\sum_{cells\ P} |\sum_{nb} a_{nb}\Phi_{bn} + b - a_P\Phi_p|}{\sum_{cells\ P} |a_P\Phi_P|} \quad \text{Eq. 2-4}$$

$$a_P\phi_P = \sum_{nb} a_{nb}\,\Phi_{nb} + b \quad \text{Eq. 2-5}$$

$$a_P = \sum_{nb} a_{nb} - S_P \quad \text{Eq. 2-6}$$

Where a_P is the center coefficient, a_{nb} are the influence coefficients for the neighboring cells and b is the contribution of the constant part of the source term S_c in $S = S_c + S_{P\phi}$ and of the boundary conditions. Residuals are set by default to a value of 10^{-3}. Due to the very small nature of IA velocities when stented a value of 10^{-5} was chosen to insure accurate IA fluidic characterization (ANSYS® Academic Research Mechanical, Canonsburg, PA, 2013).

2.4. Particle Image Velocimetry

Particle Image Velocimetry can be considered the experimental analog to CFD in that it is also utilized to generate velocity vector fields with high spatial resolution. In this technique a fluid is seeded with neutrally-buoyant microparticles which either emit or scatter light from an applied light source. A flow is applied, and the trajectories of particles are captured using a high-speed camera. Since the frame rate is known, the trajectories of these particles can be used to determine local velocities using a technique borrowed from signal processing. Each frame of this video can be thought of a two-dimensional matrix of light intensities with peaks at particle locations. For analysis, this frame is subdivided into regions termed “interrogation windows”. Each of these windows contains a distinct light intensity signature which, in the presence of flow, ideally is not altered in scale or shape,

but instead is translated some distance within the interrogation window. In order to determine the displacement for each interrogation frame, the cross-correlation of two subsequent frames at the same location is calculated. This value is computed as the integral of the dot product of both the original and time-lagged signal across all possible displacements within the interrogation window. At the true displacement of the particles, the signals are most closely in-phase and their summation is therefore most additive. For this reason, the resultant cross-correlation signal has a maximum peak whose distance from (0,0) represents the displacement of the interrogation window (M. Raffel, C. Willert, S. Werely, 2007). In order for this cross-correlation technique to work, the original signal peaks should be well-defined, easily distinguished from background noise, and undergo a sufficient but not excessive displacement between subsequent frames. For this this reason, particle seeding concentration, frame rate, flow regime, light intensity, and magnification factor are all important parameters to consider when developing an experiment.

3. 2D STRUT MODULATION AND HEMODYNAMIC CHARACTERIZATION

3.1. Introduction

Flow diversion (FD) has recently emerged as an effective treatment in preventing the rupture of IC aneurysms in a minimally invasive manner. Using this technique, a densely braided mesh cylinder is endovascularly introduced, navigated, and deployed into the arterial segment from which an aneurysm arises (Brisman JL, Song JK, Newell DW., 2006; Byrne et al., 2010). This braid is typically porous enough to facilitate nutrient transfer in surrounding healthy tissue but also dense enough to divert high energy fluid flow from impinging on the already weakened tissue of the aneurysm sac, and significantly reduce shear transmission into the aneurysm from the parent vessel. The resulting stagnation of flow eventually causes the blood within the aneurysm to thrombose; completing the process of occluding the aneurysm from the parent artery altogether, and allowing for full reendothelialization of the vessel lumen and eventual resorption of the aneurysm (Kulcsár et al., 2012; Mut et al., 2015). It's understood that lower porosity is generally beneficial for FD but this effect comes at a cost to the surrounding healthy tissue and structures (e.g. parent artery ischemia/infarct, inflammation, in-stent stenosis, etc.) (Amir Paisal et al., 2017). From this principle, it follows that the ideal porosity is the maximum which would result in enough FD to lead to intra-saccular thrombosis while minimizing the vessel's exposure to the device and the risks associated therewith. Furthermore, porosity is not a fixed value in practice, but is highly dependent on deployment technique (i.e. axial compression) as well as anatomic features (e.g. tortuosity, proximal/distal arterial segment diameters). Several groups have commented on these effects and found that while most flow diverters exhibit this dependency, the relationship between anatomy and porosity can vary with device design (Shapiro et al., 2014). This motivates the investigation into

mechanisms by which the variability in the effect of porosity on flow diverter can be reduced in order to more reliably achieve a therapeutic amount of FD without sacrificing the health of the local vasculature. Herein, we aim to examine how the effect of porosity on the FD response can be modulated by strut shape and aspect ratio to elucidate the mechanisms that enable this therapy though the use of a 2D numerical analysis of a simple sidewall aneurysm.

3.2. Methods

3.2.1. Aneurysm and Vascular Model Morphology

Flow diverters differ from other endovascular treatment options (e.g. intra-saccular coils) in that device positioning (while heavily influenced by parent arterial geometry) is largely stable irrespective of aneurysm morphology (e.g. wide-necked or fusiform aneurysms). As such the geometry of the fluid domain was selected to mimic conditions in which flow diverters would be commonly used but may be contraindicated for other treatment options (e.g. intrasaccular devices). Fig 3-1 shows the idealized 2D sidewall IC aneurysm geometry considered in the Computational Fluid Dynamic (CFD) simulations, created using ANSYS Design Modeler. The aneurysm geometry is composed of a circular aneurysm sac of radius $r = 3.5mm$, aneurysm neck of width $w = 5mm$ and Height $h = 4mm$. The parent vessel has a diameter of $d = 3mm$ with upstream length of $45mm$ and a downstream length of $15mm$ from the aneurysm center. Parent arterial geometry was chosen to represent a diameter common to the neuroarteries with the highest prevalence of aneurysms (e.g. ACA, ICA) and within the range of basilar artery diameters (Schievink, 1997).

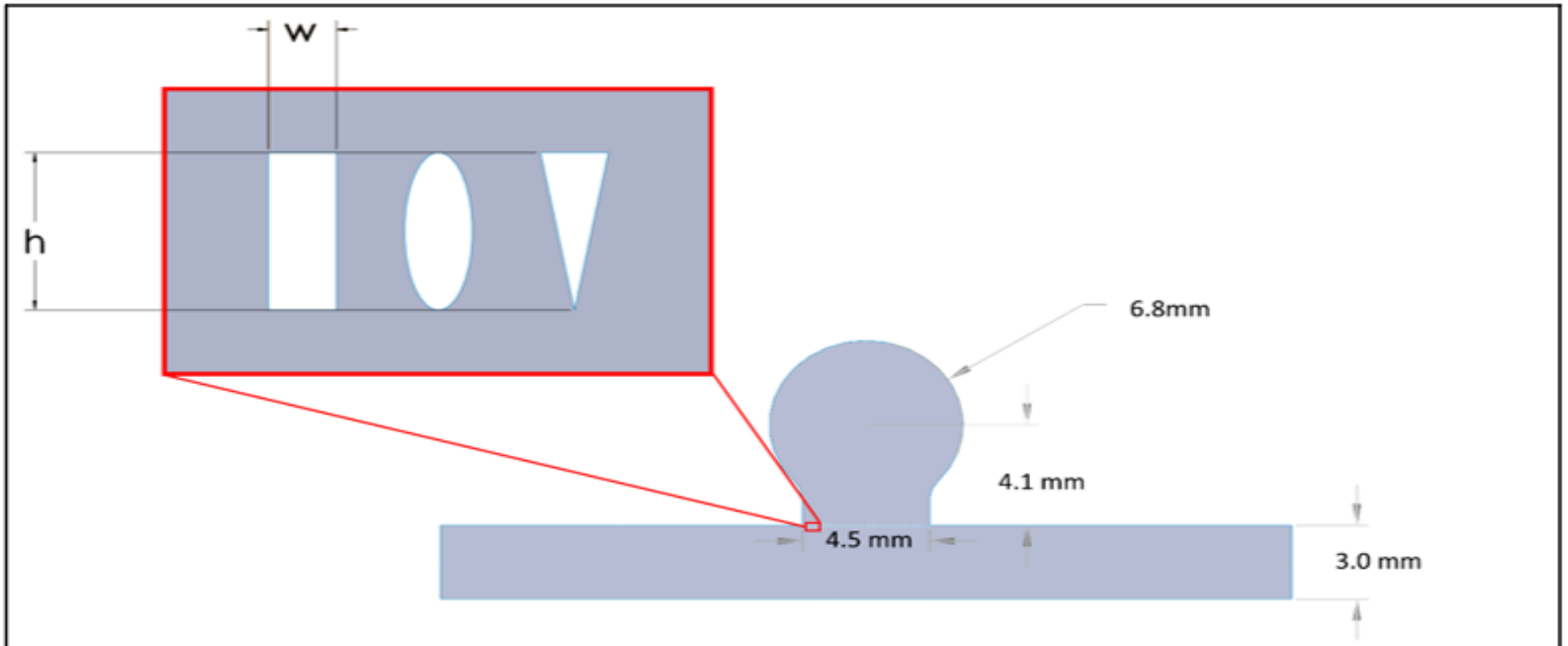

Dynamic Viscosity (μ)	Density (ρ)	Walls	Inlet Velocity	Outlet Pressure	Strut Width (w)	Strut Height (h)
$3.5 \times 10^{-3} Pa \cdot s$	$1064\ kg \cdot m^{-3}$	Rigid	$235\ mm \cdot s^{-1}$	$0\ psig$	$0.15\ mm$	$0.05\ mm$
						$0.075\ mm$
						$0.1\ mm$
						$0.15\ mm$
						$0.3\ mm$
						$0.45\ mm$

Figure 3-1: 2D Side Wall Wide Neck Aneurysm and relevant fluidic parameters used in computational fluid dynamic simulations. Radial strut size is varied by aspect ratio of strut width, kept constant at 0.15mm. Geometry and hemodynamic properties are modeled as the basilar artery.

Aneurysm geometry was chosen to represent a diameter which has previously been shown to be linked to an increased likelihood for rupture and neck width was chosen as to result in a dome-to-neck ratio for which flow diverters would commonly be indicated (Backes et al., 2014; Nelson et al., 2011).

Triangular, elliptical, and rectangular strut cross-sections are considered, though only Ellipse can be seen in Figure 1, as these shapes were tested using limited aspect ratios (ARs) by a number of other researchers (Bing et al., 2013). It has been shown that width has a near negligible effect on IA vorticity reduction (i.e. low impact on changing IA flow dynamics) therefore width was kept constant, SW, at $0.15mm$ while Strut Height, SH, was varied from $0.05mm$ to $0.45mm$ radially, spanning a range of ARs to capture its effects on IA properties (X. Xu & Lee, 2009). Strut characteristics are reported in nondimensional terms that are normalized by parent diameter. Porosity values range from 0.72 to 0.94, representing values that traditionally span the range of clinically relevant flow diverting stents (Lieber et al., 1997).

3.2.2. Discretization and Model Validity

CFD convergence criterium was a continuity residual of 1×10^{-5}. Mesh refinement was employed across geometrical parameters of interest (strut height, porosity, vessel curvature) to ensure mesh independence. The lowest porosity was considered during as it represents a change in the number of struts across the aneurysm neck (i.e. most complex geometry) and considered a reasonable approximation for the computational needs of all other porosity values. Mesh independence was calculated for average IA velocity across all strut heights and curvature values considered and are presented in Figure 3-2.

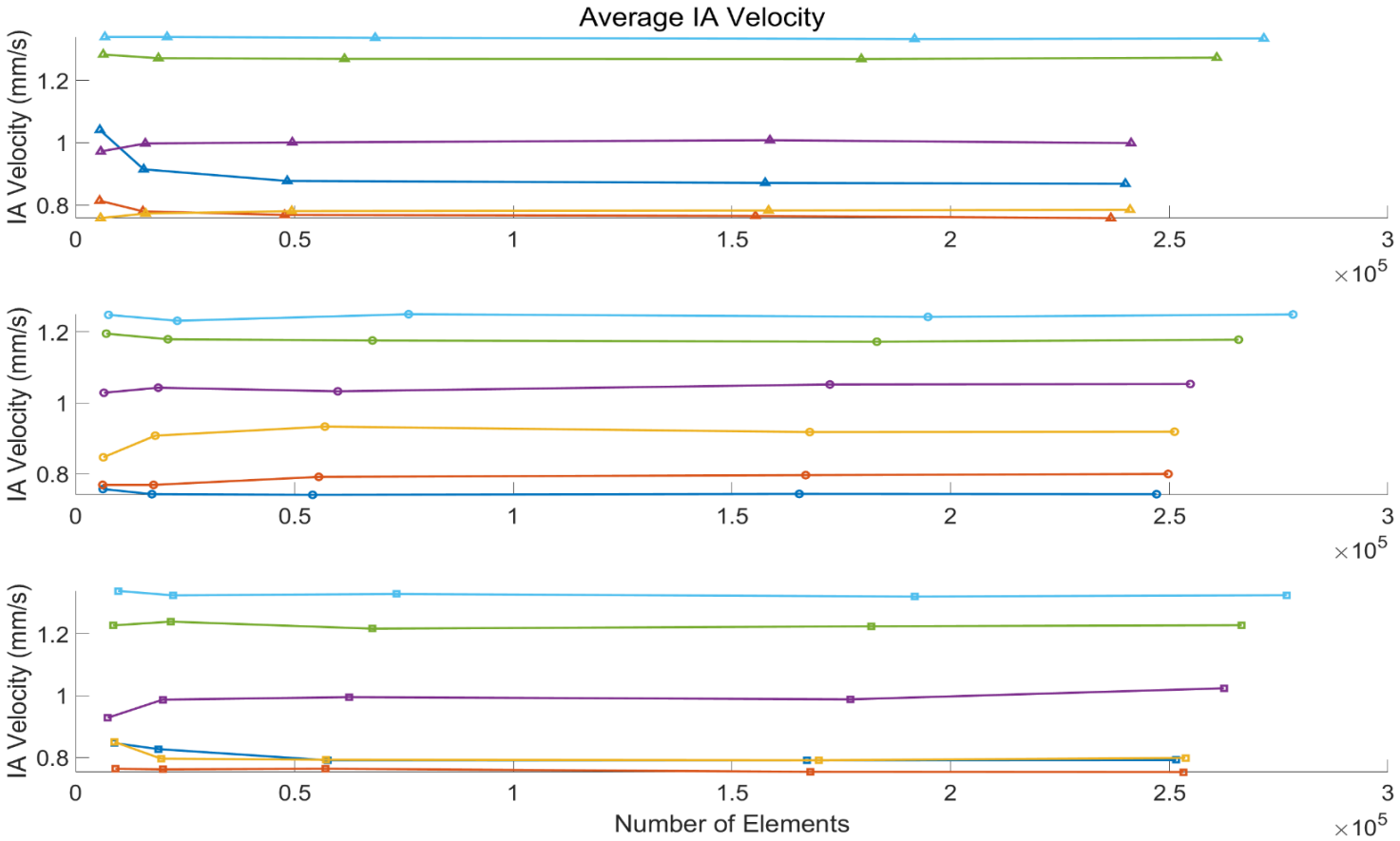

Figure 3-2: Aneurysmal XY midplane average velocity across mesh refinement of model geometry. Data is presented for porosity of 70 and all strut heights considered for triangle (top), ellipse (middle) and rectangle (bottom). Mesh independence is reached.

3.2.3. CFD and Computational Analysis

The vascular lumen was modeled as a ridged non-slip wall as is common within the literature, due to negligible distensibility of cerebral vasculature. Blood was modeled as a Newtonian fluid with density $\rho = 1060\ kg/m^3$ and viscosity $\mu = 3.5\ cP$ (Kenner et al., 1977; Peter W. et al., 1964). While blood is known to exhibit non-Newtonian properties, largely due to viscoelastic effects arising from the increased volume fraction of hematocrit in smaller vessels, these effects don't become significant at the diameter ranges considered within this study (Waite & Fine, 2007). Additionally, these parameters have been used widely in computational modeling of intravascular stenting in addition to having been validated experimentally (Aenis et al., 1997; Cho & Kensey, 1991; Y. H. Kim et al., 2010; LaBarabera, 1990; Ohta et al., 2005; Valencia & Solis, 2006). At the inlet an inviscid velocity boundary condition of $0.235\ m/s$ was chosen, corresponding to a volumetric flow rate of $1.6\ mL/s$; typical of the arterial segments being simulated (Lindegaard et al., 1987). The selection of an inviscid condition rather than a parabolic boundary condition was largely for simplicity as the boundary is sufficiently far from the hemodynamic region of interest such that any entrance effects are negligible. Upstream length L was chosen to remove entrance and boundary layer effects.

$$L = 0.05ReD \qquad \text{Eq. 3-1}$$

The Womersley number is a measure of dynamic similitude used commonly within the vascular system to describe the viscous damping behavior of blood relative to the time-

varying pressure gradient induced by the heart. This number is defined as $\alpha = d\sqrt{\frac{\omega\rho}{\mu}}$, where ω is the angular frequency of the heart rate, ρ is the blood's density and μ is its dynamic viscosity. For typical heart rates (between 60-100 bpm) this value is less than two in the neurovasculature; indicating that the flow is dominated by viscous forces rather than oscillating inertial forces (i.e. the flow is quasi-steady). Flows within this regime have a parabolic velocity profile at peak flow rate and a peak flow rate which is roughly 80% of the steady-state flow rate which would be observed for the same pressure gradient (J. Xu et al., 2015). In contrast, for $\alpha > 2$ the fluid core is dominated by inertial forces and toward the centerline has a much more uniform velocity distribution than near the walls; where these values rapidly approach the no-slip condition (u=0). Flows at high Womersley numbers also have peak flow rates that are significantly lower than steady-state flow rates under the peak pressure differentials. Since this study is largely concerned with the resulting changes to IA properties resulting from fluid shearing against stent struts near the vessel wall, a steady-state model using the volumetric flow rate near peak systole was considered a conservative but appropriate "snapshot" for comparing the effects of device geometry on the time-averaged magnitudes of fluid mechanic parameters relating to aneurysm rupture (Perktold et al., 1984; Walters, 1971). Additionally, Reynolds number values are small within the majority of the vascular system and in this instance is on the order of 200, which also indicates that a laminar flow model is suitable. Outlet boundary conditions were set to zero gage pressure as is common in the literature (Anzai et al., 2015; Moon et al., 2014; Vignon-Clementel et al., 2010; J. Xu et al., 2015).

The mesh was constructed using ANSYS Meshing 17.1 (Ansys, Canonsburg, PA, USA). Mesh independence was reached with saccular average velocity differences across mesh refinement of 2% or less. The number of elements across gaps was required to be 40, resulting in meshes of approximately 70 thousand elements and average orthogonal quality of .98. These parameters were chosen to capture flow regimes around struts and IA fluid properties.

Porosity, shape, and strut height were varied simultaneously to assess the impact of shape and strut size on spatially-averaged velocity and wall shear stress. The spatial average of the velocity is defined as follows:

$$\overline{v} = \frac{1}{A}\iint_{ROI}|v|dy\,dx = \sum_{i=0}^{N}\frac{1}{A_i}\sqrt{u_i^2 + v_i^2} \qquad \text{Eq. 3-2}$$

where u_i, v_i are the longitudinal and radial components of velocity respectively at the ith element, N is the number of elements and A_i is the area of the element at which the velocity magnitude is being calculated. Similarly, WSS is calculated as a weighted-average by element size, where the discretized differentials can also vary in size relative to the size of the elements near the wall:

$$\overline{WSS} = \frac{1}{s}\int_0^s \mu\left(\frac{du}{dy} + \frac{dv}{dx}\right)ds = \frac{1}{l_i}\sum_{i=0}^{N}\left(\frac{\Delta u_i}{\Delta y_i} + \frac{\Delta v_i}{\Delta x_i}\right) \qquad \text{Eq. 3-3}$$

As a control group, the average IA velocity and WSS were computed with no stent struts within the fluid domain in order to establish a baseline against which IA average velocity reduction (VR) and average WSS reduction (WSSR) are determined. Average reduction is defined as the percent difference of a stented aneurysm (S) from the non-stented (NS) case seen for a variable ϕ defined below.

$$\overline{Reduction_{\phi}} = \frac{NS_{\phi} - S_{\phi}}{NS_{\phi}} \times 100 \qquad \text{Eq. 3-4}$$

Bouillot et al. (year) have recently reported on the existence of a range of porosities which bridges the gap between traditional highly-porous stents and low-porosity flow diverters and within which there occurs a "hemodynamic transition" (Pierre Bouillot et al., 2014). This group has observed that when compared against an unstented control, flow diverter implantation not only reduces the magnitude of IA flow velocity but reduces IA vorticity and aligns the flow field such that it is in the same direction as parent artery flow. These studies, which evaluated commercially-available devices with AR of 1, suggested this transition in flow regime occurs as decreasing porosity reverses the dominant mechanism driving IA flow (i.e. shear vs. pressure). Similarly, in order to observe how these fields may be affected by the introduction of aspect ratio, streamlines and pressure contours are reported herein.

3.3. Results

Using ANSYS Fluent, IA average velocity and WSS were calculated for a range of shapes and porosities in a 2D idealized sidewall aneurysm model. IA velocity and WSS are

reported as reductions relative to a non-stented geometry, seen in equation 3-4. Figure 3-3 shows plots of VR and WSSR relative to porosity for the ellipse shape, where each line represents nondimensionalized strut height, $SH^* = \frac{SH}{D}$. Porosity values ranged from a low of 0.72 to a high of 0.94.

3.3.1. Strut Shape's Effect on IA Reductions

Shape was found to have little effect on IA properties. Rectangular struts induced larger reductions than that of other shapes in 70% of cases by an average of 3.8% VR and 2.2% WSSR. A table of shape comparisons and VR and WSSR for all three shapes can be seen in the appendix.

3.3.2. Strut Height's Effect on IA Reductions

Figure 3-3 shows VR and WSSR for the elliptical shape case. Given the limited effect of shape on IA properties, reductions for other shapes are presented in the appendix. Figure 3-3a demonstrates that VR is inversely proportional to porosity; a well-known result of FD stenting (Anzai et al., 2015). Additionally, the results show a sharper decline in VR after porosity 0.85, as the porosity regime transitions from that of FD to that of cardio of stent assisted stents. Perhaps most importantly, it can also be seen that the magnitude of this inverse relationship is reduced with increasing strut height (i.e. the curves flatten out at greater strut heights). This suggests that strut height may be a mechanism by which the effect of varying porosity can be reduced. The fanning in the data shows that the effect of SH on VR is correlated to porosity. At lower porosities it can be observed that all strut heights induce relatively similar amounts of VR. However, as porosity increases, the effect of SH on VR for a given porosity becomes more pronounced.

Figure 3-3b presents WSSR and has comparable results with VR; exhibiting an inverse relationship with respect to porosity as seen here and broadly within the literature (Seshadhri et al., 2011). Like VR, WSSR is negatively correlated with SH at the lowest porosity, and similarly reverses at higher porosities. Also similar to VR, the rate of WSSR changes relative to porosity decreases as SH increases. The range of WSSR values across SHs also increases with porosity, though more slowly and less dramatically than VR.

3.3.3. Strut Modulation's Effect IA Hemodynamics

The streamline plots in Figure 3-4 show velocity magnitude and streamlines for elliptical struts at high, medium, and low porosities and SHs. It can be seen that as porosity decreases, intra-aneurysmal flow regimes shift from those that are highly shear-driven; with strong rotational motion within the sac, to pressure driven; with fluid entering the aneurysm sac proximally and recombining with the flow in the parent artery distally. This motion causes the formation of small arterially aligned flow regimes in the aneurysm neck that extends into the saccular region. This alignment of IA flow in the direction of parent arterial flow has been remarked on by other groups as characteristic of the transition from "traditional" cardiac stents to flow diversion devices (Pierre Bouillot et al., 2014). This same transition can be observed even more markedly as SH increases; effectively eliminating the regions of shear-induced vortical motion seen at lower SHs and higher porosities. This suggests that increasing strut height may be a means of inducing behavior similar to flow diverting stents in a range of porosities that encompasses that of traditional stents. This transition between pressure and shear-driven flow can also be discerned by considering the effects of strut height on each fixed group of porosities.

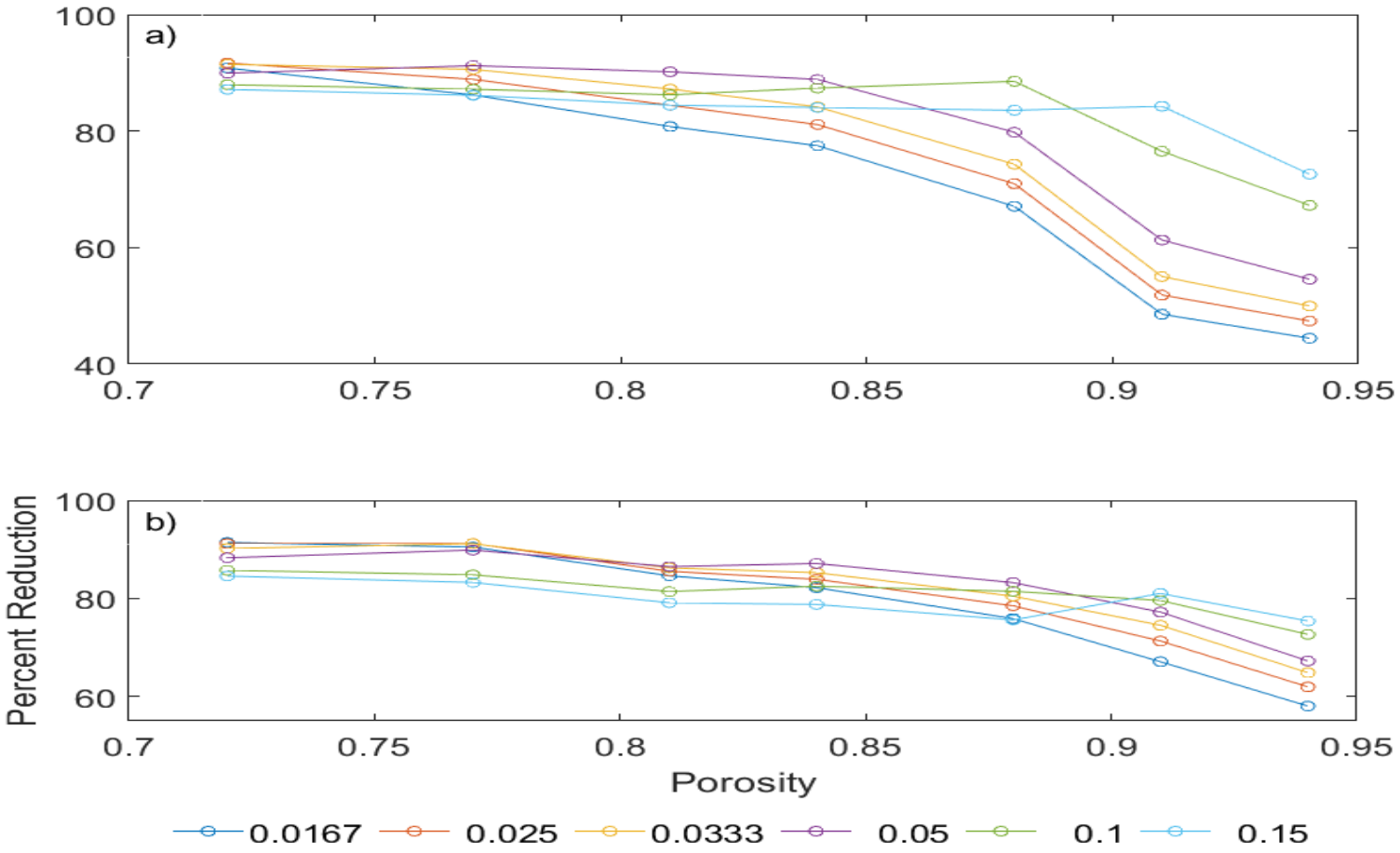

Figure 3-3: Velocity (a) and Wall Shear Stress (b) percent reductions relative to device porosity for the ellipse strut shape. Each line represents a different struts height which is nondimensionalized by the vasculature diameter. The general flattening of the curves as SH is increased indicate that increasing strut height reduces changes to aneurysmal reductions when porosity is increased.

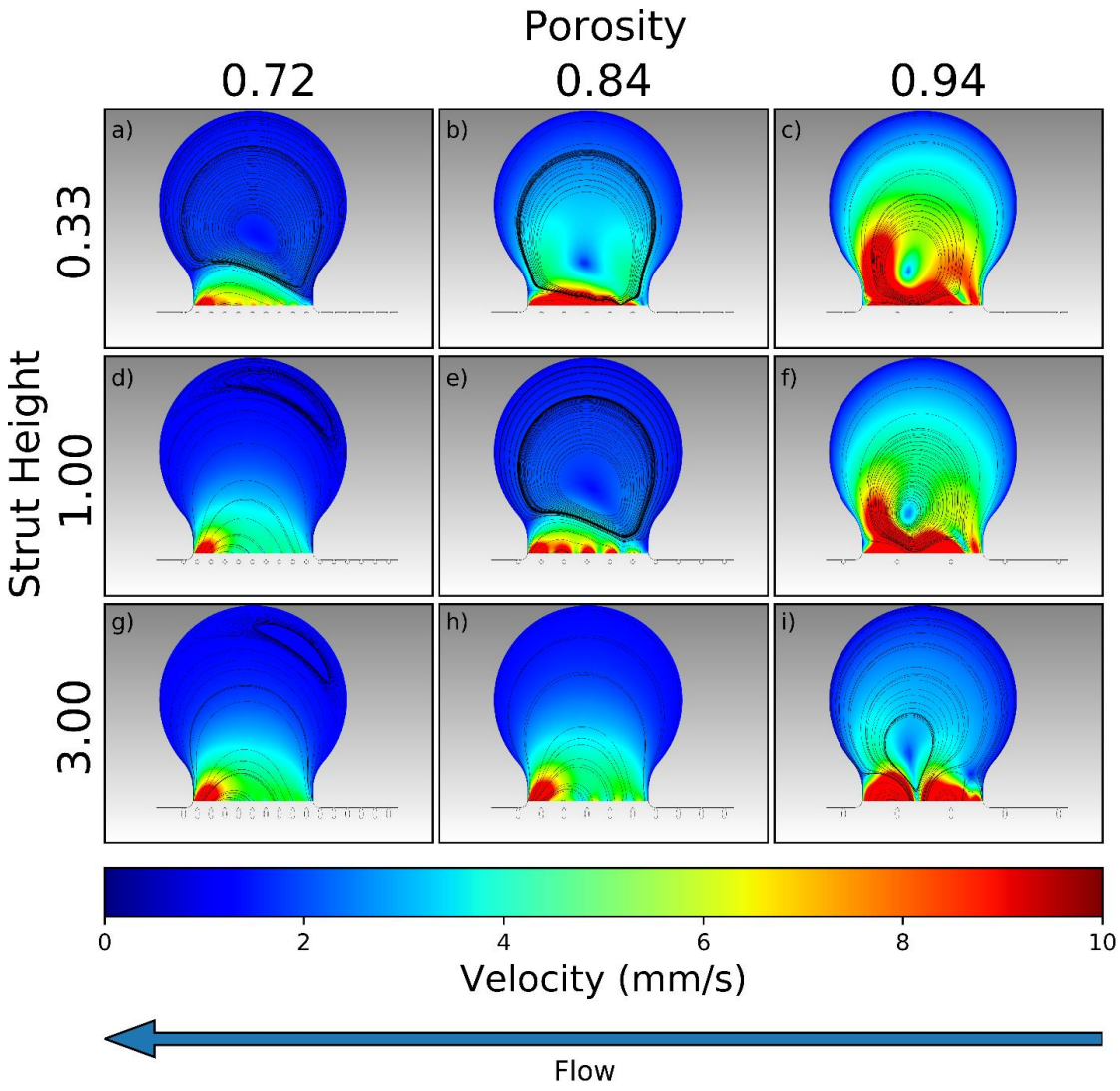

Figure 3-4: Aneurysmal streamlines and velocity magnitude at the aneurysm midplane. Porosity (horizontal) and Strut Height (vertical) represent the low medium and high values tested. SH increases flow into the aneurysm for any given porosity as SH increases. Shearing rotational motion gets stronger as porosity increases. Taken together, moving along the diagonal, shows the ability of SH to modulate aneurysmal reductions.

At the lowest porosity it can be seen from Figure 3-4 that increasing SH slightly increases IA flow and that this trend steadily reverses as porosity increases. This arises due to mass transfer from the parent and because max velocity values increase at the distal aneurysm neck/parent boundary where the pressure driven regimes exit the aneurysm and recombine with parent.

At the mid-range porosity of 0.84 this trend reverses significantly with higher strut heights clearly inducing this characteristic aligned flow. However, this change in flow regime does not necessarily coincide with a reduction in average IA velocity. This suggests a tradeoff between shear transmission reduction due to device porosity and mass flow induced by device driven arterial fluidic resistance, and potentially offers a new optimization parameter in device design.

At the highest porosity all regimes regardless of strut size are shear driven. Though interestingly the usual defining characteristics of a pressure driven regime, (i.e. an aligned IA flow with a proximal inlet and distal outlet), is represented in the last case. The strength of the shear driven motion dominates, but at high strut height two arterial alignments appear in the aneurysm neck at the proximal and distal sides. This regime has an outlet and inlet in the middle of the neck opening, creating two counter-rotating vortices which extend nearly into the aneurysm sac, significantly reducing IA properties. At this porosity increasing SH always improves reductions and can be seen in Figure 3-4 as the high-speed shear motion slowing down as SH increases.

Moving along the diagonal (i.e. increasing both porosity and SH), it can be seen that flow regimes are generally qualitatively similar. This suggests that increasing SH may

be a means of achieving comparable flow reductions (e.g. 2-5%) at significantly higher porosities (e.g. 17%).

Figure 3-5 shows velocity fields around the struts at the aneurysm neck for cases along the top-left-to-bottom-right diagonal of Figure 3-4 and show how SH induces transition to pressure driven regimes. These plots are especially illustrative of the hemodynamic transition as they exhibit traits of both shear and pressure-driven IA flow regimes.

It's known that the presence of a stent (regardless of porosity or AR) will reduce the amount of available area at the aneurysm neck for shear transmission and the consequent counter-rotational flow. Since increasing the strut area decreases the available fluidic area for shear-transmission, it follows that (similar to reducing porosity) increasing the area of each individual strut should also have the effect of reducing this vortical flow. This explains why although fig 3-5a and 3-5b show larger perturbations in the near-strut flow fields with increasing SH, the resulting IA flow regimes and VRs in 3a and 3b are strikingly similar. However, fig 3-5c demonstrates the limitation of modulating VR solely as a function of total strut area at the aneurysm neck. It can be seen that increasing SH results in impingement of higher velocity flows on the struts and effectively shrinks the arterial diameter. Together, these phenomena increase the angle of attack of local velocity vectors into the aneurysm sac and increase local pressure differentials at aneurysmal/arterial interface. Figure 3-6 shows pressure contours along the aneurysm neck of the ellipse shape for high, medium, and low porosity and SH.

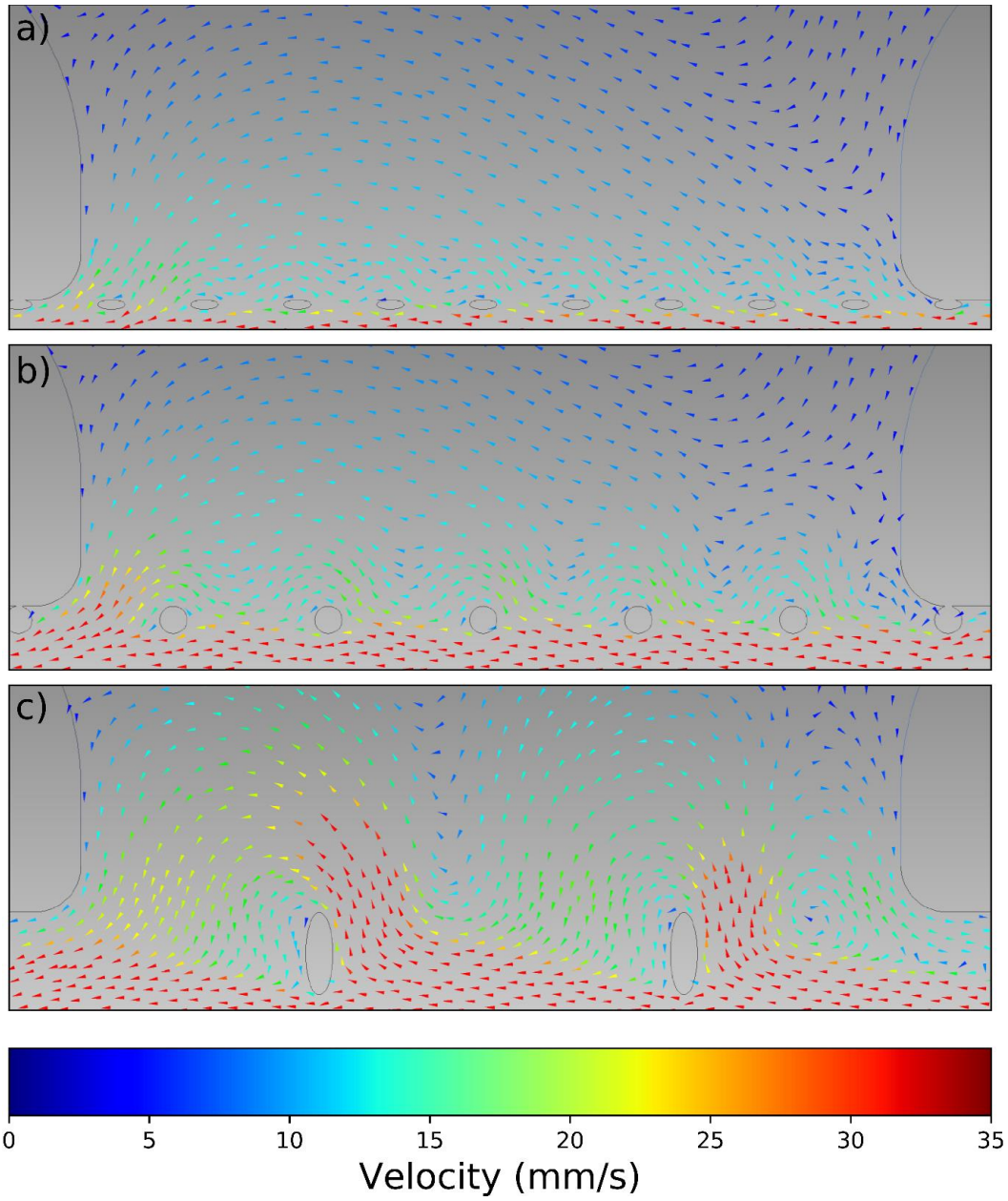

Figure 3-5: Near strut velocity field Porosity 0.72 SH 0.033 (a), Porosity 0.84 and SH 0.05 (b), Porosity 0.94 and SH 0.15 (c). Increased hemodynamic activity near struts due to increased inertial or pressure driven inflow as SH get larger and dampens the effect increased porosity has on IA properties from increased shear transfer.

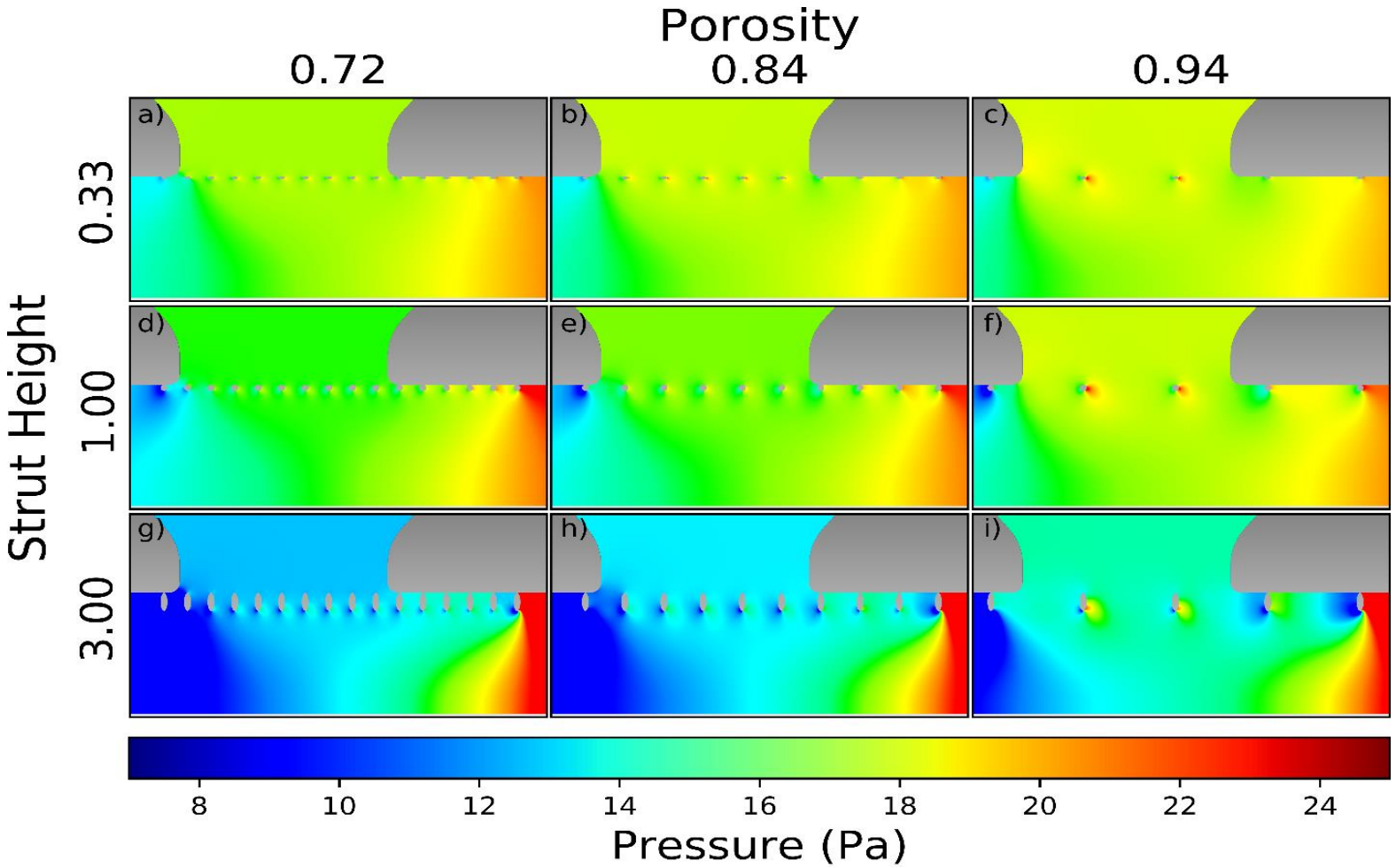

Figure 3-6: Pressure field across aneurysmal opening with varying porosity (horizontal) and varying strut height (vertical). Neck or near stent pressures do not significantly change as porosity changes but see significant changes as SH in increased. This change in pressure causes the increase hemodynamic activity near struts that modulates aneurysm response to porosity.

The results observed are consistent with those reported by other groups who have concluded that there exist two distinct flow regimes within the context of porosity-driven device design (i.e. pressure driven, arterially-aligned flows and shear-driven counter-rotational flows). Bouillot et al. 2015 describe the transition between these regimes as the result of reduced shear rate through the aneurysm neck and oppositely oriented pressure differentials at the arterial segments proximal and distal of the aneurysm. As seen in the figure this result is well represented for any given SH as porosity is varied.

Pressure gradients are spatially-compressed around the aneurysm neck causing inflow and outflow regions of the aneurysm sac and altering IA flow regime as porosity is decreased. However, when SH is introduced this effect becomes much more pronounced. Increases in SH augment the differentials at the aneurysm neck much more strongly. This induces pressure driven flow regimes at higher porosities than lower strut cases (as seen in the streamline plots of Figure 3-4). Figure 3-6 makes it clear that the hemodynamic transition observed by Bouillot and collaborators is not solely a function of reduced strain rate driven by reductions in device porosity. It is also a result of increases in fluidic resistance within the parent vessel, increased bluff body resistance as struts impede more flow, and increased flow disturbances. Reductions in porosity and increases in strut height therefore affect the same mechanism and induce the same behavior. From the fig. 3-6 it follows that changes in the stented arterial pressure field arise due to increased parent arterial friction induced by device struts, as well as changes in effective parent diameter within regions where the device is deployed. These changes in pressure combined with reduced strain rate transmission into the sac dominate hemodynamic transition.

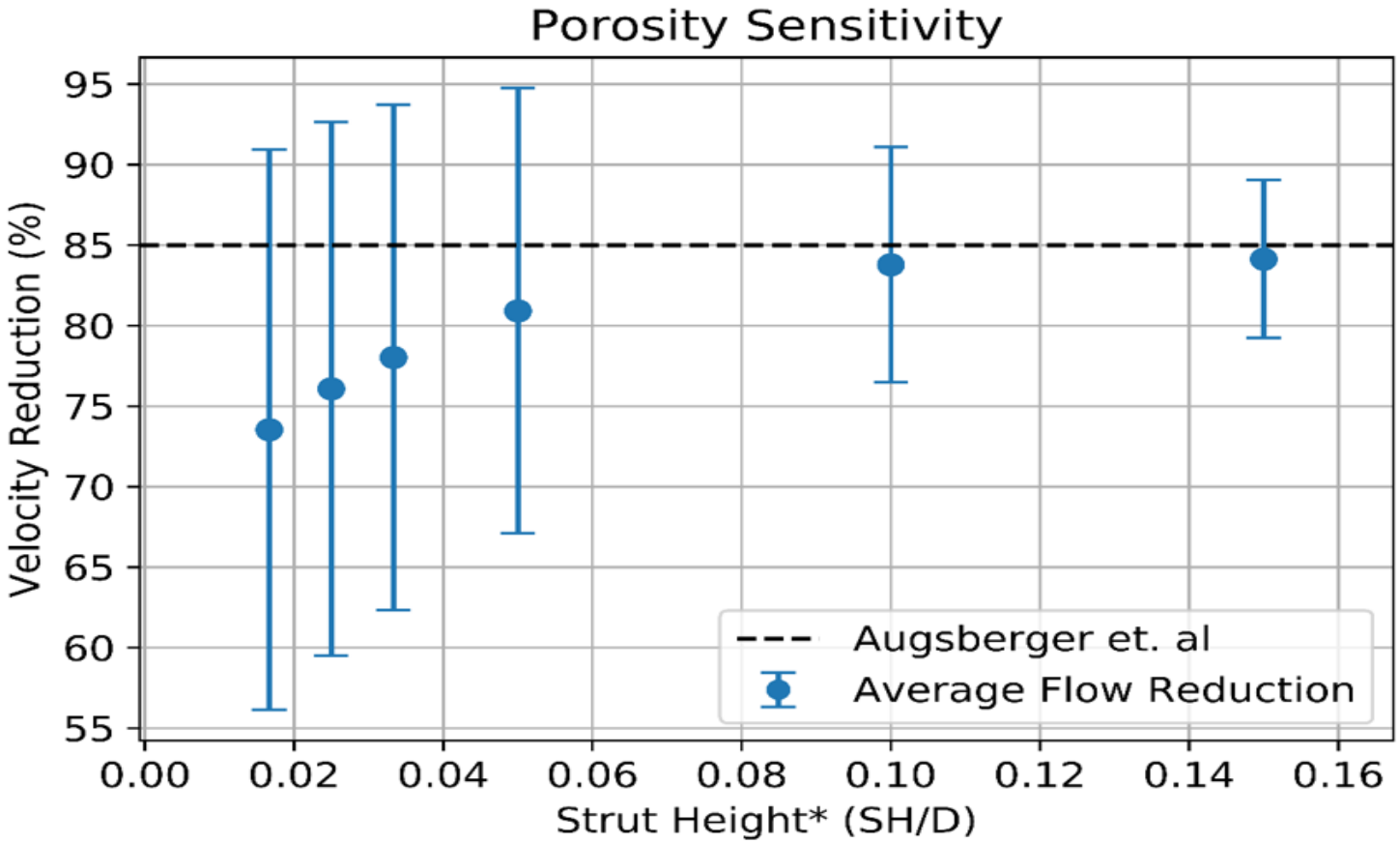

Figure 3-7: Device Sensitivity to Porosity. Bars are not error. The bars represent range of velocity reduction values observed across the range of porosity values tested for a given strut height. The range of reduction values observed decreases as SH increases as well as the average therein. This can be conceptualized as the aneurysmal response to changes in porosity or porosity sensitivity. Increasing SH reduces aneurysmal response to changes in porosity

At increased AR's, changes to fluidic resistance are enhanced, reducing the effect simple changes to porosity have on IC properties of interest. This ability to diminish the dependence of VR on porosity may prove clinically advantageous, as practically porosity isn't a fixed value but rather can vary widely due to the anatomy. It therefore may be more appropriate to consider a range of potential porosities when trying to predict patient outcomes.

To this end, Figure 3-7 shows the average and range of VR values across all porosities for any given strut height, benchmarked against the average VR values across devices of varying porosity observed by Augsberger et al. 2019under similar flow conditions. It can be seen in the figure that as SH increases, the range of VR across all porosities decreases (also seen in Figure 3-3 as the flattening of each curve for increasing SH). IA reductions dependence on porosity declines as a function of SH, or its sensitivity to changes in porosity is reduced.

3.3.4. Discussion

Results indicated that strut shape plays a small but observable role in VR. All three shapes showed nearly identical patterns of flow reduction for every SH and porosity considered, emphasizing shape's limited role in IA shear/pressure transition or changes in IA properties generally. However, greater VR reductions were observed for rectangular cross-sections; a result seen previously in the literature (Y. H. Kim et al., 2010).

Though shape plays a limited role in altering IA flow parameters, a strong dependence on SH was observed. While intra-aneurysmal velocity is inversely related to porosity in all cases, at increased strut heights (i.e. larger AR's) the effect of porosity on flow reduction is less pronounced than for smaller strut heights. From Fig 3-3 it can be

observed that although the largest VR's occur at low SH and low porosities, is also seen that low SH exhibits the greatest range of potential VR's when also considering the potential for variance in effective porosity of a device in-vivo. At low porosities, increasing SH marginally reduces VR. However, at higher SH's it is observed that VR variance is more robust to changes in porosities (i.e. the sensitivity is reduced). Many investigators have shown porosity to be highly dependent on geometry of the neurovasculature (Damiano et al., 2017). Because the anatomy can vary so widely, porosity can therefore also be thought of a random variable when trying to extend conclusions from computational results into large populations. When considered in this way, it can be shown that SH both increases the average VR and reduces its variance across a range of potential porosities, seen in Figure 3-7.

The transition in flow regimes remarked upon by other groups may be explained by an increase in fluidic resistance. Increasing strut height may be an alternate means of inducing equivalent resistances to commercially-available FD's at higher porosities and in a manner that is less dependent on anatomy than porosity. This framework of fluidic resistance across FDS offers an explanation as to how equivalent flow reductions may be achieved at increased porosities but it also suggests some negative consequences. For instance, a device which is more porous with increased strut AR may induce a therapeutic amount of flow reduction, but this behavior may show greater sensitivity to device placement as each individual strut induces a larger local resistance and larger wake formations distally, seen in Figure 3-5, at high SH and lower porosity. Additionally, the effect of the increased forces on these struts and total device should be considered and may

preclude the selection of certain materials or designs. While this study neglected fluid-structure interactions for the range of AR's considered, the increased friction between the device and arterial wall required to prevent device migration as drag force increases imposes a limitation on the degree to which aspect ratio can be used to increase flow diversion. Although these remain important considerations, the current results offer promise as a mechanism to achieve flow diversion while simultaneously reducing device exposure.

Optimizing the biological response against these tradeoffs requires a target value for VR, but in-vivo determination of a threshold value as a predictor of treatment efficacy has proven challenging. Patient-specific computational models paired with data on clinical outcomes have had moderate success at establishing thresholds in limited sample sizes, however the lack of statistical power has likely led to conservative estimates (Ouared et al., 2016). Nevertheless, these preliminary evaluations suggest the existence of such a threshold, motivating the investigation into design-based means of increasing flow reduction. In practice, FD's are designed to target a given percentage of metal coverage, but the resultant porosity post-deployment is highly-dependent on anatomy and technique. Therefore, it may be more appropriate to consider device effects on flow diversion across a range of porosities in order to characterize its robustness against commonly encountered variables which can affect resultant device geometry (e.g. tortuosity, varying arterial segment diameters, etc.). To this end, Fig. 3-7 demonstrates the potential to use strut height as a means of increasing the average flow diversion across a range of porosities while reducing the variability within group. Additionally, when compared against in-vitro

measurements of flow reduction using clinically-available, low porosity (63%) flow diverters under similar flow conditions and morphology, it can be seen the average performance approaches similar VR values.[3] These results demonstrate the potential to use aspect ratio to increase the robustness of flow diverters against clinical variables that may influence the porosity in-vivo.

Until very recently investigating IA changes with respect to stent strut shape was only a theoretical exercise but as fabrication techniques advance and FD stents see more wide-spread use, stents of asymmetric, non-circular cross sections will warrant further investigation. This is exemplified by the stent developed by Howe et al; a stretchable microfabricated thin-film flow diverter with rectangular cross-sectional elements (Howe et al., 2018). This group was able to demonstrate that precise definition and control of micro-scale design features (e.g. strut width, pore density) may be a more effective means of achieving flow diversion reliably rather than relying on a broader descriptor such as percent metal coverage. While this study is encouraging, it's limited in its ability to investigate the effects of AR as thin-film fabrication techniques are generally unsuitable for creating structures of the required depth relative to strut width. Nevertheless, this study is instructive as a potential means of realizing the potential of the results described herein.

Further studies using more complex geometry and boundary conditions are needed to fully realize the potential impacts on stent design optimization and hemodynamic changes associated with high AR struts. The study did not investigate the full range of porosities seen in clinically deployed devices and built upon the work of researchers which considered larger strut geometries than are commonly employed (i.e. strut widths of

150μm) (X. Xu & Lee, 2009). Additional studies more robustly investigating clinically relevant porosity ranges as well as more accurate pore density and strut length scales are needed to fully elucidate IA fluidic and property changes associated with large AR stents. However, this result indicates a potential path forward for manufacturing of higher porosity FD's to alleviate associated risks associated with device exposure (e.g. inflammation, nickel sensitivity, ischemia, infarct).

Lastly, the implications of this data present an interesting contrast to the conclusions drawn by many other investigators in the context of coronary stenting. A considerable amount of existing literature has suggested that stent struts should be as low-profile as possible to minimize small-scale, near-wall flow perturbations which have been shown to have adverse effects to endothelial cell function in addition to contributing to neointimal hyperplasia and in-stent stenosis (Duraiswamy et al., 2007). This is intuitive for stents which have the primary purpose of restoring lumen patency. However, it may be advantageous to maximize this effect for an application such as flow diversion; where a large portion of stent struts are not in contact with a vessel wall and flow perturbation is the design intent. What remains to be discovered is the effect strut height plays in this new hemodynamic niche where thrombosis and neointimal growth are intentionally induced as part of the therapy. Previous computational studies have shown that the number of struts (i.e. porosity) makes a larger contribution to large regions of low WSS (which has been correlated to neointimal hyperplasia) than strut height (LaDisa et al., 2004). Given this result, it may be a possibility that high-porosity, high-AR stent struts are an effective

strategy to maximize flow diversion immediately post-implantation while reducing the risk of in-stent stenosis later after neointimal remodeling has occurred.

4. 2D HIGH ASPECT RATIO STRUT AND NEUROVASCULAR CURVATURE IN THE ICA

4.1. Introduction

As shown in previous work by the author flow diverting stent performance can potentially be enhanced by modulating stent strut geometry in the radial direction (i.e. changing strut height). Previous work focused on elucidating the relationship between strut height (SH) and subsequently, SH values were exaggerated for effect. Herein modeled stent struts are defined on a scale comparable to that of currently clinically available devices to understand if these trends hold when SH size are an order of magnitude smaller. Porosity is again varied across a range of clinically relevant values and the resulting sensitivity of IA performance is reported. Previous work is further improved by changing anatomic and aneurysm anatomy to that where aneurysms are more commonly treated and where FDS are indicated for use and investigating the effect of SH on IA properties when curvature is varied.

The individual morphology of a brain aneurysm and the surrounding vasculature is of significant importance for determination of risk, endovascular therapy options and the hemodynamic variations observed (Skodvin et al., 2017). The specific influence on IA flow fields of aneurysm shape, size, and the angle of flow have all been robustly characterized. However, parent vessel morphology (specifically tortuosity as it interacts with varying device design parameters) has not been investigated due to the complexity of parameters involved though device performance can be heavily affected by parent vessel and aneurysm morphology. Increased curvature at the aneurysm site can result in malapposition of the flow diverter after deployment due to device migration, resulting in poor device performance at best and accelerating rupture at worst (Matsuda et al., 2018). Parent vessel geometry can also cause a devices porosity to change due to the nature of current generation

devices resulting in unpredictable behavior and performance (Damiano et al., 2017). In a computational study using varying radii of curvature, researchers observed that as the curvature of the parent vessel increases, the flow changes from a shear driven regime to a inertial regime with flows of higher velocity which are directed towards the aneurysmal cavity; reducing the probability of occlusion, thrombosis, reabsorption, and increasing potential for early rupture through impingement on weakened aneurysm lumen (Meng, Wang, Kim, Ecker, & Hopkins, 2006). In these inertial regimes the magnitude of velocity and vorticity were determined to be three to four times higher while also representing reduced performance and outcomes when treated with FDS (Augsburger et al., 2009; M. Kim et al., 2008).

To investigate curvature's effect on IA properties and stent performance the internal carotid artery (ICA) was chosen as the geometry to be modeled as it has been associated with increased development and rupture of IC aneurysms (Kliś et al., 2019; Lauric et al., 2014; Passerini et al., 2012). The ICA geometry consists of various segments as classified by Bouthillier, and the cavernous segment was chosen out of these seven segments as it is associated with the maximum number of bends (Bouthillier et al., 1996). The highly tortuous nature of ICA and the precedent of being susceptible to aneurysm formation make it an appropriate candidate for studying the effect of tortuosity.

4.2. Methods

4.2.1. Aneurysm and Vascular Model Morphology

A 2D parametric study with an idealized side wall aneurysm geometry was performed to elucidate the relationship between FD strut height, porosity, and curvature. Fig 4-1 shows an idealized 2D model of a sidewall aneurysm on an internal carotid artery that was used

in the CFD simulations. The model comprises of a circular aneurysmal sac of radius R = 3mm, neck width W = 4.5mm and neck height H = 1.5 mm. The diameter of the aneurysm used for the study was chosen based on literature that has shown an increased incidence for rupture (Jeong et al., 2009). The dome-to-neck ratio of DNR = 1.33 was considered as low diverters have been commonly recommended for DNR's less than 1.5 (Nelson et al., 2011). The diameter of the parent vessel D = 3 mm was chosen as this falls in the range of values for the ICA and allows for direct comparison against other work for SH. Additionally, the parent length is extended to 10 times the vessel diameter on both sides, to ensure developed flow before entering the aneurysm. Parent artery model is consistent with Internal Carotid Artery, which has been known to have a high prevalence of aneurysms and more arterial bends than other arteries in the cerebral vasculature (Lin et al., 2015). The cavernous segment of ICA extends from petrolingual ligament to the dural ring in a characteristic S shape defined by two distinct bends, anterior genu and posterior genu, connected by a horizontal segment. This S shape is commonly referred to as the carotid siphon and has angles ranging upwards of 90˚. Furthermore, the S shaped Carotid in itself is classified to have varied shapes such as the U shape, V shape, C shape, and arc shape (Lin et al., 2015; Pu et al., 2012). To model this behavior curvature is changed from 0 – 180 degrees in 45-degree steps (Figure 4-1) as this range takes into consideration the curvature of most of the arterial bends in ICA. Additionally, arc length is kept fixed which enables quantification of effect of the angle of curvature over a fixed segment size.

4.2.2. Discretization and Model Validity

CFD convergence criteria was a continuity residual of 10E-6. After convergence of the fluid domain, mesh refinement was employed across geometrical parameters of interest to

ensure mesh independence. Geometric parameters considered in the study were radial stent strut size, stent porosity, and parent vessel curvature. To cut down on computational need the lowest porosity was considered during mesh independence as it represents a change in the number of struts across the aneurysm neck (i.e. most complex geometry) and considered a reasonable approximation for the computational needs of all other porosity values. Mesh independence was calculated for average IA velocity across all strut heights and curvature values considered and are presented in Figure 4-2.

4.2.3. CFD and Computational Analysis

Basic CFD modeling for geometries presented here are very similar to the initial 2D strut modulation study, with changes in various parameters to account for modeling in the ICA versus the basilar artery. The vascular lumen was modeled as a rigid wall where the no-slip condition is applied, blood was modeled as a Newtonian fluid with density $\rho = 1060\ kg/m^3$ and viscosity $\mu = 3.5\ cP$. At the inlet an inviscid velocity boundary condition of $0.606\ m/s$ was chosen, corresponding to a volumetric flow rate of $4.6\ mL/s$; typical of the arterial segments being simulated (Bishop et al., 1986; Zarrinkoob et al., 2015). Upstream length was chosen to remove entrance and boundary layer effects ($L_{laminar} = 0.05ReD$) and downstream lengths where matched to account for any back pressure or recirculation from outlet boundary conditions too near an area of interest.

Given the same arguments used above (i.e. low Womersley number), flow was considered steady. Additionally, Reynolds number values are small within the vascular system and in this instance is on the order of 600, which also indicates that a laminar flow model is suitable.

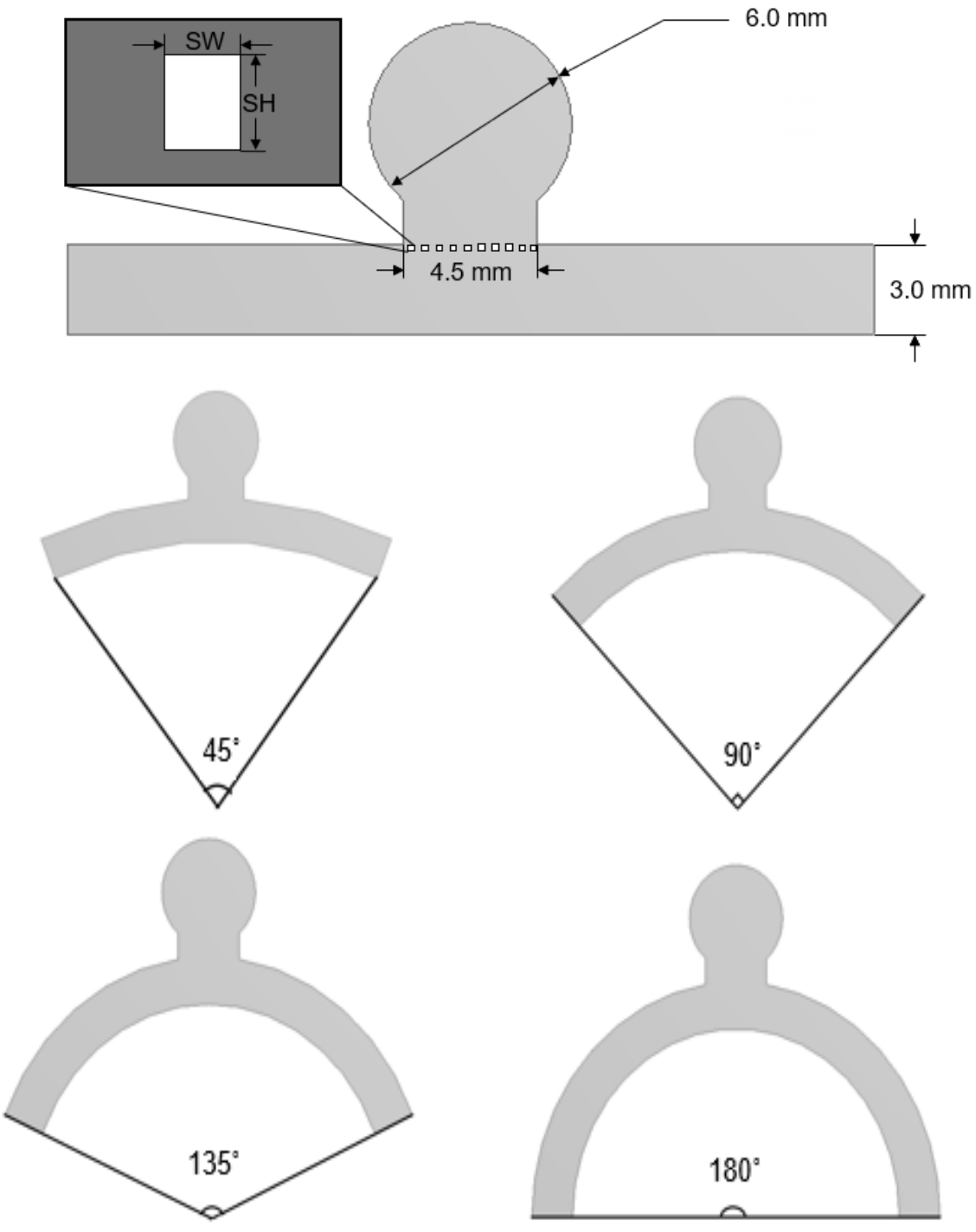

Figure 4-1: CFD geometric model considered. Side wall aneurysm and vascular parameters (a) and vascular curvatures considered (b).

The mesh was constructed using ANSYS Meshing 17.1 (Ansys, Canonsburg, PA, USA). Mesh independence was reached with saccular average velocity differences across mesh refinement of less than 5% or an absolute difference of less than $1\ mm/s$.

Porosity, vascular curvature, and strut height were varied simultaneously to assess the impact of strut size on intra-aneurysmal spatially-averaged velocity and wall shear stress. The spatial average of the velocity is defined as follows:

$$\bar{v} = \frac{1}{A}\iint_{ROI}|v|dy\,dx = \sum_{i=0}^{N}\frac{1}{A_i}\sqrt{u_i^2 + v_i^2} \qquad \text{Eq. 4-1}$$

Where u_i, v_i are the x and y components, or longitudinal and radial components respectively, of velocity respectively at the ith element, N is the number of elements and A_i is the area of the element at which the velocity magnitude is being calculated. Similarly, wall-shear stress is calculated as a weighted-average by element size, where the discretized differentials can also vary in size relative to the size of the elements near the wall:

$$\overline{WSS} = \frac{1}{s}\int_0^s \mu\left(\frac{du}{dy} + \frac{dv}{dx}\right)ds = \frac{1}{l_i}\sum_{i=0}^{N}\left(\frac{\Delta u_i}{\Delta y_i} + \frac{\Delta v_i}{\Delta x_i}\right) \qquad \text{Eq. 4-2}$$

As a control group, the average IA velocity and WSS were computed with no stent struts within the fluid domain in order to establish a baseline against which IA average velocity reduction (VR) and average WSS reduction (WSSR) are determined. Average reduction is

defined as the percent difference of a stented aneurysm (S) from the non-stented (NS) case seen below for a variable ϕ defined within the aneurysm.

$$\overline{Reduction_{\phi}} = \frac{NS_{\phi} - S_{\phi}}{NS_{\phi}} \times 100 \qquad \text{Eq. 4-3}$$

Previously this work postulated that SH as it pertains to fluidic shear transmission may be an important design parameter to consider for flow diversion given previous work by Bouillot et al.2015; who characterized pathological IA flow as shear-driven and therapeutic flow as pressure-driven. Our previous work confirmed the significance of SH in reducing IA flow at increased porosities under conditions that were intentionally selected to maximize shear's contribution to IA flow and to evaluate extreme differences in strut profile normal to the direction of flow. However, within these studies, strut geometries were not of clinically relevant size, and velocities and geometries were based on anatomical model with a lower prevalence of aneurysms. In order to translate these studies into a more realistic we've selected strut heights representing a range typical of stents and anatomical parameters more commonly encountered in aneurysm treatment. To further investigate the effects of radial strut growth and investigate the relationship between these parameters and inducing transitional flow regimes, velocity and WSS reductions are reported alongside snap shots of IA streamlines and contours for cases of increasing inertial driven motion, or aneurysm in the apex of highly tortuous anatomies.

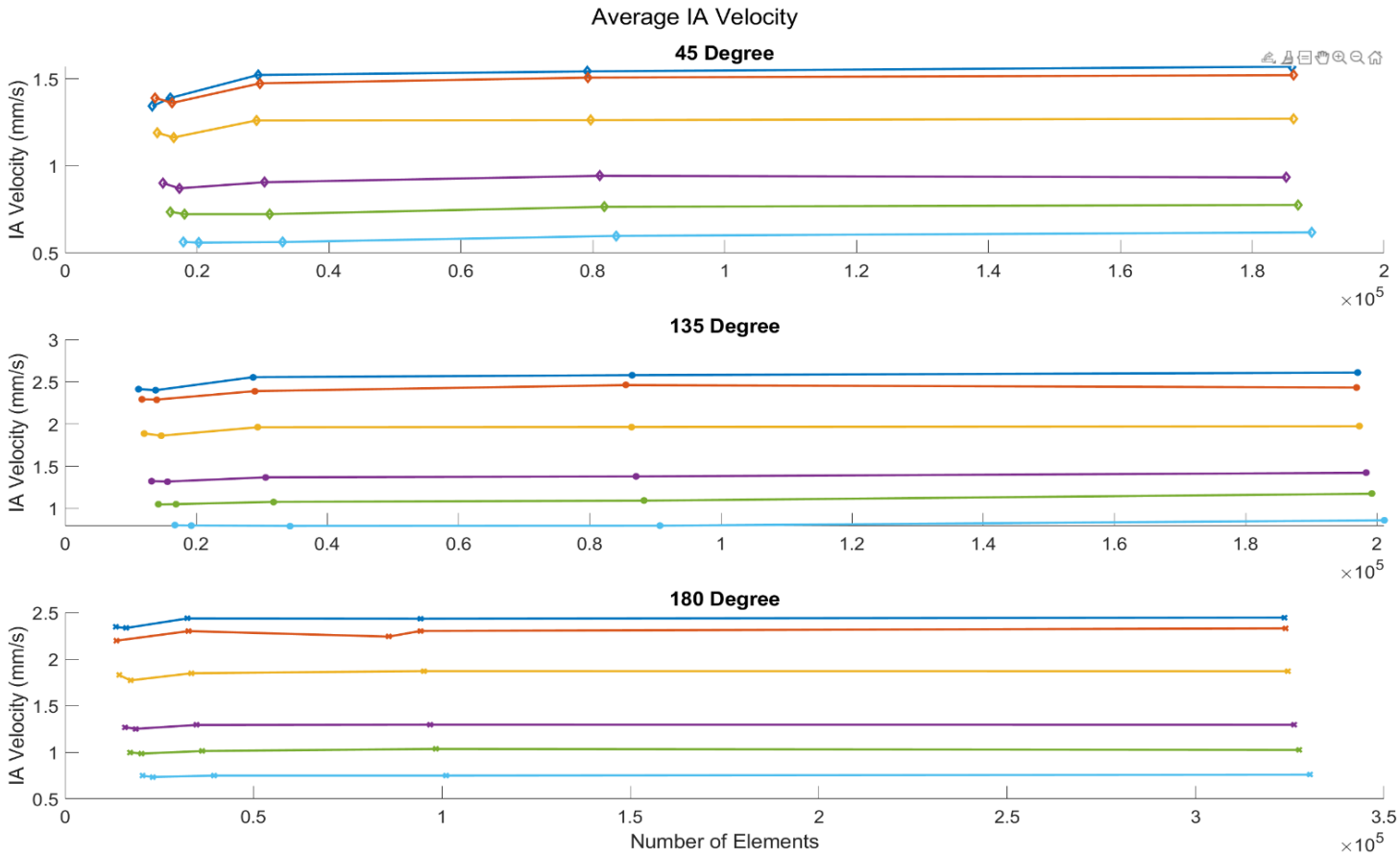

Figure 4-2: Aneurysmal midplane average velocity across mesh refinement for porosity 60 and curvature 45 (a), 135 (b), and 180 (c). Mesh independence is reaching for all geometries considered.

4.3. Results

Using ANSYS Fluent, IA average velocity and wall shear stress (WSS) were calculated for a range of vascular curvatures, strut heights and porosities in a 2D idealized sidewall aneurysm model. While much work has gone into understanding the effect of flow diverting stents on IA properties and much success has been made in utilizing this technology clinically, many unknowns still exist when devices are deployed in the clinic. Device efficacy is highly dependent on deployment technique, vascular structure at the lesion site and aneurysm geometry, all of which can change the effective porosity seen by the aneurysm. Therefore, it is reasonable to treat porosity as a random unknown variable within a range rather than static and to investigate the robustness of a device's parameters with respect to changes in the aneurysm when porosity is varied. Previous work done by the author indicated the potential for strut height to serve as a buffer to changes in porosity. In this way we've introduce the concept of porosity sensitivity, or the propensity at a given strut height for IA velocity and WSS reductions to change as porosity is increased. This work is extended here in a number of important ways. Firstly, smaller, more accurate design parameters are used to more accurately depict current FD used in the clinic, changing strut heights (0.05 - 0.45 to 0.03 - 0.15 millimeter) and strut widths (0.15 millimeter). Second, different anatomy was modeled to reflect the most direct application of flow diversion which happens primarily in the anterior circulation (specifically the ICA), changing vessel parent velocity (0.235 to 0.606 mm/s). Finally, the introduction of curvature to test for robustness of porosity sensitivity when curvature is increased as the neurovasculature in the Circle of Willis and around aneurysm is seldom straight, to

ascertain if strut height can serve a similar function in reducing IA response to changes in curvature, or if a conceptualization of curvature sensitivity can be made.

4.3.1. Comparisons Across Hemodynamic Velocities and Strut Size

As this work firstly expands and refines previous work done in understanding the role strut height plays in IA hemodynamics, a comparison across these data sets is made in Figure 4-3. Porosity sensitivity was analyzed for the zero-curvature case and is shown below the porosity sensitivity calculated in chapter 3 for the rectangular stent shape case. Porosity sensitivity is the average velocity reduction across all porosities for a given strut height. Fig 4-3 shows this value plotted relative to strut height non-dimensionalized by vessel diameter, where bars across each average value represent the range of velocity reductions from highest to lowest at the given strut height.

In the top plot of Figure 4-3 rectangular stent porosity sensitivity shows the same trends as elliptical cross-sections from Chapter 3, with growing strut height increasing the average velocity reductions across porosity and shrinking the range of values observed. In the bottom plot porosity sensitivity at a curvature of zero for the given study, also shrinking the rage of values observed as strut height increases, though reaching a maximum around aspect ratio 2, or strut height 0.06 microns before the range velocity reductions begins to increase. It can also be seen that the range of values and averages are very different between the two cases, with previous studies seeing much wider range, and much lower possible values for velocity reduction relative to the current model. To help understand these results velocity plots around stents were compared. Near strut field velocity plots across the two sets of experiments for both increasing porosity and increasing aspect ratio are presented.

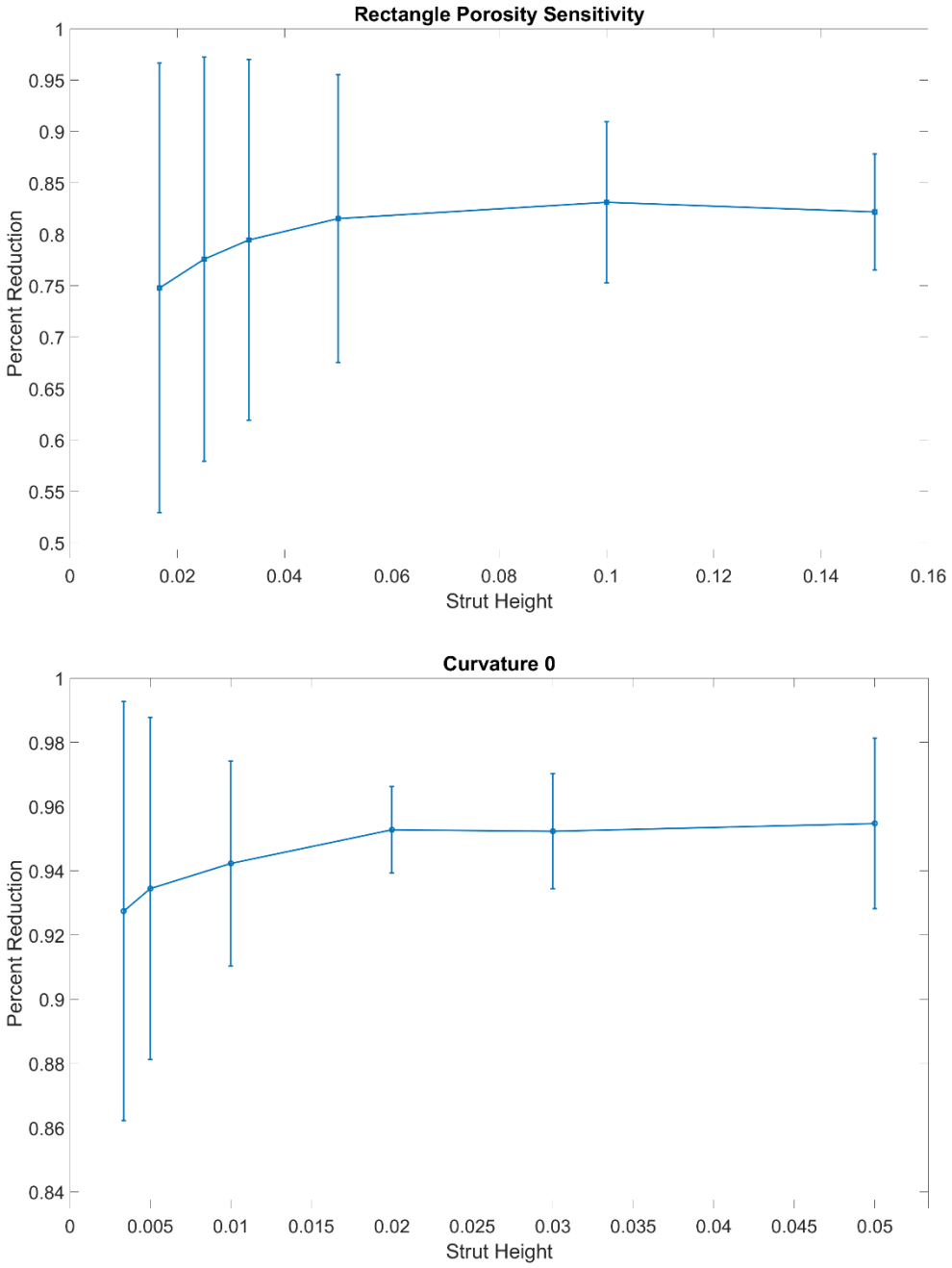

Figure 4-3: Porosity Sensitivity comparison between low velocity, low pore density (a) and high velocity, high pore density (b) relative to nondimensionalized SH. Bars are not error but represent range of velocity reductions observed at a given strut height. Results indicate that SH relative to device parameters and not anatomy is what drives behavior. Nondimensionalized values are very different but aspect ratio of struts is very similar.

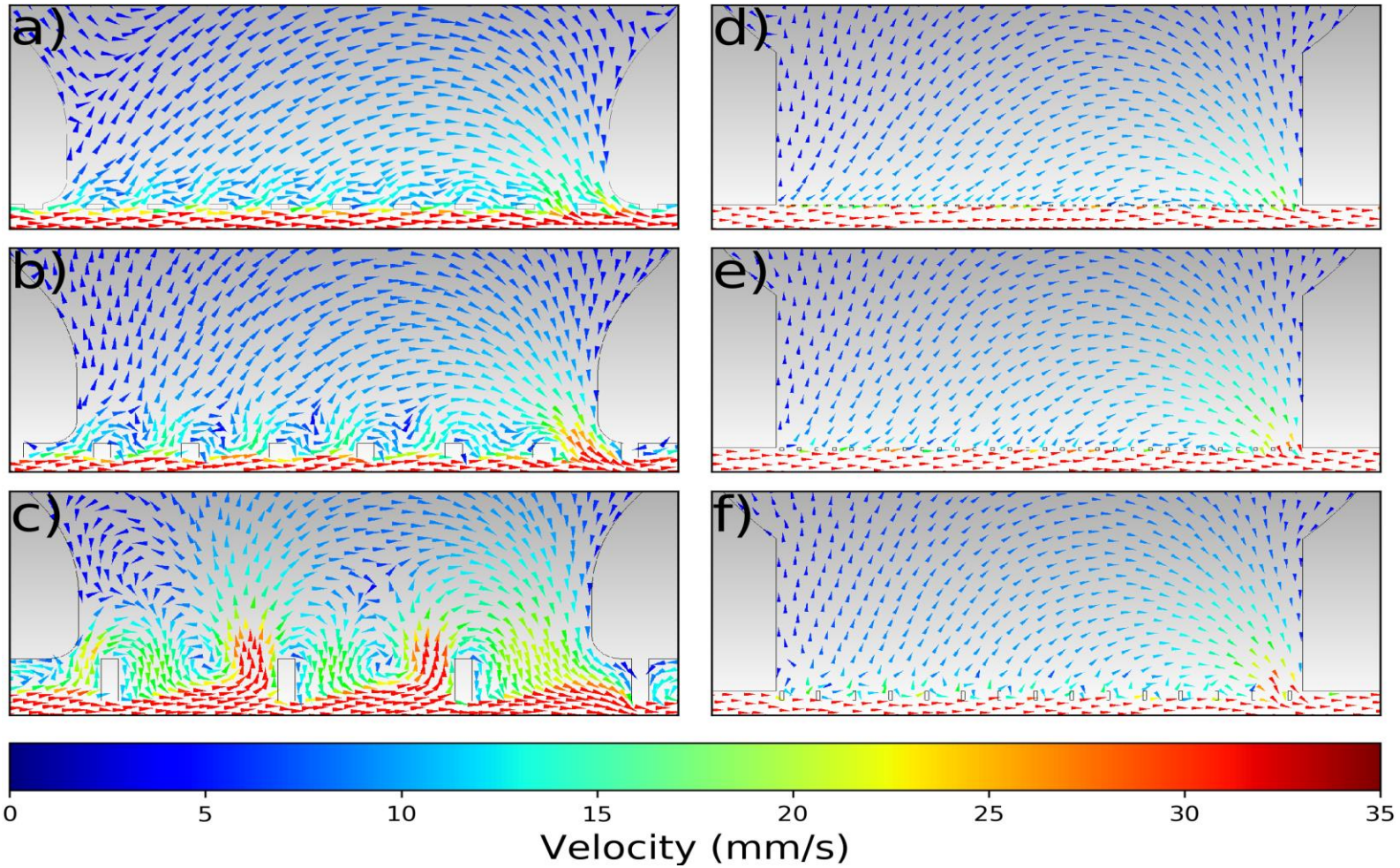

Figure 4-4: Near strut, aneurysmal neck velocity field comparisons between low velocity low pore density (a, b, c) and high velocity high pore density (d, e, f). Better alignment of flows across porosities when shear is reduced due increased pore density (d, e, f).

These plots illustrate the ability for growing strut height to help maintain velocity reductions when porosity is increased by angling flow into the aneurysm sac, disturbing the increase of shear transmission and resulting aneurysmal vorticity allowing flow to realign with the parent at the distal aneurysm opening as discussed in chapter 3.

Velocity fields in Figure 4-4 also illustrate the differences observed in porosity sensitivity. In previous studies strut parameters were very large, resulting in equivalent porosity values across cases but vastly different pore density. As the operating principle of FDs is to reduce shear transmission pore density is an important factor, though not deterministic, as has been observed within the literature (Hodis et al., 2016; Sadasivan, Cesar, Seong, Rakian, et al., 2009; Sadasivan, Cesar, Seong, Wakhloo, et al., 2009). In the low pore density case, velocities are higher, and the range of values is greater. Flow bounces around the struts at large porosities and growing strut height due to the balance of pressure driven radial forces and shear transmission driven longitudinal forces across the aneurysm opening. When shear is reduced enough, by significantly reducing pore density, flow is instead directed into the aneurysm sac even at very high porosities. Recirculation is seen for the current study where strut aspect ratio is very high (5) sending flow angled back proximally, nearly showing the near strut bouncing behavior observed previously.

4.3.2. Effect of Aspect Ratio and Vascular Curvature

Vascular curvature is a major driver of aneurysm growth and rupture and is also responsible for potential changes to effective porosity during device deployment in the clinic (Hoi et al., 2004). Growing SH has previously shown to be a potential design parameter which reduces variance in IA flow properties associated with treatment outcome as porosity is varied. Given the clinical need for devices with predictable performance across a wide range of

anatomical morphologies and the known impact of curvature, porosity sensitivity was tested against a range of curvatures shown in Figure 4-1 to test for its robustness in a more complex geometry and more clinically relevant context. Curvatures of 45, 90, 135, and 180 degrees were tested, and porosity sensitivity reported for each in Figure 4-5. SH shows the same trend across all curvatures, though of varying strength. As SH grows PS is reduced and average velocity reduction across porosities increased. As curvature is increased, and thereby the longitudinal component of velocity which affects shear-transmission is decreased, porosity sensitivity is increased for all SHs, though most notably for those above the seeming optimal value of approximately AR 2. The average velocity reduction across porosities does not go down for any curvature tested.

Figure 4-6 shows IA streamlines for the high medium and low cases of SH and curvature, moving down and to the right respectively. A porosity of 80 was chosen to report as this range of porosities has been shown by others to have a dearth of experimental data due to the lack of available devices and for which the transition from high shear driven IA motion to pressure driven has previously been observed (P. Bouillot et al., 2015; P. Bouillot et al., 2014).

Figure 4-6 indicates that increasing SH for any given curvature extends the realigned flow deeper into the aneurysm neck, eliminating more of the rotational flow in the aneurysm sac, while inducing higher velocities at the inlets and outlets. As curvature increases for any given strut height the strength of the inlet at outlet velocities grow. Given the impact SH has on modulating an aneurysms sensitivity to changes in porosity, this concept was tested against curvature as well.

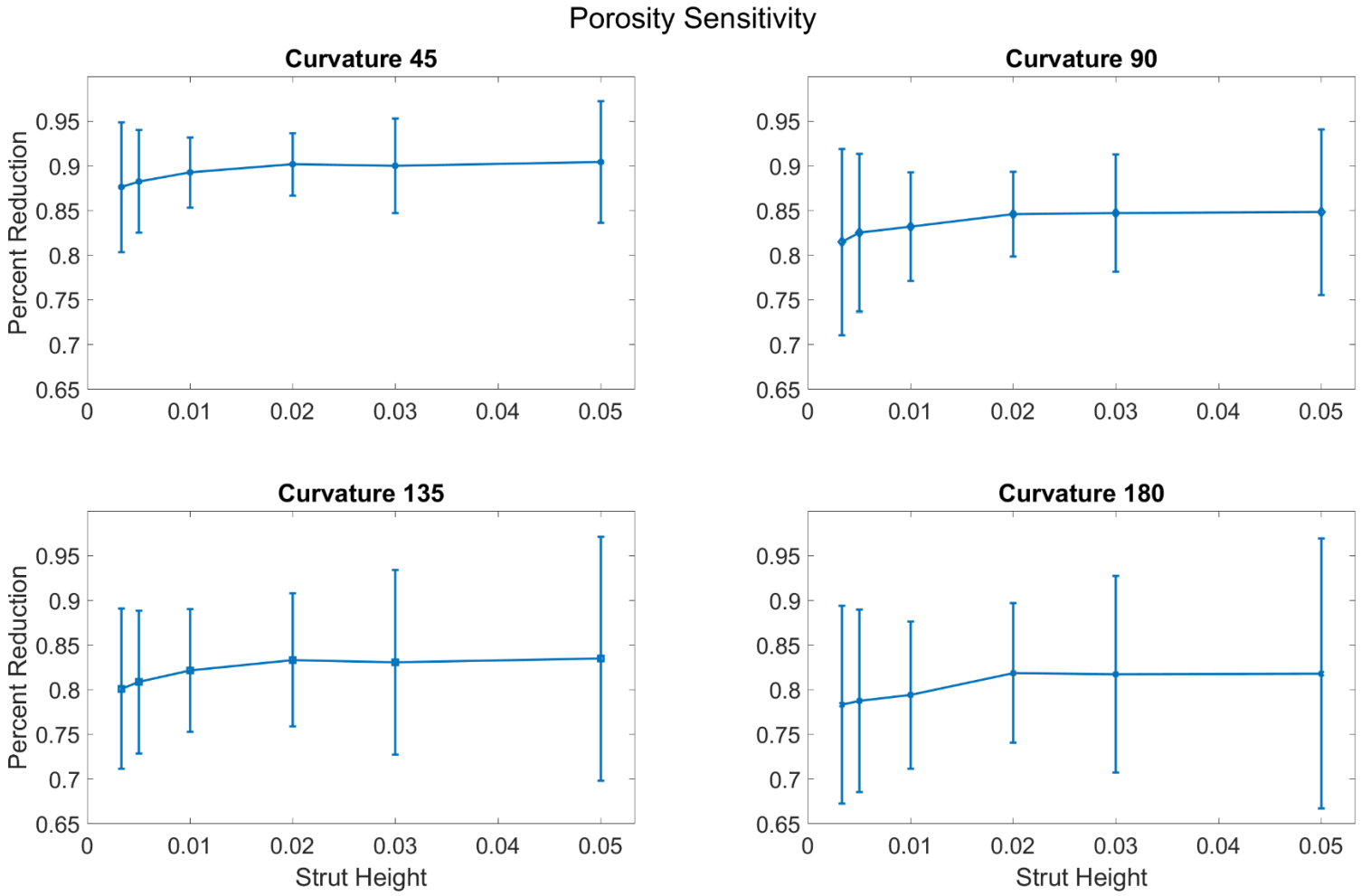

Figure 4-5: Porosity sensitivity for all curvatures considered. Curvature diminishes SH impact on porosity sensitivity.

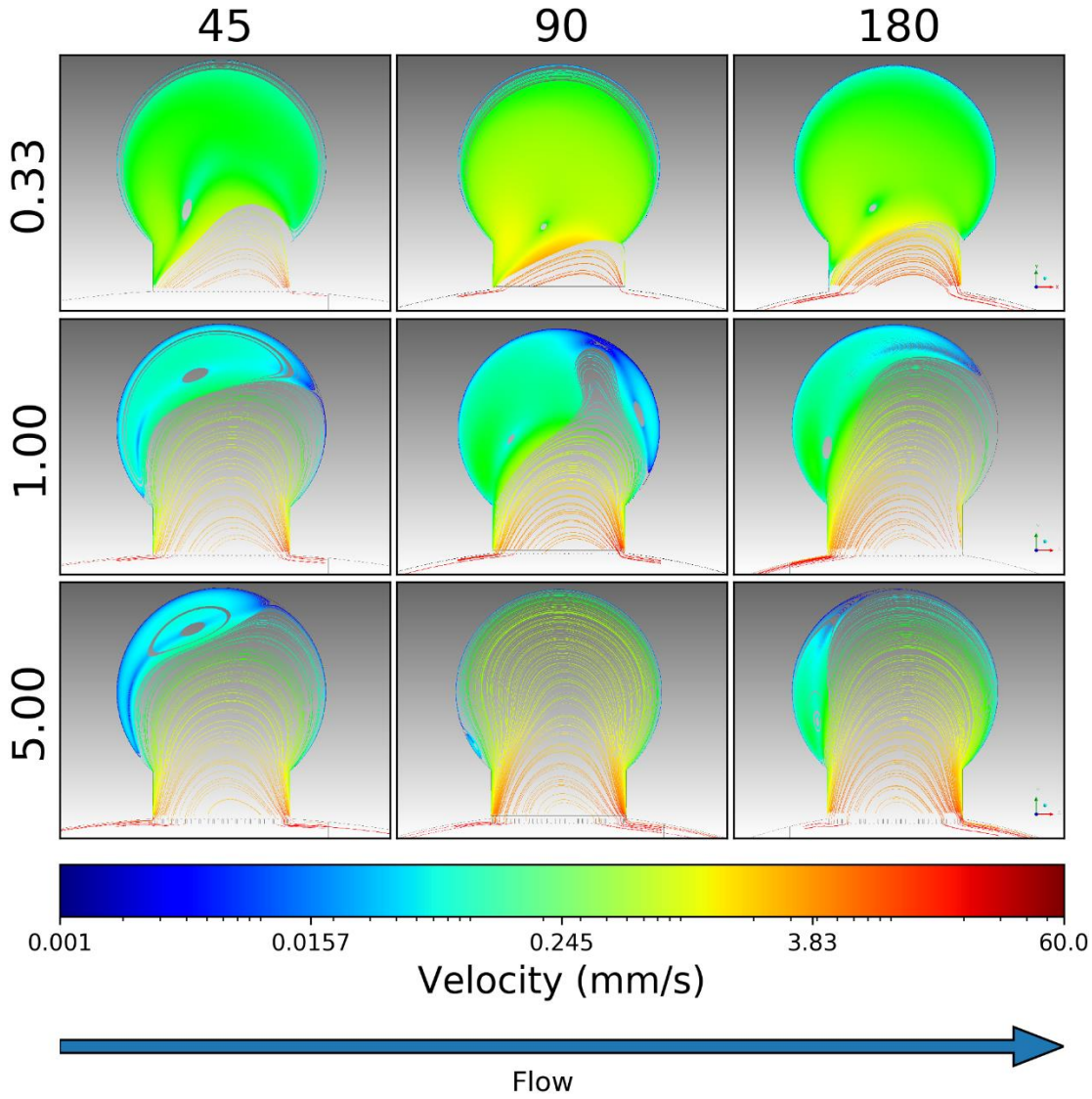

Figure 4-6: Aneurysmal midplane streamlines for low, medium and high aspect ratio (vertical) as well curvature (horizontal). Increased curvature increases inertial forces into aneurysm and SH does as well. These forces work together to shift the vertex of rotation within the aneurysm or to completely eliminate it with higher velocity inertially driven fluid.

Figure 4-7 represents IA velocity reductions in terms of curvature sensitivity (i.e. variance in velocity reduction for a given strut height when grouping across all curvatures considered in this study). Each point is the average IA velocity for the given porosity across all curvature cases considered for a given SH, and bars represent the range of velocities values observed therein. Four porosity values were examined and curvature sensitivity measured for each. Increasing SH had a largely negligible effect on curvature sensitivity though interesting patterns arise.

At low porosities increasing SH was advantageous, causing a decrease in the range of values observed across curvatures and increasing the average reductions therein. At 80 percent porosity and above SH effect on curvature is varied. At 80 percent curvature sensitivity is slightly increased and average velocity reduction slight decreased as SH grows, remaining largely static. At 90 percent the range of velocity values remain neutral with slightly increasing average values observed up to the AR 2 area where averages come back down and velocity ranges expand out.

4.4. Discussion

Data was gathered on the efficacy of a radial strut height (SH) in manipulating IA properties and flow profiles. These results were compared to earlier studies to ascertain if conclusions about the interaction of strut height and IA shear transmission held under conditions more representative of current clinical practice. In addition, these studies were expanded to consider the effects SH had in the context of vascular tortuosity. Comparisons to earlier work considered a number of important differences.

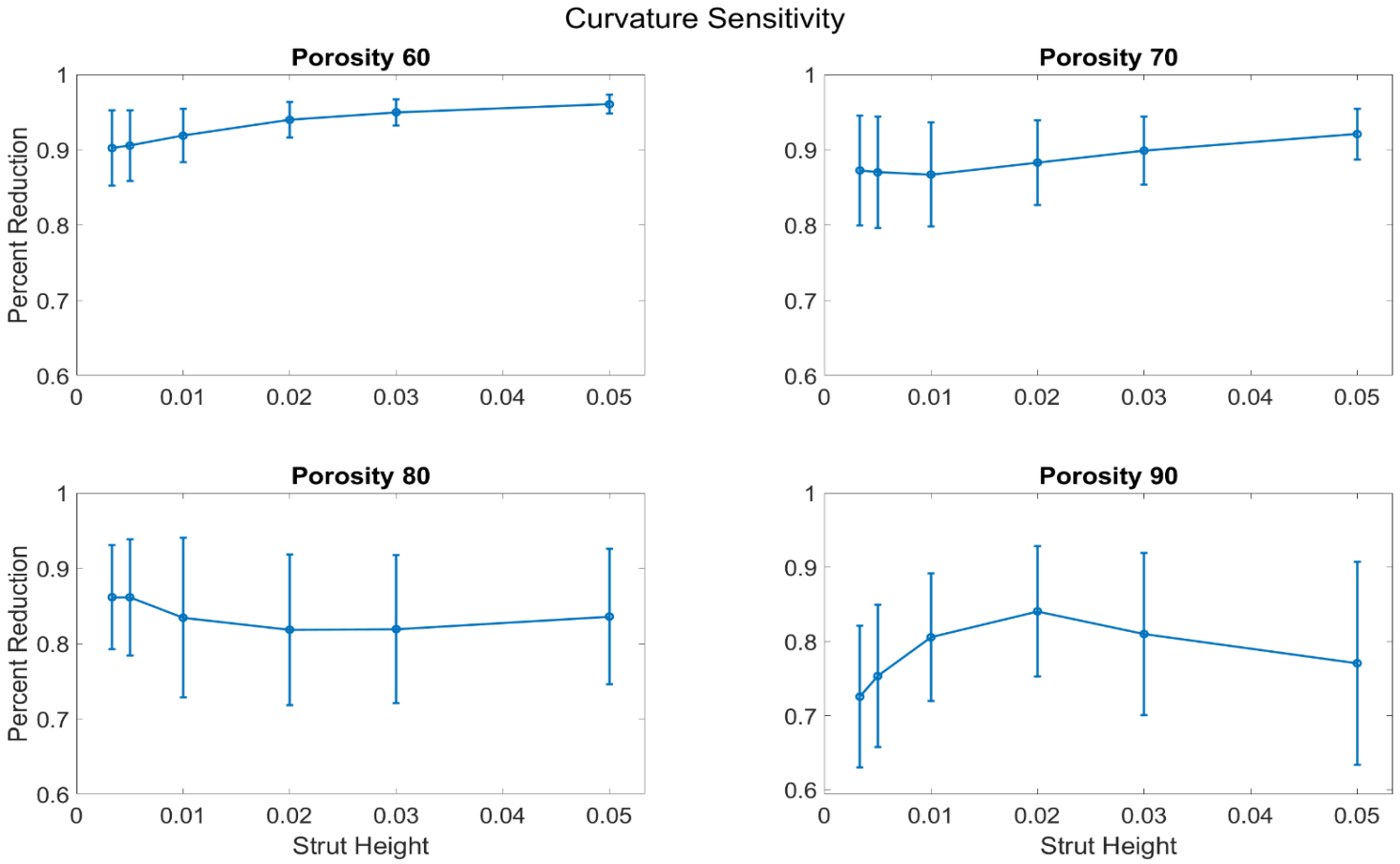

Figure 4-7: Curvature sensitivity for every porosity considered where bars represent not error but the range of velocity values across all curvatures for a given strut height and porosity. SH does not significantly change aneurysmal response to changes in curvature.

Struts were made much smaller to more accurately represent clinically available devices and arterial velocity was increased to model the ICA where aneurysms are more common, and devices are currently indicated for use.

Strut heights were reported in non-dimensionalized by parent arterial diameter due to hypothesis that that flow reduction is a largely function of how far a strut protrudes into the parent artery and interacts with the flow field as it varies across the arterial diameter and that this would be a function of arterial size. Though not definitive, data shown here calls into question that reasonable assumption as both plots share a very similar trend for increasing strut height despite the order of magnitude difference between studies in SH's examined. This data suggests that AR and pore density are driving behavior and not the size of a strut relative to the parent vessel. This has interesting consequences when considered alongside existing efforts to apply Darcy's Law to models of intracranial flow diversion. Since pore density per unit area was shown to be significant even for equal porosities, and AR was more impactful than SH relative to parent artery this implies the existence of a certain length-scale above which the use of Darcy's Law is inappropriate. An important caveat to this analysis is that the difference in parent artery velocities between cases is nearly 3 times, exactly how this translates to the effect of strut height remains to be seen.

Differences observed between the two cases (fig. 4-3) were magnitude of reductions, the rate of decrease in sensitivity observed and the range of the SH values which decrease sensitivity. All are a function of pore density and the greater reduction of shear. Reduced shear transmission means greater reductions between cases. The previous study

showed a continued decrease in sensitivity while the current had two regions: the first up to an aspect ratio of 2 where sensitivity decreases as SH increases and after AR 2 where sensitivity trends back upwards. Additionally, the region of decrease in the current model was much stronger and happened faster than observed previously. These differences, when taken with the large increase to pore density between cases, can be understood given the previous hypothesis of shear transmission reduction and radial pressure gradients at the proximal and distal edges of the aneurysm opening as the operating principle behind the effect of SH. When pore density is not high enough to reduce shear to significant levels SH serves to continuously disrupt aneurysmal velocity fields. This provides a reduction in sensitivity but when reduced allows pressure to much more significantly impact IA velocities reach a point were in-jets into the aneurysm are too great and reduce efficacy of the device. Also allowing SH to more acutely effect IA properties and flow profiles otherwise.

Figure 4-4 further illustrates this point. When observing near strut and aneurysmal entrance velocity fields for the two cases high rotational motion is observed much lower in the aneurysm neck for the low pore density cases. Only when SH is very high is enough fluid pushed further upwards and even then, shear dominates. This is observed as the aneurysmal opening/ near strut bouncing motion. For the current study no rotational motion is observed in the region of interest.

When considering porosity sensitivity across curvatures (fig. 4-5) within in this paradigm of shear vs pressure it is clear that curvature in this context enhances flow into aneurysm, changing the energy balance from one dominated by shear to one dominated by

inertia. This reduces the effectiveness of increased SH, and even potentially reverses this effect to direct more flow into the aneurysm, further diminishing porosity sensitivity. From Figure 4-6 it can be seen that flow profiles across curvatures does not change much regardless of SH, and that increased SH is still largely advantageous even at higher porosity values where the increase to range of IA values and subsequent increase in porosity sensitivity is largely a function of the inlet and outlet velocities.

Curvature sensitivity was measured to test the robustness of a device deployed within the context of high variant neurovascular context. SH was advantageous across all values for porosities of 60 and 70, and largely neutral across all SH values at porosity 80 and 90. At increased SH there is also significant difference in the projected porosities on the luminal and abluminal sides. This has the effect of reducing the flow rate of high inertial flow into the aneurysm. At low porosities this, along with the reduction of shear, are responsible for reducing curvature sensitivity. At high porosities these changes in effective inertial porosity is not enough to significantly reduce the rate of inertia thereby washing out this effect.

Overall, these results point further to SH and perhaps more importantly AR as important design parameters which could be used in the clinic to reduce uncertainty in the IA hemodynamic response when a device is deployed. Additionally, this may be a mechanism for device designers to create devices with higher porosity. As we learn more about the specifics of aneurysmal factors that contribute to the best outcomes, reducing uncertainty in IA hemodynamic performance may be a manner by which to isolate and further investigate them.

5. 3D HIGH ASPECT RATIO NOVEL STENT DESIGN: A COMPUTATIONAL AND EXPERMENTAL COMPARISON

5.1. Introduction

In general, flow diverters have been successful in the treatment of intracranial aneurysms. However, the efficacy of these devices is limited given their tendency to divert flow from healthy structures in the vicinity of a lesion site. In this study, we show the potential for diverting flow selectively via an alternative approach in which high-aspect ratio microscale structures are intentionally designed to work congruently with an intermediate porosity flow diverter. We demonstrate this design principle by implementing a microfabricated flow diverter with finely controlled cross-sectional elements. Experiments performed using an *in vitro* basilar trunk model yielded comparable intra-aneurysmal flow reduction compared to commercially available flow diverters. More importantly, the effect on flow into "jailed" perforating arteries was minimal (i.e., nearly eight-fold lower perforator flow reduction than commercial devices). Our results highlight the potential to use our new generation flow diversion device in more delicate structures within the neurovasculature, which currently lack a treatment option.

Stroke is the fifth leading cause of death in the United States. Hemorrhagic subtypes, typically arising from the rupture of intracranial aneurysms (IAs), comprised approximately an eighth of all cases in 2016, for example, with the remainder being ischemic. Despite their reduced prevalence, hemorrhagic strokes are significantly more deadly, with a mortality rate of approximately one third and significant morbidity associated with an additional third of all cases (Benjamin et al., 2019). Even though the remote location of these pathologies has historically required highly invasive treatments (i.e., craniotomy), the past three decades have seen promising developments in minimally invasive approaches (i.e., endovascular catheterization). In particular, Flow Diverters

(FDs) have proven to be a good alternative for treating a broad patient segment while resulting in a smaller range of complications than predicate techniques, such as aneurysm clipping or coiling.

FDs are densely-braided, stent-like, mesh cylinders that are endovascularly deployed across the neck of an aneurysm within the parent artery. These devices reduce the shear rate into the aneurysm, transiently induce thrombosis, and finally act as a scaffold for neointimal growth, which occurs once the thrombosed aneurysm is excluded from the circulation. Unlike conventional vascular stents, FDs require a much higher degree of metal coverage to induce thrombosis, and thus, are characterized by lower porosity (i.e., ~70% instead of the ~93% porosity typical of stents) (Dong et al., 2011). However, current FD designs must strike a fine balance when it comes to this design parameter since aneurysms frequently arise next to healthy vessels. FD porosity must, therefore, be low enough to significantly reduce flow into the aneurysm, but also high enough to allow radial pressure-driven flow into perforating arteries whose inlet may be covered by the device (referred to as "jailed" perforators).

Scientific investigations have elucidated that decreasing porosity increases the efficacy of flow diversion, but have mostly focused on characterizing flow diversion as a function of porosity in highly symmetric devices — a current clinical challenge since flow is equally decreased to lesions as to neighboring healthy anatomy (Dong et al., 2011; Y. H. Kim et al., 2010). Clinically, this lack of discrimination has restricted FD use to regions with arteries of large diameter and high volumetric flow rates, which are more robust to jailing. However, this excludes the treatment of posterior segment lesions, which constitute

a significant component of the patient population. While there have been reports of off-label FD use in regions characterized by smaller vessels, the prognosis for perforating arteries remains poor (Adix et al., 2017; Bhogal et al., 2017; Lall et al., 2014; Phillips et al., 2012; Siddiqui et al., 2012; van Rooij & Sluzewski, 2010).

Furthermore, recent computational studies on the optimization of FD response have been limited by the underlying assumption that devices leverage available fabrication techniques, i.e., wire braiding. As such, these studies have primarily focused on macroscale characteristics of large symmetric assemblies; namely braid porosity (Janiga et al., 2015; M. Zhang et al., 2016; Yue Zhang et al., 2019). Here, we demonstrate that IA flow diversion can be achieved while sparing perforators by increasing the local anisotropy of the device. We show that high-porosity FDs with high-aspect ratio struts can produce flow reductions comparable to commercial FDs in aneurysm morphologies in which IA flow is largely shear-driven while producing significantly less flow diversion in so-called jailed perforating arteries.

In the following sections, we present our newly developed FD, devised from a ground-breaking microfabrication technique adapted from semiconductor manufacturing to titanium, a well-understood biomaterial (Aimi et al., 2004; Parker et al., 2005; Woo et al., 2017). Traditional devices consist of fine round wires, which repeat frequently enough to reduce IA velocity. In contrast, our design consists of high-aspect ratio struts that divert flow selectively away from diseased tissue while allowing flow into healthy vessels. As a result, comparable reductions to standard prostheses is achieved with few struts, thereby decreasing the amount of metal coverage required as well as the risks associated therewith,

e.g., ischemia/infarct, inflammation, nickel sensitivity. This may offer a means to alter the risk profile of this treatment as to extend flow diversion therapy into a broader patient population.

5.2. Methods

5.2.1. Experimental Methods

Experiments were conducted by inducing flow through the silicone models using a circulating pump (GA Model, Micropump, Vancouver, WA) at 100 mL/min. The flow field through the aneurysm sac and perforating artery were quantified via two-dimensional particle image velocimetry (PIV). Similar to previous hemodynamic studies, a 60:40 deionized water-glycerol solution was employed with a viscosity and density similar to that of blood (3.5 cP, and 1080 kg/m^3, respectively). The viscosity of the solution was quantified using a Cannon-Fenske viscometer tube (Sigma Aldrich, St. Louis, MO). Prior to experiments, the water-glycerol solution was seeded by adding and thoroughly mixing a stock of neutrally buoyant fluorescent polystyrene microspheres (10.3 μm, maximum emission wavelength of 584 nm; PSF-010UM, Magsphere, Pasadena, CA) to the water-glycerol solution at a concentration of 2% by volume. The particles were excited using a 527 nm double-pulsed Nd:YLF laser (DualPower 10-1000, Litron, UK). The model was illuminated from below by coupling the laser head to an optical collimator via a liquid light guide (Fig. 1). High definition video was acquired at 1450 Hz using a high-speed CMOS camera (SpeedSense VEO640, Vision Research, Wayne, NJ) and a 2.5x zoom lens oriented such that the focal plane coincided with the mid-plane of the model. In each experiment, a total of 750 frames (approximately 0.5 s) were collected at a resolution of 2560 × 1660 pixels. Instantaneous velocity fields were retrieved by processing the raw PIV

image sequence using DynamicStudio (Dantec Dynamics, Holtsville, NY). First, images were pre-processed by subtracting the entire image set's temporal mean from each frame. Next, images were masked outside the region of interest by setting all pixel values to zero. Consecutive image pairs were then cross-correlated using a three-pass adaptive PIV algorithm with interrogation window sizes of 256, 128 and 64 pixels and overlaps of sub-pixel displacements were estimated using a Gaussian curve fit. Finally, spurious vectors were excluded by implementing a standard normalized median filter in a 3×3 neighborhood with eta = 0.2 (Meinhart et al., 2000).

5.2.2. Computational Methods

Numerical simulations were performed to characterize the hemodynamic effect of implantation of a HP-FD. The steady-state Navier-Stokes equations were solved using the SIMPLE (Semi-Implicit Method for Pressure-Linked Equations) algorithm in ANSYS FLUENT (Canonsburg, PA). The mesh was constructed using ANSYS Meshing 17.1 (Ansys, Canonsburg, PA, USA). Mesh independence was reached with saccular and perforator average velocity differences across mesh refinement of ≤4% seen in Figure 5-1. A tetrahedron-dominant mesh was used in the stent-deployed geometry and the aneurysm sac, with had a five-layer boundary inflation at the wall resulting in meshes of 15 million and 7 million elements for Conv-FD and HP-FD, respectively. PED-HD required very high elements to be fully realized and mesh independence of 4% achieved with only 3 iterations of mesh refinement due to the very computational cost of meshing a fully realized 3D PED model. Model parameters were based on values typically encountered in the posterior circulation (Bogren et al., 1994; Buijs et al., 1998).

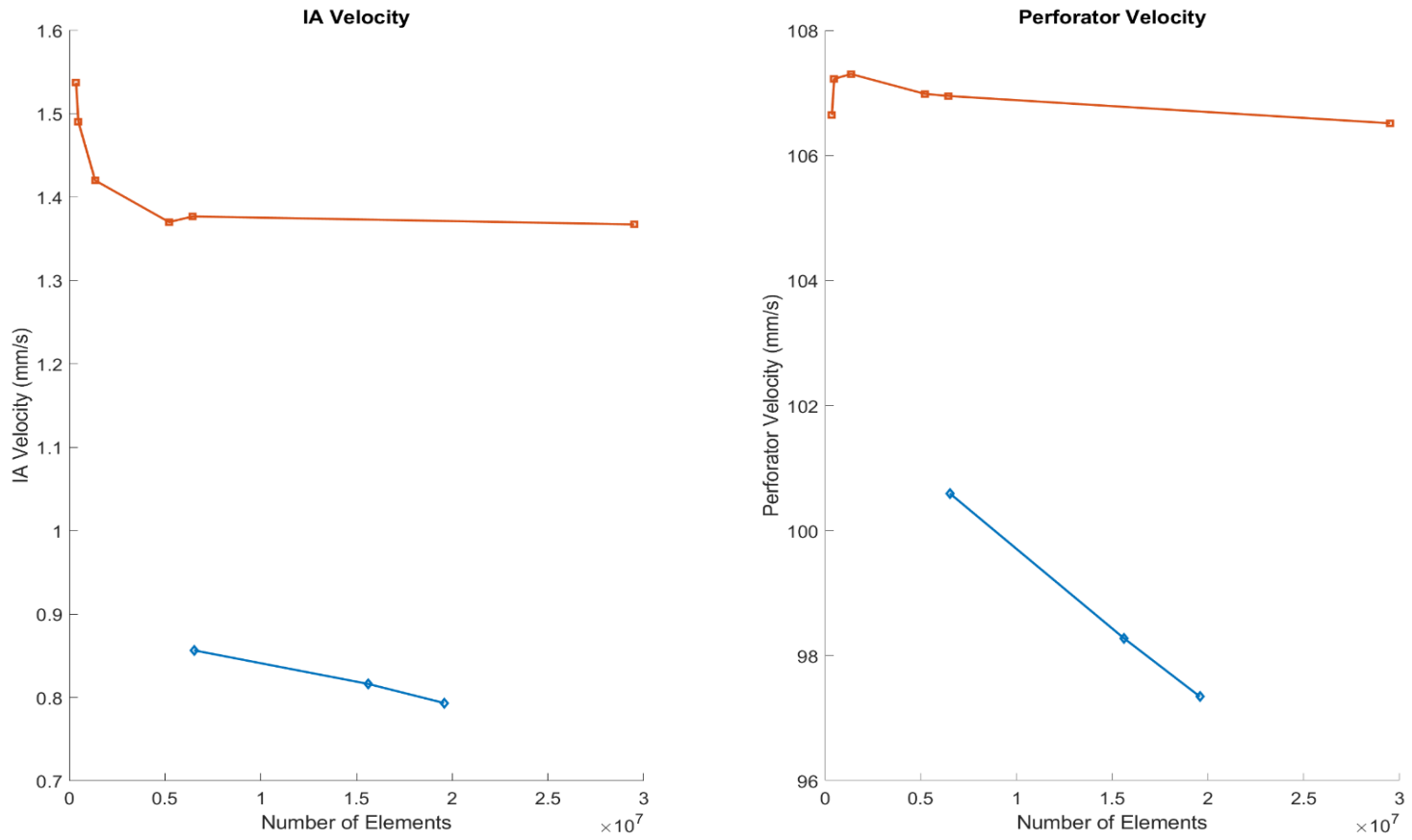

Figure 5-1: Aneurysmal and perforator midplane average velocities across mesh refinement for the high aspect ratio device and the conventional flow diverter. Mesh independence is reached for both within acceptable ranges of error. Experimental comparisons were used to further validate CFD.

Vascular geometries were matched to experiments by using the Solidworks (Solidworks, Concord, MA) design files from which the silicone models were fabricated. The vascular lumen was modelled following standard practice as a rigid non-slip wall given the negligible distensibility of the cerebral vasculature. Boundary conditions at the inlet and outlet were imposed as a constant velocity of 23.5 cm/s, corresponding to a volumetric flow rate of 1.6 mL/s (typical of the arterial segments being simulated (Lindegaard et al., 1987)). The upstream length was chosen to remove entrance and boundary layer effects, $L_{Laminar} = 0.05ReD$. Blood was modeled as a Newtonian fluid with density ρ = 1064 kg/m^3 and viscosity μ = 3.5 cP (Kenner et al., 1977; Peter W. et al., 1964). Even though blood is known to exhibit non-Newtonian properties, largely due to viscoelastic effects arising from the increased volume fraction of hematocrit in smaller vessels, these effects are negligible at the diameter ranges considered in this study(Waite & Fine, 2007). This simplification has been used widely in computational modelling of intravascular stenting (Aenis et al., 1997; Y. H. Kim et al., 2010; Ohta et al., 2005; Valencia & Solis, 2006) and has been validated experimentally (Cho & Kensey, 1991; LaBarabera, 1990).

The Womersley number is a measure of dynamic similitude used commonly within the vascular system to describe the viscous damping behavior of blood relative to the time-varying pressure gradient induced by the heart. This number is defined as $\alpha=a\sqrt{(\omega\rho/\mu)}$, where a is the radius of the artery, ω is the frequency of the pulse wave, ρ and μ are the density and the dynamic viscosity of blood, respectively. For typical heart rates (between 60-100 bpm) this value is less than two in the neurovasculature; indicating that the flow is dominated by viscous forces rather than oscillating inertial forces (i.e. the flow is quasi-

steady). Flows within this regime have a parabolic velocity profile at peak flow rate and a peak flow rate which is roughly 80% of the steady-state flow rate which would be observed for the same pressure gradient (Womersley, 1955). In contrast, for $\alpha > 2$ the fluid core is dominated by inertial forces and toward the centerline has a much more uniform velocity distribution than near the walls, where these values rapidly approach the no-slip condition (i.e. velocities are zero). Flows at high Womersley numbers also have peak flow rates that are significantly lower than steady-state flow rates under the peak pressure differentials. Since this study is largely concerned with the resulting changes to IA properties resulting from fluid shearing against stent struts near the vessel wall, a steady-state model using the volumetric flow rate near peak systole was considered as a conservative but appropriate estimate to compare the effects of device geometry on the time-averaged magnitudes of fluid mechanic parameters relating to aneurysm rupture (Barnes et al., 1971; Perktold et al., 1984).

Finally, the parent artery was set to zero gage pressure (as is common in the literature) and the perforator outlet to -120 Pa to ensure that all cases match the non-stented perforator mass flow quantified in lab experiments (Anzai et al., 2015; Moon et al., 2014; Vignon-Clementel et al., 2010; J. Xu et al., 2015). For comparison, studies with Womersley Numbers of 13-22 have observed significant differences in wall shear stress between steady-state and pulsatile models arising from differences between pulsatile and steady-state flow as well as time-dependent phenomena, e.g. vortex nucleation and decay (Yu, 2000). Nonetheless, as the overarching objective of this study is to develop relative

measures for device characterization, a steady-state model was considered appropriate as a first-pass technique for analysis of device performance.

5.2.3. Experimental and Computational Comparison

The spatially averaged velocity magnitude was computed within the region of interest (e.g. aneurysm, perforator) for each case:

$$\overline{v} = \frac{1}{A}\iint_{ROI} |v|\, dx\, dy \qquad \text{Eq. 5-1}$$

where v is the velocity vector, A is the area of the region of interest, and x and y are global cartesian unit vectors. Equation 5-1 was evaluated numerically within the aneurysm boundary using the PIV/CFD vector spacing to discretize the domain. Using these values for the control and FD-implanted cases, the percent reduction in intra-aneurysmal velocity was computed as:

$$\%\, reduction_{velocity} = \frac{\overline{v_{control}} - \overline{v_{FD}}}{\overline{v_{control}}} \qquad \text{Eq. 5-2}$$

In addition, wall shear stresses (WSS) were also quantified to evaluate the effect of FD-implantation on the vessel wall. These stresses were calculated by first obtaining the shear rate in the fluid. For simple shear in Newtonian fluids in two dimensions, this value is given by the relation:

$$\dot{\gamma} = \frac{\partial v}{\partial x} + \frac{\partial u}{\partial y}. \qquad \text{Eq. 5-3}$$

Wall shear stress is then derived from the shear rate using the following relation:

$$\tau_w = \dot{\gamma} \cdot \mu . \qquad \text{Eq. 5-4}$$

An edge detection algorithm was used to determine the boundary and a cubic spline curve was fit to the resulting coordinates. The fluid shear stress tangent to the wall was calculated by determining the tangential components of the U, V velocity components (in global coordinates) to each point along the fitted boundary. Eq 3 was discretized using the central difference method and solved within the entire fluid domain using the vector spacing from the resultant PIV and CFD velocity fields to experimentally validate the model. The max and average wall shear stresses were then reported from ANSYS.

5.3. Results

5.3.1. Device Design and Operating Principles

Conventional FDs rely on an axially and radially symmetric braided assembly of wires with fine circular cross-section (hereafter referred to as Conv-FDs) whose pitch defines the device porosity (i.e., percent open area within a 2-D unit cell projection), and thus, its performance (Stancampiano et al., 1997). Owing largely to the braided construction of Conv-FDs, porosity has been shown to be highly sensitive to local variations in anatomy and deployment technique, which makes the optimization of these devices difficult (Shapiro et al., 2014). In this study, we have developed a solid-construct device with a

fixed, intermediate porosity (Fig. 5-1a). Roughly halfway between a conventional stent and an FD, our device leverages principles from a regime previously unexplored for flow diversion, but which has shown great potential both clinically and experimentally (P. Bouillot et al., 2016). Moreover, rather than relying solely on the porosity of the assembly to divert flow, our high-aspect ratio design selectively reduces IA velocity while enabling a greater mass flow rate into perforating arteries than conventional devices. This is enabled through the implementation of high-profile struts, which increase microscale impedances to shear-driven flow along high-porosity structural elements by creating flow separation zones at strut trailing edges.

Numerical studies have shown that rectangular cross-sectional struts positioned normal to the direction of the flow induce downstream flow separation that increases with strut aspect ratio (Duraiswamy et al., 2007; Jiménez & Davies, 2009). These numerical analyses, done in the context of coronary stenting, suggest that minimizing the strut aspect ratio reduces the effect of the device on the local hemodynamics and thus the potential for thrombogenic cues near the vessel wall (e.g., low shear, recirculation). However, in the context of neurovascular flow diversion, the goal is to intentionally create thrombogenic cues intra-aneurysmally by significantly altering the local hemodynamics across the neck of an aneurysm. Therefore, it may be more advantageous in this application to *increase* the aspect ratio of struts, to produce the largest amount of fluidic resistance and induce flow separation across this region.

Until recently, constraints in machining resolution have precluded an experimental evaluation of the effect of strut aspect ratio on FD performance.

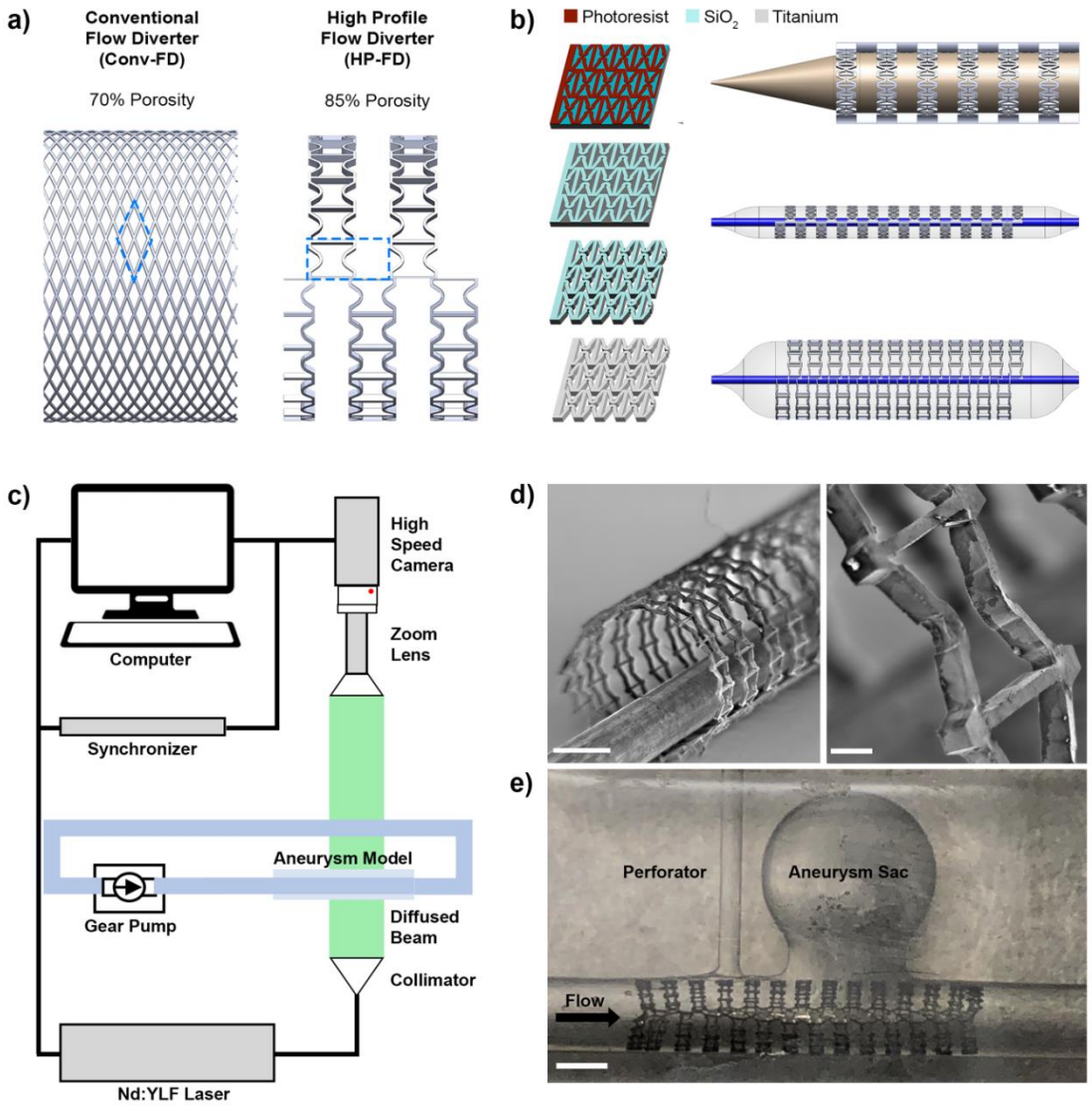

Figure 5-2: HP-FD Design and Fabrication. (a) Side-by-side comparison of HP-FD and Conv-FD designs. (b) Process flow diagram outlining fabrication and deployment technique for HP-FD. (c) Diagram of the PIV setup. (d) Scanning Electron Micrographs of deployed FD and unit cell (the scale bars are representative of 1 mm and 200 µm, respectively). (e) Deployed HP-FD in custom-fabricated silicone vascular phantom (the scale bar is representative of 1 mm.)

Here, we fabricated devices with struts 30 μm wide x 80 μm tall, resulting in an aspect ratio twice that of a Conv-FD, via Ti DRIE (Titanium Deep Reactive Ion Etching). This fabrication process allows an order of magnitude increase in machining resolution from the current state-of-the-art techniques for subtractive manufacturing of intravascular devices (e.g., laser-cutting with a minimum spot size of 25 μm). As a result, batch-scale fabrication of high-profile FDs (HP-FDs) with micron-scale resolution was achieved and, consequently, the first balloon-deployable FD produced via subtractive machining.

The inherent nature of the adopted fabrication processes is that the in-plane removal of material produces a flat pattern in which two side beams are connected by a series of cross beams (Fig. 5-1b). For deployment, a balloon catheter is interleaved between these cross beams, and the device is expanded by inflating the balloon (Mohammadi et al., 2013). Details regarding the mechanical characterization of the plasticity-based deployment of coronary stents fabricated in a similar manner have been previously reported by our group, observing that even in the regions of highest strain, no signs of fracture were present (Gott et al., 2012).

5.3.2. Benchmarking Against Conventional FD's

We deployed HP- and Conv-FDs in *in vitro* silicone models to benchmark the efficacy of our high-profile strut design on flow diversion against the current gold standard. Our models were designed and built in-house with an idealized wide-necked saccular sidewall aneurysm geometry with a perforating artery in close proximity (Fig. 5-1e) (Peck et al., 2018). Lab experiments were performed in flow conditions chosen to mimic that of the basilar artery, a region for which Conv-FDs usually have severe complications arising from perforator occlusion. Using two-dimensional Particle Image Velocimetry (PIV), we

measured the velocity of the flow in the aneurysm sac and in the perforating artery at the symmetry plane of the model before and after device implantation. We also performed Computational fluid dynamics (CFD) simulations generated from the silicone model Computer aided design (CAD) files. Baseline tests showed good agreement with PIV data at the midplane (Figure 5-2), and further evaluations were done to assess whether the greater heterogeneity of the HP-FD architecture contributes to adverse flow conditions due to out-of-plane motion.

Without any device implanted, it was observed that flow from the parent artery impinges on the distal wall of the aneurysm neck and that IA flow is shear-driven with high vorticity. The most immediate goal of FD therapy is to disrupt transmission of shear into the aneurysm sac, and it can be observed that the implantation of either device reduces the IA velocity by roughly an order of magnitude.

Implantation of the HP-FD realigns the IA flow from a regime of high counter-rotational flow to a proximal-to-distal direction, as the FD struts reduce the area available for shear transmission and the flow regime at the neck is instead dominated by a radial pressure differential into and out of the aneurysm sac (Fig 5-2b). This phenomenon is also observed in the Conv-FDs and suggests that porosity alone may not be an effective predictor of flow diversion efficacy, since the HP-FD (with 10-15% greater porosity than the Conv-FD) induces similar structural changes in the flow field while reducing the flow speed by roughly the same amount (P. Bouillot et al., 2014, 2015; Seshadhri et al., 2011; Stancampiano et al., 1997).

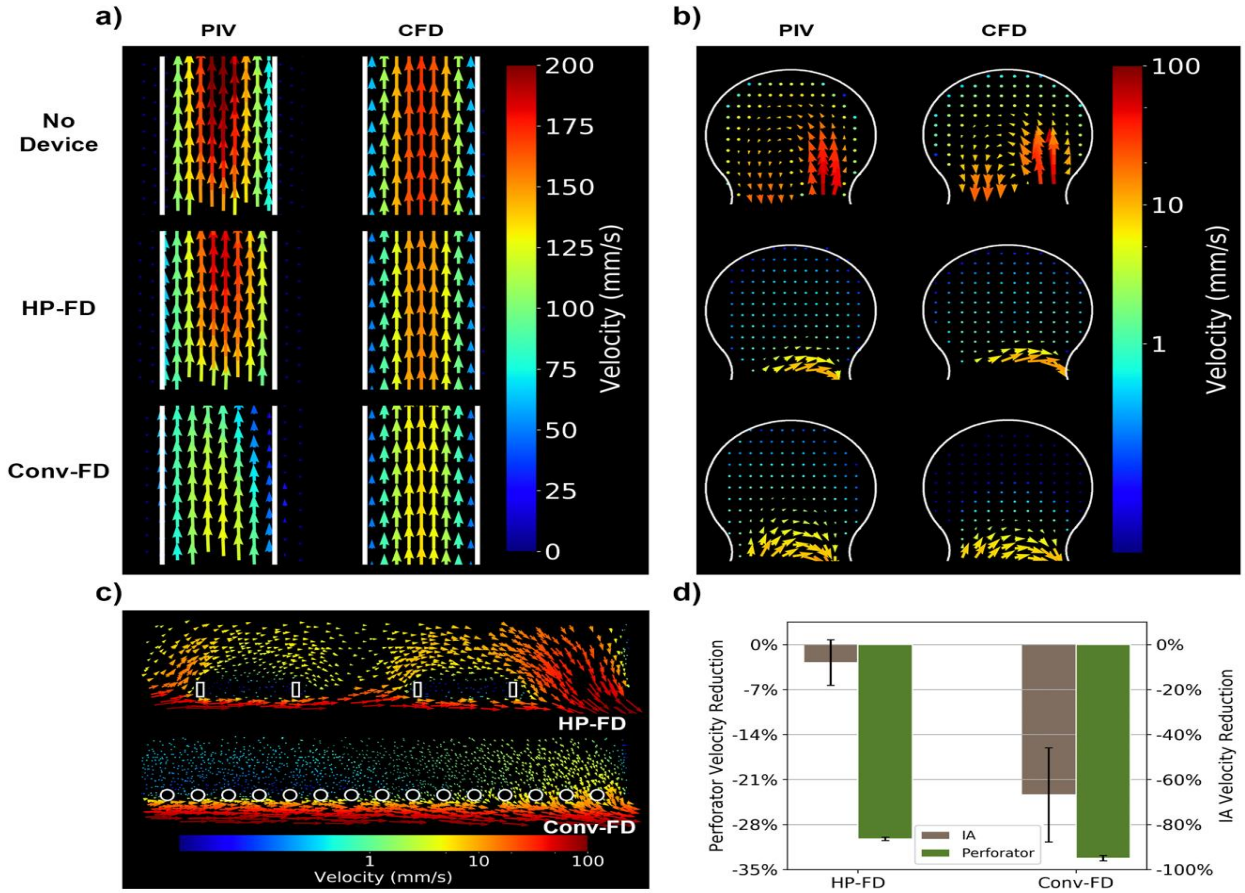

Figure 5-3: In-Vitro Comparison of HP-FD and Conv-FD Performance done to gain insight into parameters captured only in CFD. (a) PIV and CFD results for perforator velocity with and without devices in worst-case deployment position. (b) PIV and CFD results for intra-aneurysmal velocity with and without devices in worst-case deployment position. (c) Near-strut velocity field for HP-FD and Conv-FD. (d) Average intra-aneurysmal flow reduction across all deployment cases for

Most significantly, while the HP-FD appears to produce comparable IA flow reduction to the Conv-FD (87% vs. 95%), it negligibly affects perforator flow, unlike the Conv-FD (2% vs. 23%). Furthermore, when grouping data across all placements, we observed a fourfold decrease in the variance of perforator flow diversion with the HP-FD implanted relative to the Conv-FD case. This demonstrates the benefit of a high-profile, solid-construct design in which an increased porosity is largely unaffected by deployment technique and consequently, pressure-driven flow into perforating arteries is largely maintained. Clinically this establishes a new path forward by which flow diversion therapy can be extended into the posterior regions of the neurovasculature; which are often more perforator-rich and characterized by lower volumetric flow rates.

5.3.3. Device Characterization

Disruption of IA flow induces healing mechanisms on varying timescales. First, the reduction in flow velocity decreases the stress on the already weakened tissue of the aneurysm sac. Secondly, the stagnated flow prompts thrombogenic cues. This effectively forms a feedback loop, whereby a growing thrombus assists the FD in continuing to reduce flow into the aneurysm sac (Fiorella et al., 2009). Shear stresses (both within the blood and at the vessel wall) play an integral role in the signaling cues involved in this phenomenon.

Using PIV and CFD, we examined how design differences influence velocity and shear stress fields and considered the clinical and biological implications for behaviors associated with the presence of shear stress. Our CFD simulations showed that the HP-FD results in much steeper near-strut velocity gradients relative to Conv-FDs and creates larger, stronger, and more frequent saccular in-jets into the aneurysm (Fig. 5-2c). Although the Conv-FD results in a greater IA flow reduction at the neck, flow velocity was observed

to decay at a rate of X in HP-FD implanted cases. Hence, observed differences in IA flow reduction are localized to the vicinity of the device and away from the aneurysm wall.

It was also observed that the implantation of either device significantly reduces the average saccular WSS. However, both device groups show elevated local maximum WSS values at the distal segment of the aneurysm neck, where slower IA flow merges with the higher velocity flow coming in from the parent artery (Fig. 5-3). This effect is most pronounced for the HP-FD, which has high saccular velocities and the strut trailing edge low-pressure region accelerates the fluid back into the parent artery. While the Conv-FD also exhibits this behavior, both the region of increased shear and the magnitude of maximum WSS are smaller than in the HP-FD case. The implications of this are unclear given the dearth of a prognostic parameter threshold for efficacy and aneurysm occlusion, however previous studies on endothelial cell behavior may provide context.

Both the magnitude and the direction of applied shear stresses are known to affect endothelial cell behavior, with the expression of atheroprotective factors observed in laminar flows at moderately elevated shear stresses with a consistent applied direction (Chien, 2007). In contrast, turbulent or low magnitude reversing flows have been shown to induce the endothelial expression of inflammatory cytokines (Ando & Yamamoto, 2009). While extrapolating these results to tissues within a lesion where phenotype may vary by location is not trivial, this suggests that the appearance of elevated shear along the distal neck segment after device implantation is less harmful than the occurrence of stresses of the same magnitude due to recirculation (as in the unstented case).

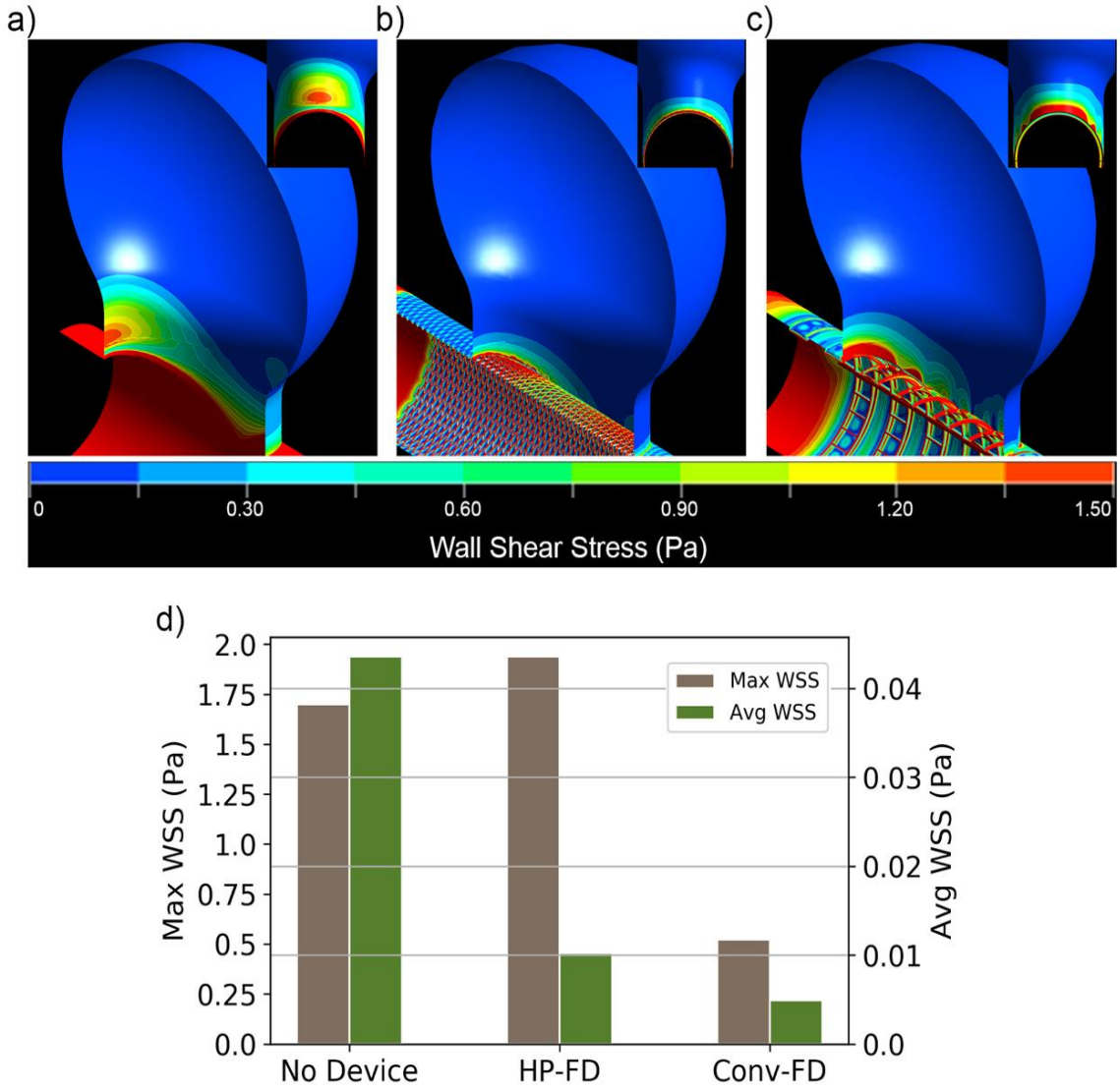

Figure 5-4: 3-D Plots of IA WSS from a clipped iso-plane with: (a) No device, (b) Conv-FD, and (c) HP-FD. Inset shows the YZ-orientation of the aneurysm distal side. (d) Maximum and average WSS for cases in panels (a), (b), and (c). Both devices significantly reduce average aneurysmal WSS and shift maximum values from a normal impulse/hammer force when not stented to a tangential viscosity driven one.

The presence of a region of elevated distal-segment WSS in the Conv-FD case agrees with this hypothesis, although the degree to which increased magnitude is tolerated is not well understood. Furthermore, both devices result in significant flow stagnation in the dome albeit via different mechanisms, i.e. even though both devices induce realignment, the magnitude of the velocity in the vicinity of the struts differs as well as the uniformity of the velocity field passing through the device into the aneurysm zone (Fig. 5-4c).

This was also observed as elevated shear flow for the HP-FD case (Fig 5-4). While fluid shear in the Conv-FD case is due to one main in-jet at the proximal aneurysm wall and fluid exiting close to the distal wall, the HP-FD case exhibits many more areas of elevated fluid shear due to significant inflow around the struts. Several thrombogenic cues have been linked to elevated shear stresses within the blood (e.g., platelet activation) ,so we hypothesize that high-aspect ratio struts can potentially accelerate thrombogenesis (Alevriadou et al., 1993). In any case, the influence on the IA flow highlights the potential for HP-FD to induce comparable flow diversion than Conv-FDs at higher porosities.

Finally, the HP-FD introduces a design regime not before implemented in the context of flow diversion. Flow reductions in this case are largely due to a mixture of increased shear rate from high porosity, lower pore density, and the increased hydrodynamic resistance that is induced by the presence of less-streamlined, high-aspect ratio structures. Exactly how these factors interact, or if there are additional factors to consider, still warrants investigation. We suspect the aspect ratio of the struts may enhance flow diversion selectivity as this is essentially also the ratio of effective areas encountered

normal to the direction of flows in bifurcating vessels (i.e. frontal areas inducing form drag). This level of control is especially compelling for a region such as the basilar trunk, where pontine arteries generally branch at right angles, maximizing the difference between these frontal areas. For many other regions of the neurovasculature, the angle between the parent and perforating artery is more obtuse and this effect may not be as prominent. Nevertheless, aspect ratio manipulation via Ti DRIE may offer a mechanism for optimization in these anatomies as well.

5.4. Discussion

The design concept presented in our study uniquely demonstrates the feasibility to divert flow selectively via a high porosity device with an unprecedented degree of machining resolution. Clinically, the ability to manipulate the permeability of the HP-FD selectively provides better control over flow diversion than standard devices. This is particularly advantageous in cases in which it is desired to redirect flow away from certain structures without affecting nearby elements (e.g., shear-driven flow near jailed perforators).

The device presented in this study exhibits an intermediate porosity compared to traditional and flow diverting stents. In previous PIV studies with commercially-available devices the transient anterior circulation, traditional neurovascular stents within this porosity range (85% - 90%) had shown behavior associated with FDs (i.e. flow realignment) at lower diastolic flow rates, before reverting to exhibit more traditional stent hemodynamics (i.e. shear-driven IA flow) at peak systole. As a result, this range of stent porosities was characterized as one of “hemodynamic transition”. This suggests that the amount of metal coverage required to induce flow diversion may be less than current embodiments of FDs and hints at the suitability of more porous designs for the posterior

circulation. While there is a precedent for the use of high-porosity stents in treating posterior circulation aneurysms, reports have been sparse and the results have been mixed (Kaku et al., 2003; Zenteno et al., 2008). High-aspect ratio strut design may further augment the flow diversion effect at intermediate-to-high porosities in order to broaden this region of hemodynamic transition while preserving selectivity. The degree to which AR can modulate the effect of increased porosity on the flow diversion effect deserves further study.

There has long been interest in characterizing the hydraulic permeability of synthetic structures as a function of unit cell geometries for various applications (e.g. filtration design). Analyses proceeding from geometric assumptions of isotropic unit cells containing cylindrical crossing fibers have concluded that the permeability constant in Darcy flow scales proportionally to the square of fiber spacing (i.e. pore size) (Clague et al., 2000; Sobera & Kleijn, 2006), where:

$$< v > = -\frac{\boldsymbol{\kappa}}{\mu} \cdot \nabla P \qquad \text{Eq. 5-5}$$

$$< v > = \boldsymbol{\kappa} \alpha \delta^2 \qquad \text{Eq. 5-6}$$

and <v> is the superficial (averaged) velocity, $\boldsymbol{\kappa}$ is the permeability tensor, μ is the dynamic viscosity, ∇P is the average pressure gradient across the porous medium and ∂ is the pore size.

Bouillot et al. 2015 have taken this a step further, applying these porous media concepts specifically to intracranial flow diversion and finding that experimental IA velocity reductions correlate fairly well with FD permeability when using this definition (Bouillot et al., 2014). This corroboration may be because all devices included in the study contained struts whose aspect ratio $\cong 1$ and therefore maintained the underlying assumption of isotropy in the permeability tensor. The selectivity we have observed as a result of increased strut profile on IA flow properties may be considered macroscopically as a change to the thickness of the porous medium, but may also potentially be modelled on a more local scale as anisotropy in the permeability tensor.

These results indicate that although porosity affects flow diversion most strongly, additional mechanisms remain that can alter the response of a given device. Ti DRIE offers a unique approach to anisotropically modify device permeability as it allows for independent manipulation of the factors affecting unit-cell strut geometries. Going forward, we will explore designs allowing for independent variation of in-plane and out-of-plane strut features (e.g. pore width/length, strut thickness, respectively) while maintaining a constant, top-down projection of porosity. While the percentage of metal coverage relative to tissue area may be an adequate predictor of flow diversion success for more homogenous and symmetric designs, we anticipate this value may offer an incomplete description of flow diversion in heterogeneous designs within a certain length-scale. Future studies leveraging this fabrication technique may be able to more rigorously examine the influence of FD geometry on the relationship between fluidic resistance and shear reduction. A better understanding of this interaction may eventually serve as a

mechanism to fine-tune flow diversion for more challenging physiological conditions (e.g., delicate posterior segment aneurysms, aneurysms arising near small perforators, etc.).

6. CONCLUSIONS

Herein we have introduced a new design parameter previously not considered within the context of aneurysmal flow diversion design and implementation, namely that of Strut Height (SH). Current clinically available devices rely on device porosity and pore density as the sole determining factor for device performance in the clinic. Devices rely on various small extruded wire (μm diameter) braiding techniques and designs to achieve intra-aneurysmal reductions, and subsequent potential for occlusion and absorption. The techniques currently used to create devices of sufficiently small scales require isometric designs and thereby have no consideration of this radial design parameter.

Here we have shown that devices of this scale can be created and tested in the lab, that consideration of SH has important implications for flow diversion and subsequently outcomes in the clinic, and that this parameter is a potentially important one in advancing our understanding of IA flow diversion.

Members of this laboratory developed a deep reactive ion etched (DRIE), titanium, balloon-deployable, single-piece constructed, flow diversion device. They have shown that by utilizing an auxetic unit cell design, this device can accommodate large radial strains without fracturing; a key prerequisite for endovascular navigation and compatibility with balloon deployment. Consequently, these designs exhibit minimal foreshortening and enhanced reliability in wall apposition.

Etching a titanium solid device in this manner also allowed the production of an anisotropic strut design of non-circular cross section and higher porosity, which were tested against current generation design parameters for efficacy. Experimental and computational results showed that higher strut aspect ratios allowed for higher device porosity to achieve

similar aneurysmal reductions and reduced device response to, or sensitivity to, potential changes in porosity.

These results indicate that the current state of the art of flow diversion, namely that of reducing shear transmission into the aneurysm and high velocity impingement on aneurysm lumen, are not the only mechanisms worth considering for flow diversion. This new generation of devices may be made more porous reducing risk associated with branch occlusion and edema, and much more resilient. Devices created and tested here showed resistance to mechanical disturbances as well as morphological and technique driven variability which affect outcomes and device reliability in the clinic. So too do these results hint at potential for their use in homing in the specific post flow diversion aneurysmal flow regimes and parameters which are most associated with thrombosis, reendothelialization, and absorption. Controlling the fluidic response both through a device whose values vary less in the clinic, and a device which can predict the velocities post implementation would revolutionize flow diversion and aneurysm treatment.

6.1. Future Work

Current work shows the capability of a Ti DRIE solid construct device of low metal coverage and high aspect ratio struts to achieve aneurysm velocity reductions relative to currently clinically available devices. Future work will need to optimize design parameters of porosity, pore density and strut height with respect to IA velocity. Results indicated that high aspect ratio devices saw a shift in distal wall response to implementation from other devices due to higher velocity outlet. Exactly how the lumen would respond to a more aggressive distal velocity profile when treated with a high aspect ratio device remains to be seen and will need to be tested. Reendothelialization in the presence of high aspect ratio

struts and thrombogenesis in the presence of more complicated flow profile represent further important biological work to be done to fully understand how SH can be leveraged to improve flow diversion and usher in a new generation of design and performance.

7. BIBLIOGRAPHY

Adix, M. L., Kaminsky, I. A., & Choi, I. S. (2017). Ophthalmic artery occlusion after Pipeline Embolization Device placement with reconstitution of flow via an endoleak: a report of two cases. *J NeuroIntervent Surg*, *9*(7), 686–688. https://doi.org/10.1136/neurintsurg-2016-012782

Aenis, M., Stancampiano, A. P., Wakhloo, A. K., & Lieber, B. B. (1997). Modeling of Flow in a Straight Stented and Nonstented Side Wall Aneurysm Model. *Journal of Biomechanical Engineering*, *119*(2), 206–212. https://doi.org/10.1115/1.2796081

Aimi, M. F., Rao, M. P., MacDonald, N. C., Zuruzi, A. S., & Bothman, D. P. (2004). High-aspect-ratio bulk micromachining of titanium. *Nature Materials*, *3*(2), 103–105. https://doi.org/10.1038/nmat1058

Alevriadou, B. R., Moake, J. L., Turner, N. A., Ruggeri, Z. M., Folie, B. J., Phillips, M. D., Schreiber, A. B., Hrinda, M. E., & McIntire, L. V. (1993). Real-time analysis of shear-dependent thrombus formation and its blockade by inhibitors of von Willebrand factor binding to platelets. *Blood*, *81*(5), 1263–1276.

Amir Paisal, M. S., Taib, I., & Ismail, A. E. (2017). Computational Analysis on Stent Geometries in Carotid Artery: A Review. *IOP Conference Series: Materials Science and Engineering*, *166*(1), 0–13. https://doi.org/10.1088/1757-899X/165/1/012003

Ando, J., & Yamamoto, K. (2009). Vascular Mechanobiology. *Circulation Journal*, *73*(11), 1983–1992. https://doi.org/10.1253/circj.CJ-09-0583

ANSYS® Academic Research Mechanical. (2013). ANSYS Fluent Theory Guide. *ANSYS Inc., USA*, *15317*(November), 1–759. http://www.pmt.usp.br/ACADEMIC/martoran/NotasModelosGrad/ANSYS Fluent Theory Guide 15.pdf

Anzai, H., Yoshida, Y., Sugiyama, S., Endo, H., Matsumoto, Y., & Ohta, M. (2015). Porosity dependency of an optimized stent design for an intracranial aneurysm. *Technology and Health Care*, *23*(5), 547–556. https://doi.org/10.3233/THC-151007

Augsburger, L., Farhat, M., Reymond, P., Fonck, E., Kulcsar, Z., Stergiopulos, N., & Rüfenacht, D. A. (2009). Effect of flow diverter porosity on intraaneurysmal blood flow. *Clinical Neuroradiology*, *19*(3), 204–214. https://doi.org/10.1007/s00062-009-9005-0

Backes, D., Vergouwen, M. D. I., Velthuis, B. K., Van Der Schaaf, I. C., Bor, A. S. E., Algra, A., & Rinkel, G. J. E. (2014). Difference in aneurysm characteristics between ruptured and unruptured aneurysms in patients with multiple intracranial aneurysms. *Stroke*, *45*(5), 1299–1303. https://doi.org/10.1161/STROKEAHA.113.004421

Barnes, H. A., Townsend, P., & Walters, K. (1971). On pulsatile flow of non-Newtonian liquids. *Rheologica Acta*, *10*(4), 517–527. https://doi.org/10.1007/BF03396402

Bartleson, J. D., Trautmann, J. C., & Sundt, T. M. (1986). Minimal Oculomotor Nerve Paresis Secondary to Unruptured Intracranial Aneurysm. *Archives of Neurology*, *43*(10), 1015–1020. https://doi.org/10.1001/archneur.1986.00520100033011

Benjamin, E. J., Muntner, P., Alonso, A., Bittencourt, M. S., Callaway, C. W., Carson, A. P., Chamberlain, A. M., Chang, A. R., Cheng, S., Das, S. R., Delling, F. N., Djousse, L., Elkind, M. S. V., Ferguson, J. F., Fornage, M., Jordan, L. C., Khan, S. S., Kissela, B. M., Knutson, K. L., … Virani, S. S. (2019). Heart Disease and Stroke Statistics-2019 Update: A Report From the American Heart Association. In *Circulation* (Vol. 139, Issue 10). https://doi.org/10.1161/CIR.0000000000000659

Bhogal, P., Ganslandt, O., Bäzner, H., Henkes, H., & Pérez, M. A. (2017). The Fate of Side Branches Covered by Flow Diverters–Results from 140 Patients. *World Neurosurgery*, *103*, 789–798. https://doi.org/10.1016/j.wneu.2017.04.092

Bing, F., Darsaut, T. E., Salazkin, I., Makoyeva, A., Gevry, G., & Raymond, J. (2013). Stents and flow diverters in the treatment of aneurysms: device deformation in vivo may alter porosity and impact efficacy. *Neuroradiology*, *55*(1), 85–92. https://doi.org/10.1007/s00234-012-1082-0

Bishop, C. C. R., Powell, S., Rutt, D., & Browse, N. L. (1986). Transcranial doppler measurement of middle cerebral artery blood flow velocity: A validation study. *Stroke*, *17*(5), 913–915. https://doi.org/10.1161/01.STR.17.5.913

Bogren, H. G., Buonocore, M. H., & Gu, W. (1994). Carotid and vertebral artery blood flow in left- and right-handed healthy subjects measured with MR velocity mapping. *Journal of Magnetic Resonance Imaging*, *4*(1), 37–42.

Bouillot, P., Brina, O., Ouared, R., Yilmaz, H., Lovblad, K.-O., Farhat, M., & Mendes Pereira, V. (2016). Computational fluid dynamics with stents: quantitative comparison with particle image velocimetry for three commercial off the shelf intracranial stents. *J NeuroIntervent Surg*, *8*, 309–315. https://doi.org/10.1136/neurintsurg-2014-011468

Bouillot, Pierre, Brina, O., Ouared, R., Lovblad, K. O., Farhat, M., & Mendes Pereira, V. (2015). Hemodynamic transition driven by stent porosity in sidewall aneurysms. *Journal of Biomechanics*, *48*(7), 1300–1309. https://doi.org/10.1016/j.jbiomech.2015.02.020

Bouillot, Pierre, Brina, O., Ouared, R., Lovblad, K. O., Farhat, M., & Pereira, V. M. (2014). Particle imaging velocimetry evaluation of intracranial stents in sidewall aneurysm: Hemodynamic transition related to the stent design. *PLoS ONE*, *9*(12), 1–17. https://doi.org/10.1371/journal.pone.0113762

Bouthillier, A., Van Loveren, H. R., & Keller, J. T. (1996). Segments of the internal carotid artery: A new classification. *Neurosurgery*, *38*(3), 425–433. https://doi.org/10.1097/00006123-199603000-00001

Brinjikji, W., Murad, M. H., & Lanzino, G. (2013). Endovascular Treatment of Intracranial Aneurysms With Flow Diverters. *Stroke*, *44*(2), 442–447. https://doi.org/10.1161/STROKEAHA.112.678151

Brisman JL, Song JK, Newell DW. (2006). Cerebral aneurysms. *N Engl J Med*, *355*,

928–939.

Buijs, P. C., Krabbe-Hartkamp, M. J., Bakker, C. . J., de Lange, E. E., Ramos, L. M., Breteler, M. M., & Mali, W. P. (1998). Effect of age on cerebral blood flow: measurement with ungated two-dimensional phase-contrast MR angiography in 250 adults. *Radiology*, *209*(3), 667–674. https://doi.org/10.1148/radiology.209.3.9844657

Byrne, J. V., Beltechi, R., Yarnold, J. A., Birks, J., & Kamran, M. (2010). Early experience in the treatment of intra-cranial aneurysms by endovascular flow diversion: A multicentre prospective study. *PLoS ONE*, *5*(9), 1–8. https://doi.org/10.1371/journal.pone.0012492

Chien, S. (2007). Mechanotransduction and endothelial cell homeostasis: The wisdom of the cell. *American Journal of Physiology - Heart and Circulatory Physiology*, *292*(3), 1209–1224. https://doi.org/10.1152/ajpheart.01047.2006

Cho, Y. I., & Kensey, K. R. (1991). Effects of the non-Newtonian viscosity of blood on flows in a diseased arterial vessel. Part 1: Steady flows. *Biorheology*, *28*(3/4), 241–262. https://doi.org/10.3233/BIR-1991-283-415

Clague, D. S., Kandhai, B. D., Zhang, R., & Sloot, P. M. . (2000). Hydraulic permeability of (un)bounded fibrous media using the lattice boltzmann method. *Physical Review E*, *61*(1), 616–625. https://doi.org/10.1103/physreve.61.616

Damiano, R. J., Tutino, V. M., Paliwal, N., Ma, D., Davies, J. M., Siddiqui, A. H., & Meng, H. (2017). Compacting a single flow diverter versus overlapping flow diverters for intracranial aneurysms: A computational study. *American Journal of Neuroradiology*, *38*(3), 603–610. https://doi.org/10.3174/ajnr.A5062

Dandy, W. E. (1938). Intracranial Aneurysm of the Internal Carotid Artery. *Annals of Surgery*, *107*(5), 654–659. http://www.pubmedcentral.nih.gov/articlerender.fcgi?artid=1386933&tool=pmcentrez&rendertype=abstract

Dong, J., Wong, K. K. L., Sun, Z., & Tu, J. (2011). Numerical Analysis of Stent Porosity and Strut Geometry for Intra-saccular Aneurysmal Flow. *Computing in Cardiology*, *38*, 477–480.

Duraiswamy, N., Schoephoerster, R. T., Moreno, M. R., & Moore, J. E. (2007). Stented Artery Flow Patterns and Their Effects on the Artery Wall. *Annual Review of Fluid Mechanics*, *39*(1), 357–382. https://doi.org/10.1146/annurev.fluid.39.050905.110300

Durso, P. I., Lanzino, G., Cloft, H. J., & Kallmes, D. F. (2011). Flow diversion for intracranial aneurysms: A review. *Stroke*, *42*(8), 2363–2368. https://doi.org/10.1161/STROKEAHA.111.620328

Eymard, R., Gallouët, T., & Herbin, R. (2019). Finite Volume Methods. In *Handbook of Numerical Analysis* (1st ed., Vol. 7, pp. 713–1020). Elsevier.

Fiorella, D., Lylyk, P., Szikora, I., Kelly, M. E., Albuquerque, F. C., McDougall, C. G., & Nelson, P. K. (2009). Curative cerebrovascular reconstruction with the Pipeline embolization device: the emergence of definitive endovascular therapy for intracranial aneurysms. *J NeuroIntervent Surg*, *1*(1), 56–65. https://doi.org/10.1136/jnis.2009.000083

Forget, T., Veznedaroglu, E., Sharan, A., Mitchell, W., Silva, M., & Rosenwasser, R. H. (2001). A Review of Size and Location of Ruptured Intracranial Aneurysms. *Neurosurgery*, *49*(6), 1322–1326.

Frosen, J., Tulamo, R., Paetau, A., Laaksamo, E., Korja, M., Laakso, A., Niemela, M., & Hernesniemi, J. (2012). Saccular intracranial aneurysm: pathology and mechanisms. *Acta Neuropathologica*, *123*(1), 773–786. https://doi.org/10.1007/s00401-011-0939-3

Galbraith, C. G., Skalak, R., & Chien, S. (1998). Shear stress induces spatial reorganization of the endothelial cell cytoskeleton. *Cell Motility and the Cytoskeleton*, *40*(4), 317–330.

Gott, S. C., Jabola, B. A., Xu, G., & Rao, M. P. (2012). Vascular stents with rationally-designed surface patterning. *Conference Proceedings : ... Annual International Conference of the IEEE Engineering in Medicine and Biology Society. IEEE Engineering in Medicine and Biology Society. Conference*, *2012*, 1639–1642. https://doi.org/10.1109/EMBC.2012.6346260

Guglielmi, G., Vinuela, F., Dion, J., & Duckwiler, G. (1991). Electrothrombosis of Saccular Aneurysms via Endovasuclar Approach: Part 2. *Journal of Neurosurgery*, *75*, 8–14.

Guglielmi, G., Vinuela, F., Sepetka, I., & Macellari, V. (1991). Electrothrombosis of Saccular Aneurysms via Endovasuclar Approach: Part 1. *Journal of Neurosurgery*, *75*, 1–7.

Hodis, S., Ding, Y., Dai, D., Lingineni, R., Mut, F., Kallmes, D., & Kadirvel, R. (2016). Relationship between aneurysm occlusion and flow diverting device oversizing in a rabbit model. *J NeuroIntervent Surg*, *8*(1), 94–98. https://doi.org/10.1136/neurintsurg-2014-011487.Relationship

Hoi, Y., Meng, H., Woodward, S. H., Bendok, B. R., Hanel, R. A., Guterman, L. R., & Hopkins, L. N. (2004). Effects of arterial geometry on aneurysm growth: Three-dimensional computational fluid dynamics study. *Journal of Neurosurgery*, *101*(4), 676–681. https://doi.org/10.3171/jns.2004.101.4.0676

Howe, C., Mishra, S., Kim, Y.-S., Chen, Y., Ye, S.-H., Wagner, W. R., Jeong, J.-W., Byun, H.-S., Kim, J.-H., Chun, Y., & Yeo, W.-H. (2018). Stretchable, Implantable, Nanostructured Flow-Diverter System for Quantification of Intra-aneurysmal Hemodynamics. *ACS Nano*, acsnano.8b04689. https://doi.org/10.1021/acsnano.8b04689

Janiga, G., Daróczy, L., Berg, P., Thévenin, D., Skalej, M., & Beuing, O. (2015). An automatic CFD-based flow diverter optimization principle for patient-specific intracranial aneurysms. *Journal of Biomechanics*, *48*(14), 3846–3852. https://doi.org/10.1016/j.jbiomech.2015.09.039

Jeong, Y. G., Jung, Y. T., Kim, M. S., Eun, C. K., & Jang, S. H. (2009). Size and location of ruptured intracranial aneurysms. *Journal of Korean Neurosurgical Society*, *45*(1), 11–15. https://doi.org/10.3340/jkns.2009.45.1.11

Jiménez, J. M., & Davies, P. F. (2009). Hemodynamically driven stent strut design. *Annals of Biomedical Engineering*, *37*(8), 1483–1494. https://doi.org/10.1007/s10439-009-9719-9

Kaku, Y., Yoshimura, S., Yamakawa, H., & Sakai, N. (2003). Failure of stent-assisted endovascular treatment for ruptured dissecting aneurysms of the basilar artery. *Neuroradiology*, *45*(1), 22–26. https://doi.org/10.1007/s00234-002-0903-y

Kayembe, K. N., Sasahara, M., & Hazama, F. (1984). Cerebral aneurysms and variations in the circle of Willis. *Stroke*, *15*(5), 846–850. https://doi.org/10.1161/01.STR.15.5.846

Keedy, A. (2006). An overview of intracranial aneurysms. *McGill Journal of Medicine*, *9*(2), 141–146.

Kenner, T., Leopold, H., & Hinghofer-Szalkay, H. (1977). The continuous high-precision measurement of the density of flowing blood. *Pflügers Archiv European Journal of Physiology*, *370*(1), 25–29. https://doi.org/10.1007/BF00707941

Kim, M., Taulbee, D. B., Tremmel, M., & Meng, H. (2008). Comparison of two stents in modifying cerebral aneurysm hemodynamics. *Annals of Biomedical Engineering*, *36*(5), 726–741. https://doi.org/10.1007/s10439-008-9449-4

Kim, Y. H., Xu, X., & Lee, J. S. (2010). The effect of stent porosity and strut shape on saccular aneurysm and its numerical analysis with lattice Boltzmann method. *Annals of Biomedical Engineering*, *38*(7), 2274–2292. https://doi.org/10.1007/s10439-010-9994-5

Kliś, K., Krzyżewski, R., Kwinta, B., Stachura, K., & Gąsowski, J. (2019). Tortuosity of the Internal Carotid Artery and Its Clinical Significance in the Development of Aneurysms. *Journal of Clinical Medicine*, *8*(2), 237. https://doi.org/10.3390/jcm8020237

Kotowski, M., Naggara, O., Darsaut, T. E., Nolet, S., Gevry, G., Kouznetsov, E., & Raymond, J. (2013). Safety and occlusion rates of surgical treatment of unruptured intracranial aneurysms: a systematic review and meta-analysis of the literature from 1990 to 2011. *Journal of Neurology, Neurosurgery & Psychiatry*, *84*(1), 42–48. https://doi.org/10.1136/jnnp-2011-302068

Kulcsár, Z., Augsburger, L., Reymond, P., Pereira, V. M., Hirsch, S., Mallik, A. S., Millar, J., Wetzel, S. G., Wanke, I., & Rüfenacht, D. A. (2012). Flow diversion

treatment: Intra-aneurismal blood flow velocity and WSS reduction are parameters to predict aneurysm thrombosis. *Acta Neurochirurgica*, *154*(10), 1827–1834. https://doi.org/10.1007/s00701-012-1482-2

Kulcsár, Z., Wetzel, S. G., Augsburger, L., Gruber, A., Wanke, I., & Andre Rüfenacht, D. (2010). Effect of flow diversion treatment on very small ruptured aneurysms. *Neurosurgery*, *67*(3), 789–793. https://doi.org/10.1227/01.NEU.0000372920.39101.55

LaBarabera, M. (1990). Principles of design of fluid transport systems in zoology. *Science*, *249*(4972), 992–1000.

LaDisa, J. F., Olson, L. E., Guler, I., Hettrick, D. a, Audi, S. H., Kersten, J. R., Warltier, D. C., & Pagel, P. S. (2004). Stent design properties and deployment ratio influence indexes of wall shear stress: a three-dimensional computational fluid dynamics investigation within a normal artery. *Journal of Applied Physiology (Bethesda, Md. : 1985)*, *97*(1), 424–430; discussion 416. https://doi.org/10.1152/japplphysiol.01329.2003

Lall, R. R., Crobeddu, E., Lanzino, G., Cloft, H. J., & Kallmes, D. F. (2014). Acute branch occlusion after Pipeline embolization of intracranial aneurysms. *Journal of Clinical Neuroscience : Official Journal of the Neurosurgical Society of Australasia*, *21*(4), 668–672. https://doi.org/10.1016/j.jocn.2013.07.011

Lauric, A., Hippelheuser, J., Safain, M. G., & Malek, A. M. (2014). Curvature effect on hemodynamic conditions at the inner bend of the carotid siphon and its relation to aneurysm formation. *Journal of Biomechanics*, *47*(12), 3018–3027. https://doi.org/10.1016/j.jbiomech.2014.06.042

Li, H., Pan, R., Wang, H., Rong, X., Yin, Z., Milgrom, D. P., Shi, X., Tang, Y., & Peng, Y. (2013). Clipping versus coiling for ruptured intracranial aneurysms: A systematic review and meta-analysis. *Stroke*, *44*(1), 29–37. https://doi.org/10.1161/STROKEAHA.112.663559

Lieber, B. B., Stancampiano, A. P., & Wakhloo, A. K. (1997). Alteration of Hemodynamics in Aneurysm Models by Stenting: Influence of Stent Porosity. *Annals of Biomedical Engineering*, *25*, 460–469. https://doi.org/10.1007/BF02684187

Lin, L. M., Colby, G. P., Jiang, B., Uwandu, C., Huang, J., Tamargo, R. J., & Coon, A. L. (2015). Classification of cavernous internal carotid artery tortuosity: A predictor of procedural complexity in Pipeline embolization. *Journal of NeuroInterventional Surgery*, *7*(9), 628–633. https://doi.org/10.1136/neurintsurg-2014-011298

Lindegaard, K. F., Lundar, T., Wiberg, J., Sjoberg, D., Aaslid, R., & Nornes, H. (1987). Variations in middle cerebral artery blood flow investigated with noninvasive transcranial blood velocity measurements. *Stroke*, *18*(6), 1025–1030. https://doi.org/10.1161/01.STR.18.6.1025

Luessenhop, A., & Velasquez, A. (1964). Observations on the Tolerance of the Intracranial Arteries to Catherterization. *Journal of Neurosurgery*, *21*.

M. Raffel, C. Willert, S. Werely, J. K. (2007). *Particle Image Velocimetry: a Practical Guide* (2nd ed.). Springer.

Matsuda, Y., Chung, J., Keigher, K., & Lopes, D. (2018). A comparison between the new Low-profile Visualized Intraluminal Support (LVIS Blue) stent and the Flow Redirection Endoluminal Device (FRED) in bench-top and cadaver studies. *Journal of NeuroInterventional Surgery*, *10*(3), 274–278. https://doi.org/10.1136/neurintsurg-2017-013074

Meinhart, C. D., Wereley, S. T., & Santiago, J. G. (2000). A PIV Algorithm for Estimating Time-Averaged Velocity Fields. *Journal of Fluids Engineering*, *122*(2), 285. https://doi.org/10.1115/1.483256

Meng, H., Wang, Z., Kim, M., Ecker, R. D., & Hopkins, L. N. (2006). Saccular aneurysms on straight and curved vessels are subject to different hemodynamics: implications of intravascular stenting. *American Journal of Neuroradiology*, *27*(9), 1861–1865. https://doi.org/10.3174/ajnr.a3234

Mohammadi, A. R., Mohamed Ali, M. S., Lappin, D., Schlosser, C., & Takahata, K. (2013). Inductive antenna stent: design, fabrication and characterization. *Journal of Micromechanics and Microengineering*, *23*(2), 025015. https://doi.org/10.1088/0960-1317/23/2/025015

Moon, J. Y., Suh, D. C., Lee, Y. S., Kim, Y. W., & Lee, J. S. (2014). *Considerations of Blood Properties , Outlet Boundary Conditions and Energy Loss Approaches in Computational Fluid Dynamics Modeling*. *9*(1), 1–8.

Mut, F., Raschi, M., Scrivano, E., Bleise, C., Chudyk, J., Ceratto, R., Lylyk, P., & Cebral, J. R. (2015). Association between hemodynamic conditions and occlusion times after fl ow diversion in cerebral aneurysms. *J NeuroIntervent Surg*, *7*(1), 286–290. https://doi.org/10.1136/neurintsurg-2013-011080

Nahed, B. V., Bydon, M., Ozturk, A. K., Bilguvar, K., Bayrakli, F., & Gunel, M. (2007). Genetics of intracranial aneurysms. *Neurosurgery*, *60*(2), 213–225. https://doi.org/10.1227/01.NEU.0000249270.18698.BB

Nelson, P. K., Lylyk, P., Szikora, I., Wetzel, S. G., Wanke, I., & Fiorella, D. (2011). The pipeline embolization device for the intracranial treatment of aneurysms trial. *American Journal of Neuroradiology*, *32*(1), 34–40. https://doi.org/10.3174/ajnr.A2421

Ohkuma, H., Fujita, S., & Suzuki, S. (2002). Incidence of aneurysmal subarachnoid hemorrhage in Shimokita, Japan, from 1989 to 1998. *Stroke*, *33*(1), 195–199. https://doi.org/10.1161/hs0102.101891

Ohta, M., Wetzel, S. G., Dantan, P., Bachelet, C., Lovblad, K. O., Yilmaz, H., Flaud, P., & Ru, D. A. (2005). Rheological Changes After Stenting of a Cerebral Aneurysm :

A Finite Element Modeling Approach. *Cardio Vascular and Interventional Radiology*, *28*(1), 768–772. https://doi.org/10.1007/s00270-004-7148-6

Orz, Y., Kobayashi, S., Osawa, M., & Tanaka, Y. (1997). Aneurysm size: A prognostic factor for rupture. *British Journal of Neurosurgery*, *11*(2), 144–149. https://doi.org/10.1080/02688699746500

Ouared, R., Larrabide, I., Brina, O., Bouillot, P., Erceg, G., Yilmaz, H., Lovblad, K. O., & Mendes Pereira, V. (2016). Computational fluid dynamics analysis of flow reduction induced by flow-diverting stents in intracranial aneurysms: A patient-unspecific hemodynamics change perspective. *Journal of NeuroInterventional Surgery*, *8*(12), 1288–1293. https://doi.org/10.1136/neurintsurg-2015-012154

Parker, E. R., Thibeault, B. J., Aimi, M. F., Rao, M. P., & MacDonald, N. C. (2005). Inductively Coupled Plasma Etching of Bulk Titanium for MEMS Applications. *Journal of The Electrochemical Society*, *152*(10), C675. https://doi.org/10.1149/1.2006647

Passerini, T., Sangalli, L. M., Vantini, S., Piccinelli, M., Bacigaluppi, S., Antiga, L., Boccardi, E., Secchi, P., & Veneziani, A. (2012). An Integrated Statistical Investigation of Internal Carotid Arteries of Patients Affected by Cerebral Aneurysms. *Cardiovascular Engineering and Technology*, *3*(1), 26–40. https://doi.org/10.1007/s13239-011-0079-x

Peck, R. A., Bahena, E., Jahan, R., Aguilar, G., Tsutsui, H., Princevac, M., Wilhelmus, M. M., & Rao, M. P. (2018). Meso-Scale Particle Image Velocimetry Studies of Neurovascular Flows In Vitro. *JoVE*, *142*, e58902. https://doi.org/doi:10.3791/58902

Perktold, K., Gruber, K., Kenner, T., & Florian, H. (1984). Calculation of pulsatile flow and particle paths in an aneurysm-model. *Basic Research in Cardiology*, *79*(3), 253–261. https://doi.org/10.1007/BF01908024

Peter W., R., Eleanor, L., Hamilton E, H., & William H., A. (1964). Viscosity of normal human blood under normothermic and hypothermic conditions. *J. Appl. Physiol.*, *19*(1), 117–122.

Phillips, T. J., Wenderoth, J. D., Phatouros, C. C., Rice, H., Singh, T. P., Devilliers, L., Wycoco, V., Meckel, S., & McAuliffe, W. (2012). Safety of the pipeline embolization device in treatment of posterior circulation aneurysms. *American Journal of Neuroradiology*, *33*(7), 1225–1231. https://doi.org/10.3174/ajnr.A3166

Pierot, L., Spelle, L., & Vitry, F. (2008). Immediate clinical outcome of patients harboring unruptured intracranial aneurysms treated by endovascular approach: Results of the ATENA study. *Stroke*, *39*(9), 2497–2504. https://doi.org/10.1161/STROKEAHA.107.512756

Pierot, L., & Wakhloo, A. K. (2013). Endovascular treatment of intracranial aneurysms: Current status. *Stroke*, *44*(7), 2046–2054.

https://doi.org/10.1161/STROKEAHA.113.000733

Portegies, M. L. P., Bruijn, R. F. A. ., Hofman, A., Doudstaal, P. J., & Ikram, A. (2014). Cerebral Vasomotor Reactivity and Risk of Mortality The Rotterdam Study. *Stroke*, *45*(1), 42–47. https://doi.org/10.1161/STROKEAHA.113.002348

Pu, F., Xie, S., Li, D., Li, S., Zhang, C., & Fan, Y. (2012). Geometric classification of the carotid siphon: association between geometry and stenoses. *Surgical and Radiologic Anatomy*, *35*(5), 385–394. https://doi.org/10.1007/s00276-012-1042-8

Ross, M., & Pawlina, W. (2016). *Histology; a Text and Atlas* (7th ed.). Wolters Kluwer.

Rowe, A. J., Finlay, H. M., & Canham, P. B. (2003). Collagen biomechanics in cerebral arteries and bifurcations assessed by polarizing microscopy. *Journal of Vascular Research*, *40*(4), 406–415. https://doi.org/10.1159/000072831

Sadasivan, C., Cesar, L., Seong, J., Rakian, A., Hao, Q., Tio, F. O., Wakhloo, A. K., & Lieber, B. B. (2009). An original flow diversion device for the treatment of intracranial aneurysms: Evaluation in the rabbit elastase-induced model. *Stroke*, *40*(3), 952–958. https://doi.org/10.1161/STROKEAHA.108.533760

Sadasivan, C., Cesar, L., Seong, J., Wakhloo, A. K., & Lieber, B. B. (2009). Treatment of rabbit elastase-induced aneurysm models by flow diverters: Development of quantifiable indexes of device performance using digital subtraction angiography. *IEEE Transactions on Medical Imaging*, *28*(7), 1117–1125. https://doi.org/10.1109/TMI.2008.2012162

Schievink, W. I. (1997). Intracranial Aneurysms. *The New England Journal of Medicine*, *10*(4), 739–749.

Seibert, B., Tummala, R. P., Chow, R., Faridar, A., Mousavi, S. A., & Divani, A. A. (2011). Intracranial aneurysms: Review of current treatment options and outcomes. *Frontiers in Neurology*, *JUL*(July), 1–11. https://doi.org/10.3389/fneur.2011.00045

Seppo, J., Jari, S., & Johanna, K. (2005). Hyperglycemia, excess weight, and history of hypertension as risk factors for poor outcome and cerebral infarction after aneurysmal subarachnoid hemorrhage. *Journal of Neurosurgery*, *102*(6), 998–1003.

Serbinenko, F. A. (1974). Balloon Catherterization and Occlusion of Major Cerebral Vessels. *Journal of Neurosurgery*, *41*, 125–145.

Seshadhri, S., Janiga, G., Beuing, O., Skalej, M., & Thévenin, D. (2011). Impact of Stents and Flow Diverters on Hemodynamics in Idealized Aneurysm Models. *Journal of Biomechanical Engineering*, *133*(7), 071005. https://doi.org/10.1115/1.4004410

Shapiro, M., Raz, E., Becske, T., & Nelson, P. K. (2014). Variable porosity of the pipeline embolization device in straight and curved vessels: A guide for optimal deployment strategy. *American Journal of Neuroradiology*, *35*(4), 727–733. https://doi.org/10.3174/ajnr.A3742

Siddiqui, A. H., Abla, A. A., Kan, P., Dumont, T. M., Jahshan, S., Britz, G. W., Hopkins, L. N., & Levy, E. I. (2012). Panacea or problem: flow diverters in the treatment of symptomatic large or giant fusiform vertebrobasilar aneurysms. *Journal of Neurosurgery*, *116*(6), 1258–1266. https://doi.org/10.3171/2012.2.JNS111942

Skodvin, T. O., Johnsen, L. H., Gjertsen, Ø., Isaksen, J. G., & Sorteberg, A. (2017). Cerebral Aneurysm Morphology before and after Rupture: Nationwide Case Series of 29 Aneurysms. *Stroke*, *48*(4), 880–886. https://doi.org/10.1161/STROKEAHA.116.015288

Sobera, M. P., & Kleijn, C. R. (2006). Hydraulic permeability of ordered and disordered single-layer arrays of cylinders. *Physical Review. E, Statistical, Nonlinear, and Soft Matter Physics*, *74*(3 Pt 2), 36301. https://doi.org/10.1103/PhysRevE.74.036301

Soni, S. R. (1974). Aneurysms of the posterior communicating artery and oculomotor paresis. *Journal of Neurology Neurosurgery and Psychiatry*, *37*(4), 475–484. https://doi.org/10.1136/jnnp.37.4.475

Stancampiano, A. P., Engineering, A., York, N., Lieber, B. B., Stancampiano, A. P., & Wakhloo, A. K. (1997). Alteration of hemodynamics in aneurysm models by stenting: Influence of stent porosity. *Annals of Biomedical Engineering*, *25*(3), 460–469. https://doi.org/10.1007/BF02684187

Stehbens, W. E. (1990). Pathology and pathogenesis of intracranial berry aneurysms. *Neurological Research*, *12*(1), 29–34. https://doi.org/10.1080/01616412.1990.11739909

Trobe, J. D., Glaser, J. S., & Quencer, R. C. (1978). Isolated Oculomotor Paralysis The Product of Saccular and Fusiform Aneurysms of the Basilar Artery. *Archives of Ophthalmology*, *96*(7), 1236–1240.

Valencia, A., & Solis, F. (2006). Blood flow dynamics and arterial wall interaction in a saccular aneurysm model of the basilar artery. *Computers and Structures*, *84*(21), 1326–1337. https://doi.org/10.1016/j.compstruc.2006.03.008

van Rooij, W. J., & Sluzewski, M. (2010). Perforator infarction after placement of a pipeline flow-diverting stent for an unruptured A1 aneurysm. *AJNR. American Journal of Neuroradiology*, *31*(4), E43-4. https://doi.org/10.3174/ajnr.A2034

Vignon-Clementel, I. E., Figueroa, C. A., Jansen, K. E., & Taylor, C. A. (2010). Outflow boundary conditions for 3D simulations of non-periodic blood flow and pressure fields in deformable arteries. *Computer Methods in Biomechanics and Biomedical Engineering*, *13*(5), 625–640. https://doi.org/10.1080/10255840903413565

Voldby, B., Enevoldsen, E. M., & Jensen, F. T. (1985). Regional CBF, intraventricular pressure, and cerebral metabolism in patients with ruptured intracranial aneurysms. *Journal of Neurosurgery*, *62*, 48–58.

Waite, L., & Fine, J. (2007). *Applied Biofluid Mechanics* (1st ed.). McGraw-Hill Education.

Walters, K. (1971). On pulsatile flow of non-Newtonian Liquids. *Rheologica Acta*, *10*(4), 517–527.

Weir, B., Disney, L., & Karrison, T. (2002). Sizes of ruptured and unruptured aneurysms in relation to their sites and the ages of patients. *Journal of Neurosurgery*, *96*(1), 64–70. https://doi.org/https://doi.org/10.3171/jns.2002.96.1.0064

Werner, S., Blakemore, A., & King, B. (1941). Aneurysm of the Internal Carotid Artery withing the Skull. *Journal of the American Medical Association*, *116*, 578–582.

Womersley, J. R. (1955). Method for the calculation of velocity, rate of flow and viscous drag in arteries when the pressure gradient is known. *The Journal of Physiology*, *127*(3), 553–563. https://doi.org/10.1113/jphysiol.1955.sp005276

Woo, B. W. K., Gott, S. C., Peck, R. A., Yan, D., Rommelfanger, M. W., & Rao, M. P. (2017). Ultrahigh Resolution Titanium Deep Reactive Ion Etching. *ACS Applied Materials & Interfaces*, acsami.6b16518. https://doi.org/10.1021/acsami.6b16518

Xu, J., Wu, Z., Yu, Y., Lv, N., Wang, S., Karmonik, C., Liu, J. M., & Huang, Q. (2015). Combined effects of flow diverting strategies and parent artery curvature on aneurysmal hemodynamics: A CFD study. *PLoS ONE*, *10*(9), 1–13. https://doi.org/10.1371/journal.pone.0138648

Xu, X., & Lee, J. S. (2009). Application of the lattice Boltzmann method to flow in aneurysm with ring-shaped stent obstacles. *Int. J. Num. Meth. Fluids*, *59*(1), 691–710. https://doi.org/10.1002/fld

Yu, S. C. M. (2000). Steady and pulsatile flow studies in Abdominal Aortic Aneurysm models using Particle Image Velocimetry. *International Journal of Heat and Fluid Flow*, *21*(1), 74–83. https://doi.org/10.1016/S0142-727X(99)00058-2

Zarrinkoob, L., Ambarki, K., Wåhlin, A., Birgander, R., Eklund, A., & Malm, J. (2015). Blood flow distribution in cerebral arteries. *Journal of Cerebral Blood Flow and Metabolism*, *35*(January), 648–654. https://doi.org/10.1038/jcbfm.2014.241

Zenteno, M. A., Santos-Franco, J. A., Freitas-Modenesi, J. M., Gomez, C., Murillo-Bonilla, L., Aburto-Murrieta, Y., Diaz-Romero, R., Nathal, E., Gomez-Llata, S., & Lee, A. (2008). Use of the sole stenting technique for the management of aneurysms in the posterior circulation in a prospective series of 20 patients. *Journal of Neurosurgery*, *108*(6), 1104–1118. https://doi.org/10.3171/JNS/2008/108/6/1104

Zhang, M., Anzai, H., Chopard, B., & Ohta, M. (2016). Towards the patient-specific design of flow diverters made from helix-like wires: an optimization study. *Biomedical Engineering Online*, *15*(Suppl 2), 159. https://doi.org/10.1186/s12938-016-0257-z

Zhang, Yi Sen, Yang, X. J., Wang, S. Z., Qiao, A. K., Chen, J. L., Zhang, K. Y., Liu, Z. C., Zhao, Y. J., Zhang, Y., Luo, B., & Li, C. H. (2010). Hemodynamic effects of stenting on wide-necked intracranial aneurysms. *Chinese Medical Journal*, *123*(15), 1999–2003. https://doi.org/10.3760/cma.j.issn.0366-6999.2010.15.009

Zhang, Yue, Wang, Y., Kao, E., Florez-Valencia, L., & Courbebaisse, G. (2019). Towards optimal flow diverter porosity for the treatment of intracranial aneurysm. *Journal of Biomechanics*, *82*, 20–27. https://doi.org/10.1016/j.jbiomech.2018.10.002